UNIVERSITY OF CALIFORNIA
SANTA CRUZ

Seeking the Sun: Materials Development for Renewable Energy Applications Employing Solar Concentration

A dissertation in partial satisfaction
of the requirements for the degree of

DOCTOR OF PHILOSOPHY
in
PHYSICS

by

Eli Nygren
December 2023

The dissertation of Eli Nygren is approved:

_____
Professor Sue Carter, Chair

_____
Professor Jairo Velasco Jr.

_____
Professor David Lederman

_____
Peter Biehl
Vice Provost and Dean of Graduate Studies

TABLE OF CONTENTS

Table of Contents

ABSTRACT ..... *ix*

ACKNOWLEDGEMENTS ..... *x*

INTRODUCTION **1**

CHAPTER 1: FLUORESCENCE FOR SOLAR ENERGY HARVESTING **2**

PHOTOVOLTAIC EFFECT 2

PHOTOLUMINESCENCE 5

LUMINESCENT SOLAR CONCENTRATOR BACKGROUND 10

LOSS MECHANISMS: 13

CONFIGURATION MODIFICATIONS: 18

EXTENDING THE ABSORPTION RANGE: 22

SYNTHESIS METHODS 23

Organic Dye Systems *23*

Inorganic or Hybrid Semiconductor Systems *28*

GENERAL CHARACTERIZATION METHODS 32

Photoluminescence Spectroscopy *32*

UV-Vis-IR Absorption Spectroscopy *33*

Quantum Yield Measurements *36*

MULTIPLE DYE INTERACTIONS 40

Radiative Transfer: *41*

Forster Resonance Energy Transfer (FRET): *42*

EXPLORING DYE COMBINATIONS 44

AGGREGATION INDUCED FORSTER RESONANCE ENERGY TRANSFER IN MULTI-DYE LUMINESCENT SOLAR CONCENTRATORS 51

Dye Selection *51*

Experimental Design *53*

Conclusion *70*

COMPUTATIONAL MODELING 71

CHAPTER 2: REDOX ACTIVE MATERIALS FOR HYDROGEN PRODUCTION 80

BACKGROUND 80

REDOX REACTIONS FOR SOLID STATE APPLICATIONS 80

COMMON GENERATION METHODS 84

Fossil Fuel Driven Reaction *84*

Electrolysis/ Water Splitting *85*

Solar Thermochemical Hydrogen Production *86*

INDUSTRIAL NEED 90

MULTIPLE AND NONLOCAL CATION REDOX IN CA-CE-TI-MN OXIDE PEROVSKITES FOR STCH APPLICATIONS 92

Stagnation Flow Reactor Experiment *92*

Magnetic Moment Measurements *94*

QUATERNARY OXIDE PEROVSKITE STUDY FOR STCH PERFORMANCE 95

Material Selection Criteria *95*

Solid State Synthesis Reactions *97*

Redox Cycling *99*

Characterization Methods *101*

X Ray Data Analysis Techniques and Results *111*

Conclusions and Remarks..... *131*

REFERENCES **138**

LIST OF FIGURES

Figure 1: Semiconductor Doping..... 3
Figure 2: P-N Junction..... 3
Figure 3: Solar Cell IV and Power Curves..... 4
Figure 4: Jablonski Diagram..... 7
Figure 5: Electronic States and Spin Number..... 9
Figure 6: Edge-Mounted LSC System..... 11
Figure 7: Chlorophyll and LR305 Spectra Overlaid..... 12
Figure 8: Perylene Dye Lumogen Red 305 (left), and expanded view of the perylene core structure (right)..... 13
Figure 9: Total Internal Reflection of an LSC..... 14
Figure 10: PL Redshifting from Reabsorption..... 17
Figure 11: Effects of PV Cell Placement in LSC..... 19
Figure 12: Front-facing Cell LSC.....**Error! Bookmark not defined.**
Figure 13: AM1.5 Spectrum for Photon Counts (left), and Photon Energy (right)..... 22
Figure 14: Polymer Film Synthesis - Drop Casting..... 26
Figure 15: Polymer Film Synthesis - Sheet Casting and Doctor Blading..... 27
Figure 16: Quantum Dot Structure and Energy Level Splitting..... 30
Figure 17: Surface PL Diagram..... 32
Figure 18: Transmittance/Absorbance Schematic..... 33
Figure 19: Integrating Sphere Cross Section..... 37
Figure 20: Spectrophotometer Calibration Light Source Spectra..... 38
Figure 21: Calibration Curve for Integrating Sphere..... 39
Figure 22: Decomposing Excitation and PL Spectra from Integrating Sphere..... 45
Figure 23: LR305 and LV570 Combination Integrating Sphere Spectra (raw data)..... 46
Figure 24: LR305 and LV570 Combination Integrating Sphere Spectra (excitation peak subtracted)..... 47
Figure 25: LR305 and LV570 Combination Integrating Sphere Spectra (white light excitation)..... 50

Figure 26: Absorption and PL Spectra for Selected UV Dyes Overlaid with LR305 51
Figure 27: Molecular Structures of Selected UV Dyes 51
Figure 28: Surface PL Spectra of Dye Combinations in Low Concentration 62
Figure 29: Surface PL Spectra of Dye Combinations in High Concentration..... 65
Figure 30: Relative Spectral Irradiance of Low Concentration UV Dyes, Blend, and LR305 Only, Under AM1.5 Illumination 66
Figure 31: Edge Emission of High Concentration Samples Under AM1.5 Illumination 67
Figure 32: FRET Efficiency as a function of particle separation, observed and expected values 69
Figure 33: Predicted enhancement to PV from each dye blend 69
Figure 34: Observed FRET Efficiency compared to various models for ADS 80 74
Figure 35: Observed FRET Efficiency compared to various models for ADS 61 76
Figure 36: Observed FRET Efficiency compared to various models for ADS 75 76
Figure 37: Periodic Table of the Elements, illustrating electron valency and oxidation states83
Figure 38: Redox cycle diagram for STCH 87
Figure 39: Stagnation Flow Reactor cycling data for water splitting 93
Figure 40: Tube furnace temperature profile illustrating inconsistencies 101
Figure 41: Ellingham Diagram illustrating the changing Gibb's Free Energy for oxidation of various metals .....**Error! Bookmark not defined.**
Figure 42: TGA data for CCTM006 105
Figure 43: Bragg planes illustrating interference of x-rays 107
Figure 44: Idealized x-ray absorption data to show distinct regions 109
Figure 45: XANES data for Mn K edge of all CCTM samples 110
Figure 46: Beamline diagram for x-ray absorption detectors 112
Figure 47: Raw data for CCTM005 Ce L3 edge after 3 reductions 113
Figure 48: CCTM005 Ce L3 edge (after 3 reductions), after normalization, and after flattening 113
Figure 49: Flow chart for processing raw XANES data 114
Figure 50: First derivative of Mn K edge across all redox steps for CCTM005 and references 116
Figure 51: Mn K edge for CCTM006 and references, showing absorption edge via half-line crossing 117

Figure 52: Ce L3 edge for CCTM006 and references, showing absorption edge via half-line crossing 118

Figure 53: Mn K edge for CCTM005 and references, showing absorption edge via half-line crossing 118

Figure 54: Ce L3 edge for CCTM005 and references, showing absorption edge via half-line crossing 120

Figure 55: XRD data for CCTM and associated phases with labeled peaks 121

Figure 56: XRD for CCTM006 across all redox steps 122

Figure 57: Zoom-in on CCTM006 XRD to illustrate lattice parameter shifting 124

Figure 58: Illustration of lattice parameter expansion due to oxygen vacancy 125

Figure 59: Lattice parameter 'a' across all CCTM stoichiometries 126

Figure 60: Lattice parameter 'b' across all CCTM stoichiometries 126

Figure 61: Lattice parameter 'c' across all CCTM stoichiometries 127

Figure 62: "Squareness index" across all CCTM stoichiometries 127

Figure 63: XRD zoomed in for pristine state of all CCTM stoichiometries 128

Figure 64: Changes in mass throughout redox cycling for all CCTM stoichiometries, and implied oxygen deltas 129

Figure 65: Oxide reduction potential as a function of manganese content 131

Figure 66: Diagram of a potential real world STCH reactor 132

ABSTRACT

Seeking the Sun: Materials Development for Renewable Energy Applications Employing Solar Concentration

by

Eli Nygren

Nearly all energy production on Earth can be traced back to the sun, and yet we are still finding innovative ways to tap directly into this source for our energy needs. I start by describing efforts to enhance the efficiency of luminescent solar concentrators (LSC), which offer a pathway for dual purpose land coverage to meet agricultural and power production needs. By incorporating a second fluorescent species into the LSC, I show that power enhancement to a typical cell configuration can be improved by ~5%. To keep up with an ever-growing human demand, however, reliable energy *storage* for renewables needs to improve. Hydrogen has long been considered a promising energy carrier to solve this problem, and here I will discuss advances in generating this fuel from nothing but water and concentrated sunlight. A novel oxide perovskite material used for splitting water via redox reactions, CCTM, is hereby described. It is shown to be remarkably stable and outperforms all other leading material candidates for the same task.

ACKNOWLEDGEMENTS

After taking a very long hiatus midway through my undergraduate studies, I never thought I would complete the degree, let alone continue on to a doctoral program. Thank you to everyone who encouraged me to do this crazy thing, whether it was the wise move or not. I gained so much both academically and personally from this experience, and I have many people to thank for that. My fellow lab mates were always a source of inspiration, and sometimes necessary distraction. I will miss our philosophical discussions. Other friends I've made during my time in graduate school I will cherish forever. My family has always been supportive, and that has continued in full force through this chapter of my life. Most of all, though, thank you to my amazing wife for supporting me both emotionally and financially through grad school. It has been an amazing journey, and I know the future holds many more blessings for us.

INTRODUCTION

Ever since the discovery of fire, humanity's success has grown intertwined with the rapid oxidation of fuels to convert stored energy into heat. Add an industrial revolution, creation of an electrical grid, and personal vehicles for an ever-growing population, and we find ourselves at a point where reimagining this relationship would be wise. Besides the clear connection between increased atmospheric carbon dioxide and average temperatures, we simply must face the issue of limited supply. By many accounts, the Earth may only have 50-100 years of recoverable oil left to extract[1]. Regardless of one's stance on the severity of climate change, it's hard to argue against the fact that we really ought to start making the switch to renewable sources of energy.

Fortunately, the technology already exists to convert many of our energy intensive activities from fossil fuels to renewable sources. The main push with most of these technologies is to bring the cost down to make them economically competitive with conventional methods. Governmental subsidies and incentives can play an important role in this, but that topic is best left to other works.[2] Another approach is to tackle individual high energy industries with niche technologies which offer benefits specific to each one. The present paper will highlight two such niche technologies, outline my work on improving these technologies from a materials science angle, and discuss the outlook of their viability in societal use.

CHAPTER 1: Fluorescence for Solar Energy Harvesting

Photovoltaic Effect

Before diving into light concentration for solar energy conversion, let's discuss the basics of the photovoltaic cells which would cover a standard solar panel. Using the most conventional PV material on the market, silicon, as an example, this section will outline the physics which allow us to turn sunlight into electric power.

A silicon PV cell is an example of a diode, in fact it is also knows as a photodiode. As such, a PV cell is made to allow current through it in only one direction. Silicon itself is a semiconductor, that is, its electronic fermi level lies within a bandgap. This means that, with no outside energy input, its outermost electrons are bound tightly and not free to delocalize and conduct electricity. This behavior alone makes it an insulator. However, because of the relatively low energy difference between the valence and conduction bands, the semiconductor may permit the flow of electrons with minimal outside intervention. This intervention can come in the form of heat, or the absorption of light with sufficient energy. Whatever the mechanism, the energy threshold to promote an electron from the valence to conduction band is the bandgap energy.

The behavior can be further altered by adding in elements with different valence states, in a process called doping. For silicon (O = 4), this would typically be boron (O = 3) or phosphorous (O = 5). By doping in elements with more valence

electrons than silicon, there are surplus electrons (still neutral charged lattice) because only 4 electrons are needed to participate in bonds within the silicon structure. This is called n-type doping because one inserts negative charges. When doped with boron, the opposite effect is observed. One less electron is present than needed to participate in bonding. This can equivalently be thought of as introducing an extra 'hole' into the lattice, or a place that a different free electron could occupy given the opportunity. This is known as p-type doping.

The basis for many diodes, including a silicon PV cell, is to fuse a p-type and an n-type together, creating a P-N junction. The P-N junction is so useful because it fills the excess holes in the p-type region with the surplus electrons in the n-type region, creating a charge separation yielding a 'built in potential'. This potential is what allows the one-way traffic in any diode, due to the depletion of charge carriers in the center of the PN junction. Applying a voltage which opposes this built in potential has the effect of shrinking away the depletion zone, giving a continuous path for charge carriers. Applying the voltage in reverse only serves to increase the depletion zone, and will not conduct.

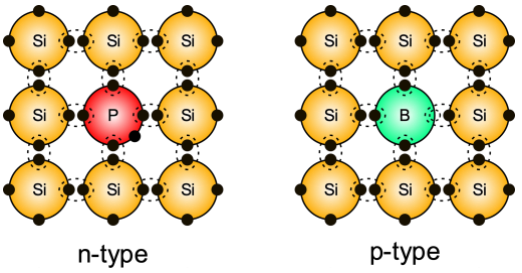

Figure 2: Semiconductor Doping

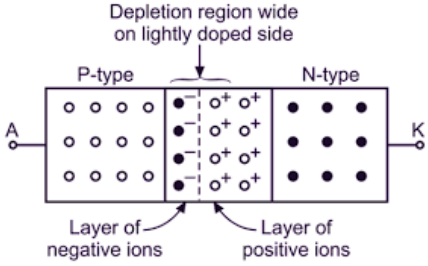

Figure 1: P-N Junction

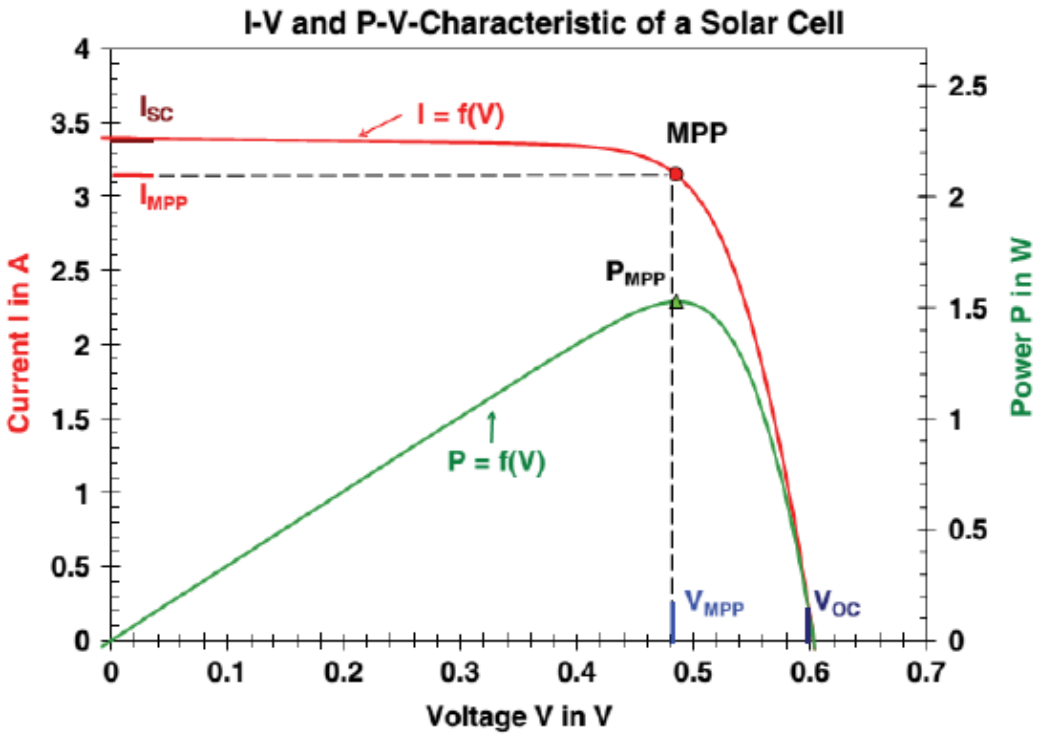

Figure 3: Solar Cell IV and Power Curves

The other important effect the bandgap has is setting the energy of each electron being conducted. This can be visualized by understanding that each outgoing electron is sitting at an energy level equal to the bandgap difference, which manifests in the system as a higher working voltage. It is therefore tempting to say that we should simply find the highest bandgap material for our solar cells to achieve highest efficiency. This is a fallacy, though, because the higher the bandgap, the more incoming photons *go unabsorbed*, missing more and more of the solar spectrum. This delicate balance was summarized in 1961 by William Shockley and Hans-Joachim Queisser, in their famous expression for solar cell efficiency[3] .

$$\eta = \frac{E_g \int_{E_g}^{\infty} b_s(E)dE}{\int_0^{\infty} E b_s(E)dE} \tag{0}$$

With this idealized expression for PV efficiency, we can calculate an optimal bandgap energy for a given incoming spectrum. For our sun, after it passes through the atmosphere, this optimal bandgap turns out to be 1.4 eV, leading to a theoretical maximum efficiency of 33%. Silicon, having a bandgap of 1.1 eV, is just slightly lower than this, and results in a theoretical maximum of about 31%, which is good enough given its abundance and long history of successful use.

For solar energy applications where the incoming spectrum is somehow modified, as we will explore in future sections, this optimal bandgap will change. For instance, as in the upcoming luminescent solar concentrator, incoming light to the PV cell may be at a sharp peak in wavelength. In this case, the optimal semiconductor would have a bandgap just above the energy of these incoming photons to achieve a high voltage while still producing a photocurrent from absorbing all photons. The matching of bandgap to concentrator system will not be a focus of this paper, but is important to introduce as future advances in the field may be related to this.

Photoluminescence

Simply put, photoluminescence (PL) is the emission of a photon by a material directly following the absorption of a higher energy photon. Let us distinguish terminology for the different ways and material systems in which this can occur. Most

molecular systems of interest which demonstrate PL contain carbon atoms, and will thus be referred to as organic systems. In an organic system, absorption of a photon results in the promotion of an electron from a ground state orbital to an excited state orbital. An excited state is not a stable environment for an electron, and it will take any number of pathways to decay back into its ground state. Before looking at these pathways, let's define some terms. For a single atom, the "outermost" electrons are the valence electrons. Similarly, for a molecule, these highest energy electrons are said to be in the *highest occupied molecular orbital (HOMO)*. The next available energy state, quantized as they are, is known as the *lowest unoccupied molecular orbital (LUMO)*, and represents the minimum threshold of energy required to promote an electron.

For a more complete view of allowed energy states, we must include not only electronic states, but also vibrational and rotational states. All combined, this leads to a multitude of available states which are only slight deviations in energy from the electronic states. The effect this has on a molecule's absorption spectrum is to widen its peaks, which would otherwise theoretically be delta functions. A promoted electron can momentarily exist in any number of these states, whereby a handful of relaxation events can occur. An electron cascading down between pairs of closely spaced states exhibits vibrational relaxation, otherwise known as thermal relaxation. In this case, no photons are emitted after the absorption event, and the energy instead goes to heating the material. If the electron transitions between states of sufficiently high energy difference, it may result in photoluminescence. A typical pathway is for

the electron to thermally relax down to the lowest vibrational substate within an electronic state, and then drop to a lower electronic state from this “cliff edge”, emitting a photon. These interactions are summarized well in a Perrin-Jablonski Diagram, shown below.

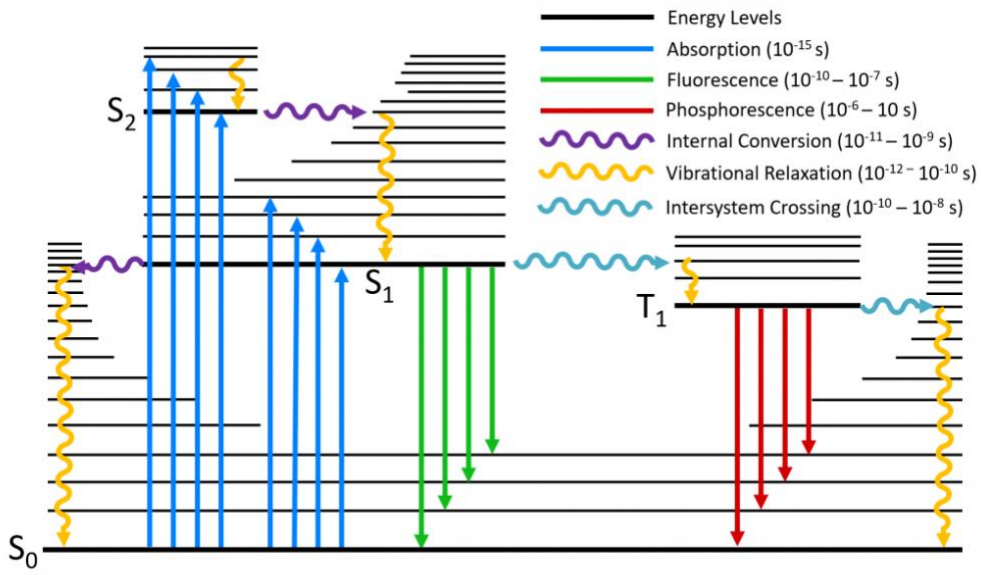

Figure 4: Jablonski Diagram

The tendency to transition *from* a lower cliff edge *to* an arbitrary substate, whether promoting or relaxing, yields absorption and PL spectra which are roughly mirror images of each other, reflected about the wavelength corresponding to the orbital energy difference. The emitted photon will always be of a lower energy, because of the thermal relaxation which occurs, and the difference in wavelength of absorption and PL peaks is known as the *Stokes Shift*. The benefit choosing molecules with a high Stokes Shift will be discussed in the next section.

Electronic transitions, however; are governed by selection rules worked out by pioneers in the early days of quantum theory such as Neils Bohr, and later formalized by Alfred Lande, that describe which transitions are in accordance with physical laws such as conservation of angular momentum. In spectroscopy, an important finding is that quantum number J=+/-1, based on the fact that a photon has a spin of 1. For a complete guide to selection rules, refer to this work. [4] Any transitions which do not follow the most basic selection rules are known as *forbidden transitions*. Phosphorescence is an example of such a transition, occurring when an excited electron in a singlet state migrates into a triplet state with a slightly lower energy. This cannot be achieved by the absorption or emission of a photon, because it involves a change of electron spin. It can, however, be achieved by vibrational interactions. Once an electron exists in this triplet state, the only lower energy state it can drop to is the ground singlet state. Because this involves yet another spin transition, it is statistically unlikely to happen. This manifests as a long break between the absorption, and phosphorescent emission of a photon. This feature is what allows certain glow in the dark materials to keep glowing minutes or even several hours in darkness after being “charged” by a light source.

The spin multiplicity of an excited state can be thought of as the total number of microstates possible within a given microstate. As an example, there are three possible ways to have two electrons have parallel spins after an excitation event. They could both be spin up, both be spin down, or both be in a superposition of the two.

This works because electrons in two different spatial quantum states are distinguishable. The multiplicity in general is given by the equation;

$$\boldsymbol{M} = 2(2\boldsymbol{S} + 1) \tag{1}$$

...where M is the multiplicity, and S is the total spin quantum number when all electrons have been considered. If two electrons are in the same orbital, their spatial state is said to be symmetric and their spin states must then be antisymmetric to satisfy the Pauli Exclusion principle. The converse is also true. These ideas are summarized nicely in the figure below.

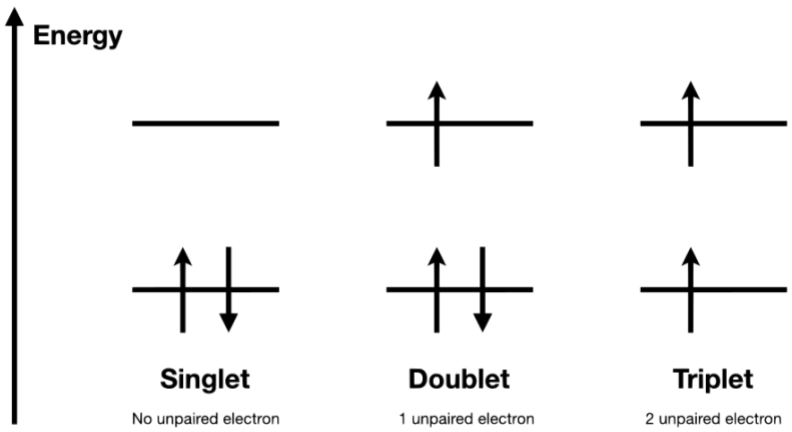

Figure 5: Electronic States and Spin Number

Luminescent Solar Concentrator Background

Luminescent Solar Concentrators (LSC) have a history in research dating back to 1973[5]. Initially proposed as a means to maximize the output power for minimal solar cell material, the LSC uses one or more luminophores embedded in a polymer matrix to absorb higher energy photons from the sun and re-emit lower energy photons according to the dye's Stokes Shift. The majority of these emitted photons, are subject to total internal reflection, as determined by the index of refraction of the waveguiding material, commonly glass or poly-methyl methacrylate (PMMA) sheets. In the classical configuration, some or all of the edges of the LSC are lined with a photovoltaic material such as silicon. If only some are PV lined, reflective tape covers the other edges in order to redirect and channel all the light toward the PV-lined edges. One major initial motivation for this technology was to minimize the PV material, due to the relatively high cost of this component. However, as silicon solar cells have dropped dramatically in price, this aspect has become less of a factor. When considering the effective power conversion efficiency (PCE) of the classical LSC panel, it can never hope to compete with a conventional solar panel with ~100% cell coverage, because only a small portion of solar photons will be fluoresced through the waveguide material. With all major loss mechanisms wrapped into one internal efficiency factor, Q_{LSC}, encompassing incomplete absorption, escape cone, and reabsorption losses, we get a formula for total LSC efficiency.

$$\eta = Q_{LSC}\, \varphi_{dye}\, Q_{PV} \tag{2}$$

Where φ and Q_{PV} are the quantum yield (to be discussed later) and the PCE of the photovoltaic cells themselves. Because of the competitive price for silicon of late, instead of minimizing *cell* area, recent efforts have focused on giving LSCs dual functionality to maximize use of *land* area.

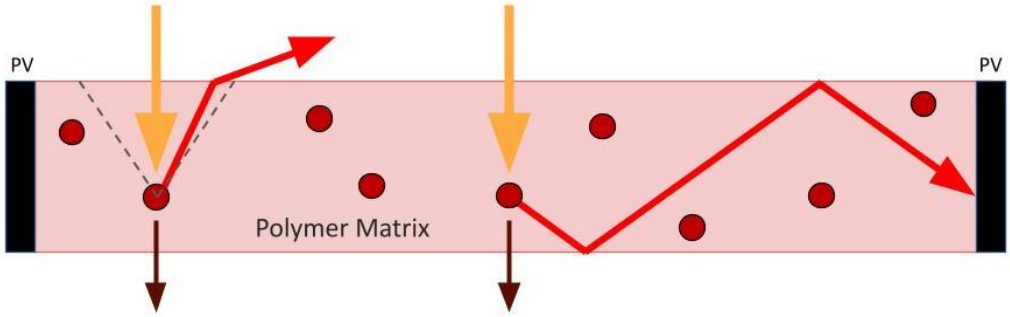

Figure 6: Edge-Mounted LSC System

Greenhouses have become an attractive application option due to the considerable land area needed for both agriculture and grid scale solar arrays. Moreover, plants (and other photosynthesizing organisms) have a unique spectral response, which is complemented well by certain LSC schema. The chloroplasts in plant cells contains any of several varieties of chlorophyll ('a' and 'b' being the two most common), which absorb only red and blue portions of the visible spectrum, leaving the viewer to see reflected (or transmitted) green light. The fact that this green part of the spectrum is unused by plants, and in many cases even hinders their productivity, points toward the development of a system which absorbs green light, and subsequently reemits red light. Below is shown absorption spectra of the two most common varieties of chlorophyll, overlaid with absorption and

photoluminescence (PL) spectra of our current state of the art LSC dye, Lumogen Red 305 (LR305). [6], [7]

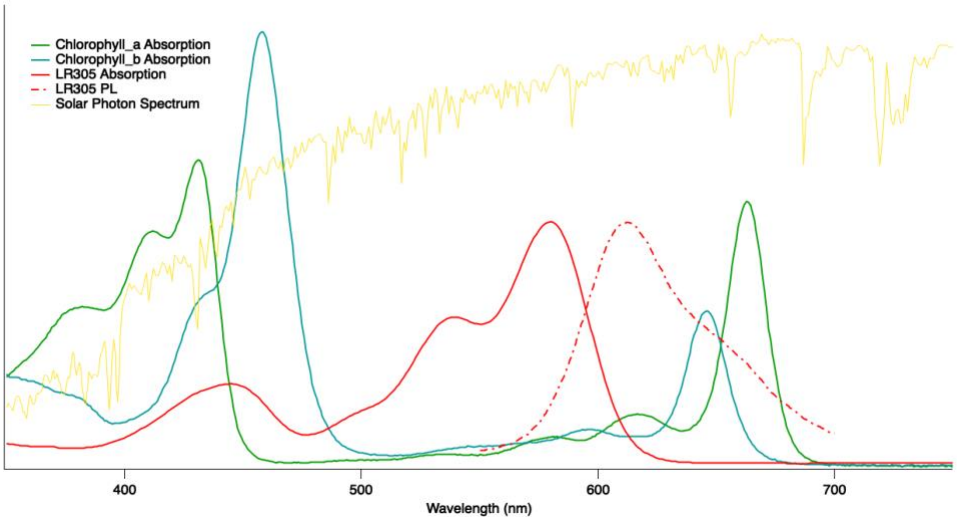

Figure 7: Chlorophyll and LR305 Spectra Overlaid

As we can see, this dye not only absorbs unwanted green light, but it actually can potentially amplify the amount of red light that the plants see. The extra red light can actually give a slight additional boost to plants, as it overlaps nicely with the second peaks of both common chlorophyll species. Its absorption spectrum aligns nicely with the photonic emission spectrum of the sun, and the red part of chlorophyll's absorption sits right at the wavelength at which the sun emits the most photons.

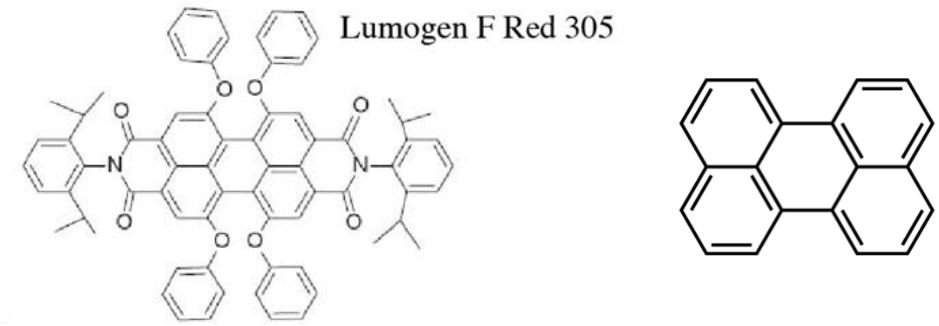

Figure : Perylene Dye Lumogen Red 305 (left), and expanded view of the perylene core structure (right)

LR305 is an example of a perylene dye, which hold industrial importance in applications such as pigments and lasing media. The perylene molecule itself has a chemical formula of $C_{20}H_{12}$, and can be visualized as 5 hexagonal carbon rings stacked in a honeycomb pattern[8]. On its own, it exhibits a brownish color and blue fluorescence when excited by UV light. An incredible number of variations in optoelectronic properties can be realized by building peripheral structures off this perylene core. Such molecular constructions are called perylene dyes, including our relevant example of LR305. Notice the perylene core of this molecule, and the biaxial symmetry of the extensions.

Loss Mechanisms:

Escape cone – The containment of light within the waveguide of an LSC relies on the principle of total internal reflection (TIR), whereby all light traveling past a critical angle may be “trapped” in a medium of higher refractive index than its surrounding environment, based on Snell’s Law.

$$n_1 \sin\theta_1 = n_2 \sin\theta_2 \quad (1)$$

The light which emanates at an angle lower than this, is said to be in the "escape cone" and will leave the medium, refracting at the interface.

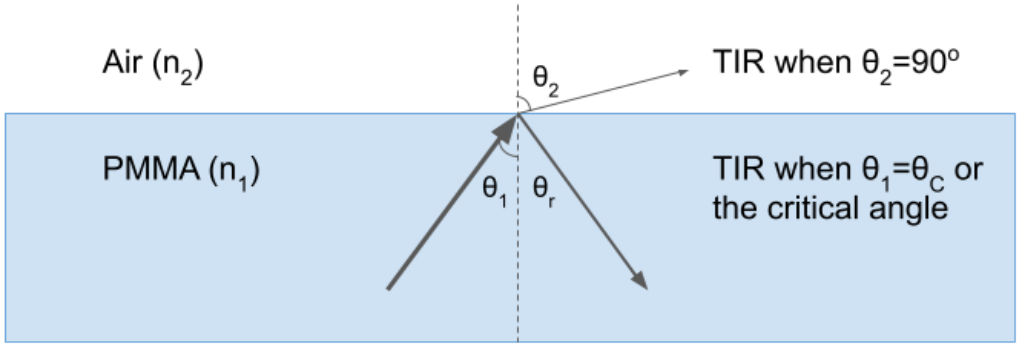

Figure 8: Total Internal Reflection of an LSC

For a typical LSC medium of glass or PMMA (n ~ 1.5), and given that air has an index of refraction of n ~ 1, the escape cone boundary exists at an angle of ~41.8° off normal. This is in accordance with the critical angle formula;

$$\theta_C = \sin^{-1}\left({}^{n_2}/_{n_1}\right) \quad (2)$$

By integrating across all solid angles between $-\theta_C$ and θ_C, we can predict what portion of PL photons will remain within the waveguide. This is made possible by realizing that PL occurs (in most cases, including ours presently) isotropically, and therefore we only need to know the ratio of solid angles contained within the escape

cone to all solid angles. It is important to realize that there is an escape cone both above *and below* the waveguide, thus the bounds.

$$\iint_{0,\theta_C}^{2\pi,\pi-\theta_C} \sin\theta \; d\theta \; d\varphi \tag{3}$$

Plugging in the previously stated critical angle value to the above integral and dividing by 4π, we obtain a value of 0.745. Subtracting this form one and multiplying by 100, we see that ~25% of photons are lost via both escape cones. While none of these photons will contribute to a photocurrent, the escape cone on the underside of the LSC panel will contribute red photons to the plants below, enhancing photosynthetically active light.

The next loss mechanism is simply incomplete absorption of incoming light within the target wavelength range. There is no set way to calculate this loss because different dyes will target different ranges of photon wavelengths to absorb. In an ideal world, our fluorophore would absorb 100% of the photons with higher energy than the bandgap (or HOMO-LUMO gap). For direct bandgap semiconductor fluorophores, this is almost true. Especially for organic molecules, though, there are complicated peaks and valleys in the absorption spectrum based on the molecular orbital structure. Of course, increasing the dye concentration or film thickness can always achieve higher absorption. However, there are potential efficiency penalties for doing this, discussed next.

Most fluorescent molecules show a substantial overlap in their absorption and PL spectra. This arises from the fact that transitions are allowed to occur between a multitude of pairs of vibrational substates, and a portion of the emitted light will have enough energy to promote an electron between substates of a lower energy difference. When a PL photon is absorbed by the same species of molecule which emitted the light, it is called reabsorption, and has the potential to reduce the efficiency of the system

Reabsorption will not lead to any losses if and only if the molecule is 100% efficient at converting absorbed photons into PL photons. If this is not the case, the system will incur a loss in efficiency because a portion of the photons destined to hit the PV cell are instead converted to heat energy after being intercepted by another dye molecule. This PL efficiency is known as quantum yield, and will be further defined in a future section. The main factor at play here is known as the Stokes Shift, which describes the difference in wavelength (or energy) between the absorption and PL peaks. Due to the broadening of both peaks from vibrational states, there is a chance that fluorescence on the higher energy side could be absorbed by the same species of fluorophore, causing an excitation on the lower energy end of the spectrum. If the second absorption event does not lead to an emitted photon, a loss is

incurred.[9]

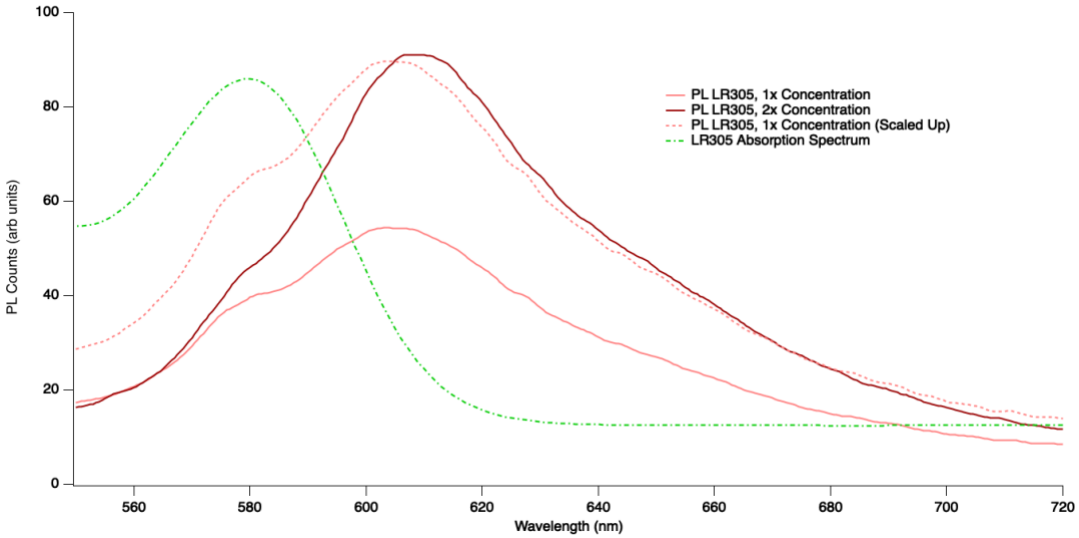

Figure 9: PL Redshifting from Reabsorption

Above samples were prepared as ~0.5mm thick PMMA sheets with either 10:1 or 10:2 molar ratios of polymer:dye. The lower dye concentration (solid pink) sample is shown both as is, and scaled (dashed pink) so that the peak value coincides with that of the higher concentration, to show their differences clearly. Notice how the PL spectrum of the higher concentration dye:polymer matrix shifts toward longer wavelengths, and this shift occurs as a function of wavelength. This is because bluer PL photons are sitting in a region of stronger absorption, as illustrated by the dashed green line in the above plot. Dye concentration, LSC dimensions, and PV cell placement can all affect how much self-absorption occurs.

Configuration Modifications:

While the edge mounted PV configuration would lead to the highest transmittance to the plants below, it also leads to a meager power performance, driven *only* by the fluoresced waveguided light. It is beneficial, in most practical applications, to attach front facing cells at less than 100% coverage. This way, the PV cells produce current from both the direct sunlight, and an additional *PV enhancement factor* due to the waveguided light.

$$Enhancement = \frac{Power_{LSC}}{Power_{PV,\ no\ dye}} - 1 \qquad (4)$$

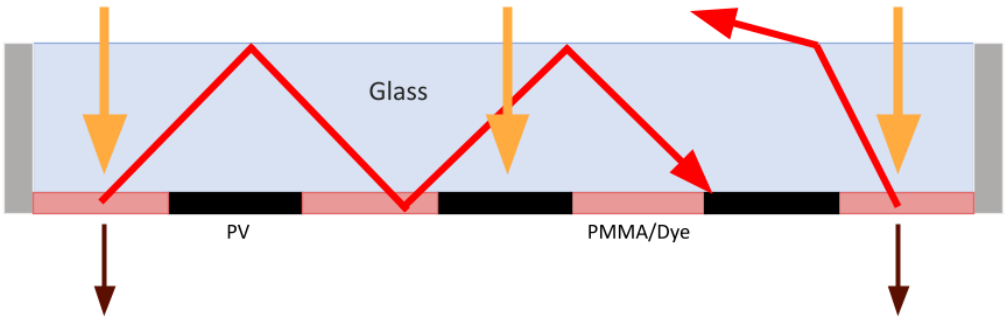

Figure 10: Front-facing cell LSC Design

As mentioned earlier, total power output obviously increases as the cell area approaches 100%, but this also blocks more red light from reaching plants below. So, we develop a picture of LSC performance which requires increasing cell coverage up to the point where crops below will still experience adequate growth. This is a difficult criterion to quantify, but our current system operates at ~50% coverage and

strikes a good balance here. Additionally, there is the question of cell placement and configuration. It stands to reason that fewer, larger patches of PV cells will benefit less from the waveguided light than will more, smaller strings of cells[10]. This hypothesis is put to the test in the paper cited below, to determine optimal cell configuration for an LSC. Two, equal area, configurations are plotted alongside the curve required to achieve 6% PCE (once considered economical viability indicator), as revealed through computer simulation. Values left of the curve are considered economically viable.

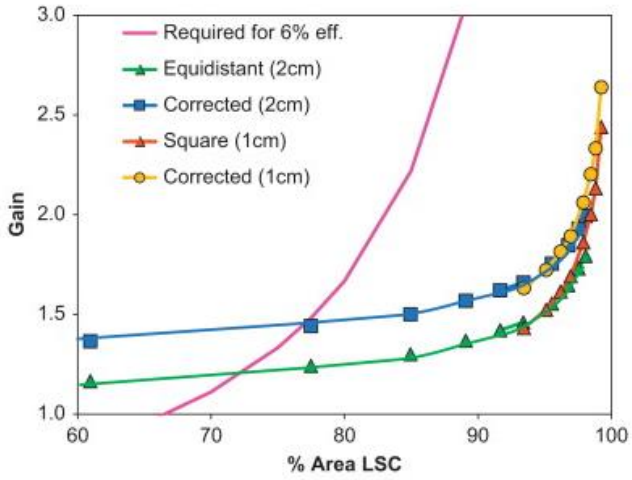

Figure 11: Effects of PV Cell Placement in LSC

The concept of *enhancement* in an LSC arises from the front-facing configuration. In simple terms, it is defined as the percentage above the max power that would be realized with the PV cell coverage alone, that is contributed by the waveguided light due to the fluorescent material. For example, a one square meter LSC panel would have roughly 1000 watts of (usable) solar light incident upon it. If exactly half of it were covered with monocrystalline silicon PV operating at 20%

PCE, then its direct light max power production would be 100 watts. However, due to the fluorescent activity of the dye within the entire medium, an actual mass power of say 120 watts might be seen. This LSC would be exhibiting an enhancement factor of 20%.

Red tinted greenhouse panes have been used previously in agricultural applications *purely* for their ability to prevent unusable light from heating up crops, with no coupling to a PV system[11]. The red LSC concept simply adds power generation to the system. Different parts of the solar spectrum can stimulate specific type of growth for certain plants. For example, red light causes many plants to grow bushier rather than taller, and develop flowers earlier. For many crops, this translates into accelerated growth and thus is an economically interesting option. Most plants do not actually need (or even benefit from) the full intensity of modified sunlight that the dye embedded sheet would offer. Each plant species has its own maximum rate at which it can utilize solar energy to produce carbohydrates. Because of this, and depending on which crops are grown, it is perfectly acceptable to cover a large portion of the panel with front facing cells.

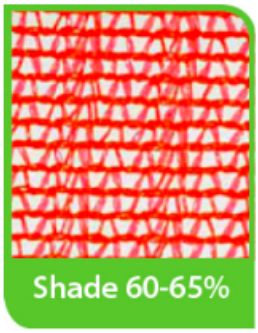

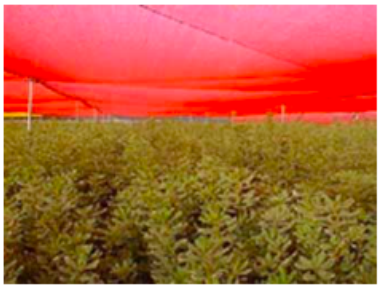

Technical Details

UV resistance (years) 5
Maximum width (m) 26 ft (8 m)

ChromatiNet Red Shade Net 60%: 60-65% Shade Protection

ChromatiNet Red changes the light spectrum transmitted to the plants, reduces the spectrum of blue, green and yellow light and increases the red and far-red light spectrum. Thus, the rhythm of plants' development under red light is increased, their leaf surface is larger, their stems are longer and thicker, and the total foliage volume is higher.

- Excellent shading solution for growers who wish to accelerate growth.
- Obtain early flowering without decreasing flower quality.
- Increase foliage volume plants such as house plants, decorative branches, non-flowering herbs, and a variety of field and nursery plants.
- Enhance the development of root systems in shoots and tissue culture plantlets.
- Flexible, light, strong and easy to spread.
- Available in various widths.
- Recyclable and UV resistant.

Figure 12: Example of commercial red shades for greenhouses, ChromatiNet

Extending the Absorption Range:

While LR305 does a great job of converting the unwanted parts of the visible range, it largely leaves UV and NIR alone. From the solar cell's perspective, the

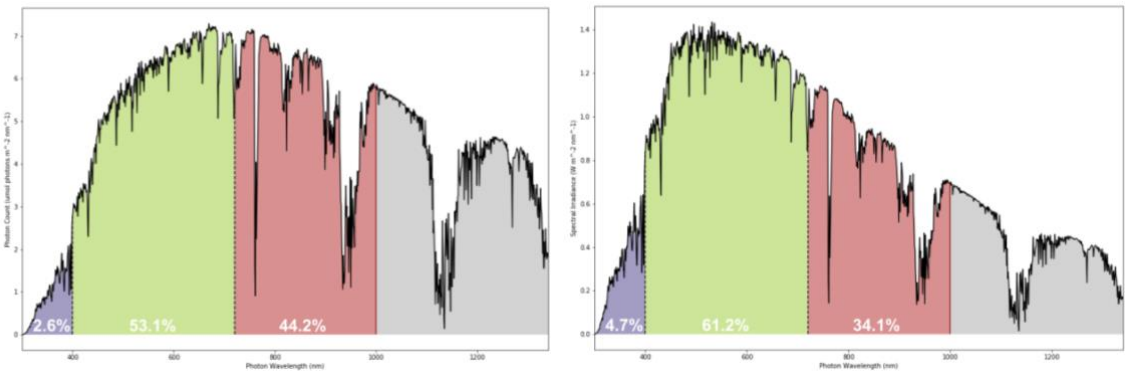

Figure 13: AM1.5 Spectrum for Photon Counts (left), and Photon Energy (right)

highest efficiency of an LSC would be achieved if the luminescent dye absorbed all light from UV up through visible, and luminesced a sharp peak of around 1000 nm light. This is because silicon's bandgap of 1.1 eV allows it to efficiently absorb and convert light up to this energy. Solar cells depend on the absorption of light of higher energy than the bandgap, and it is the overall number of photons absorbed which determines its power output. Because of this, the plot showing number of photons per wavelength bin (left) from the sun is more helpful than the standard power spectrum (right) often shown since it is scaled by the photon energy. Since any additional photon energy is wasted as heat in a solar cell, any number of 1000 nm photons will yield the same photocurrent as the same number of photons somewhere in the visible or UV ranges. Therefore, NIR emission is promising since it could theoretically yield

the most photons. While this seems like a good place to put one's effort, NIR and IR emitting dyes tend to suffer from low quantum yields[12], [13]. Many complex interactions may contribute to this effect, but a main reason for this is that an electron at the band edge has many nonradiative decay pathways of similar energy difference to that of the bandgap itself. These nonradiative pathways manifest as thermalization and lower the PLQY.

This leaves the UV portion to investigate as a source of extra energy. UV fluorescent dyes can often have near unity quantum yield, and their contribution to the LSC can be made without absorbing valuable red light before the plants get it. While the UV range only contains 2.6% of the usable photons from the sun, these would go completely unused in a conventional LSC setup. The following section will investigate the effects of pairing LR305 with a variety of UV dyes for LSC applications.

Synthesis Methods

Organic Dye Systems

Dye Preparation

Concentrated dye solutions are prepared for future use with a variety of organic solvents. The solvent must be chosen wisely as to dissolve both the dye and whichever polymer will be used to make the sample. On an interesting note, when

observed in solution, a fluorescent dye may exhibit vastly different PL peaks depending on the solvent used. This effect is known as solvatochromatism, and is caused by conformational changes in the fluorophore based largely on the polarity of the solvent it interacts with[14].

These dye solutions have typically been made at concentrations of between 1-10 mg/mL. This is achieved simply by weighing an amount of dye powder directly in a vial, dividing that value (in mg) by the desired concentration, and pipetting the resulting amount of solvent into the vial. In general, adding a solute to a solvent will change the total volume (either increasing or decreasing it depending), but this effect has been ignored in this procedure, because preliminary findings indicate that the effect is negligible or nonexistent. When low final concentrations are desired, it is best to start with a low concentration solution. Sample dye mass is accurately set by adding a known volume. This is a much more precise and reproducible method than weighing out powder and transferring every time. However, the relative uncertainty in dye mass increases as the volume of liquid transferred decreases. Therefore, it is desirable to have a large proportion of the total solvent used to dissolve the polymer be from the dye solution itself.

Polymer Dispersal

Dry polymer beads or powder is first weight out directly in a 20mL glass vial. The target polymer solution concentration depends on the final formation process to be used. For spin casting, a concentration of about 100 mg/mL or lower is desired to

allow for consistent pipetting for dispersal. If sheet casting is to be pursued, a higher concentration of around 200-300 mg/mL is best. This leads to fewer gas bubbles forming, causing imperfections in the film. In either case, a calculated amount of dye solution is added to the polymer, followed by however much pure solvent is needed to achieve the desired concentration. If many samples are to be made, a spreadsheet is recommended to streamline the process. Typically, a stir bar is added to the vial, spinning on heat at least overnight, until all polymer has dissolved and dispersed evenly.

Casting

Once the polymer solution has been made, all that's left is to distribute it so as to obtain a solid film or sheet for characterization. One common method is called spin casting. In this procedure, the solution is pipetted onto a 1" square glass slide, which is immediately spun using a dedicated spin coater device. The speed and duration of rotation can be adjusted, altering film formation. The most tunable parameter here is the film thickness, being affected by a combination of solution concentration and spin speed. In a simplified theory, all else being equal, the spin speed affects film thickness in the following way:[15]

$$t \propto {}^{1}/_{\sqrt{\omega}} \tag{5}$$

...where *t* is the film thickness, and ω is the angular velocity of the spin process. For polymer films, the spin should be initiated immediately after dispensing the solution

onto the glass. Otherwise, it may start to harden in a bubble formation centered on the slide, leaving the film inconsistent and thicker in the middle. Slides should be cleaned prior to casting according to lab procedures. Polymer films are typically less sensitive to surface conditions than neat films, and less stringent methods may be used.

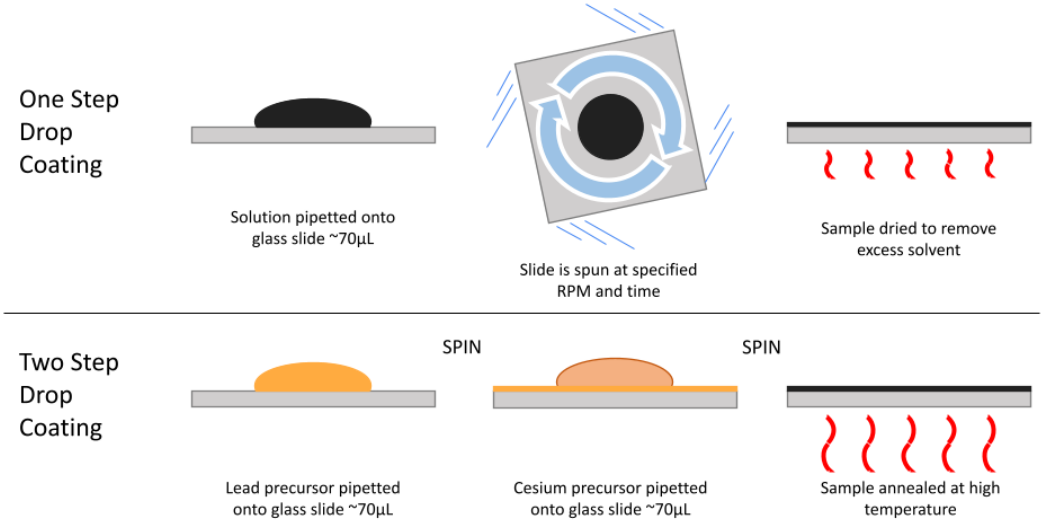

Figure 14: Polymer Film Synthesis - Drop Casting

When thicker films are required, sheet casting may be used. In this method, a thick, honeylike solution is mixed first, which is then poured into a small aluminum tray. Once all samples have been poured into trays, they are loaded into a vacuum oven. Heat is applied (temperature depends on polymer) and vacuum is pulled, and then left at least overnight to evaporate as much solvent as possible. If the initial polymer solution was made too thin, it may result in the formation of large bubbles.

Once all solvent has off-gassed, the resulting discs can be pressed into "pucks". A convenient instrument to achieve this is a hot press (like one commonly used for T-shirt prints). Discs are placed between the heated platens in between two non-stick sheets such as [], and then pressed at around 40 psi. Spacers may be placed in the corners to achieve uniform thickness. After pressing, sheets get cut into a standard dimension rectangle (1cm x 2cm) using a hot knife and a straight edge. Clean edges are important for ensuring consistent and low scattering of waveguided light off the edge.

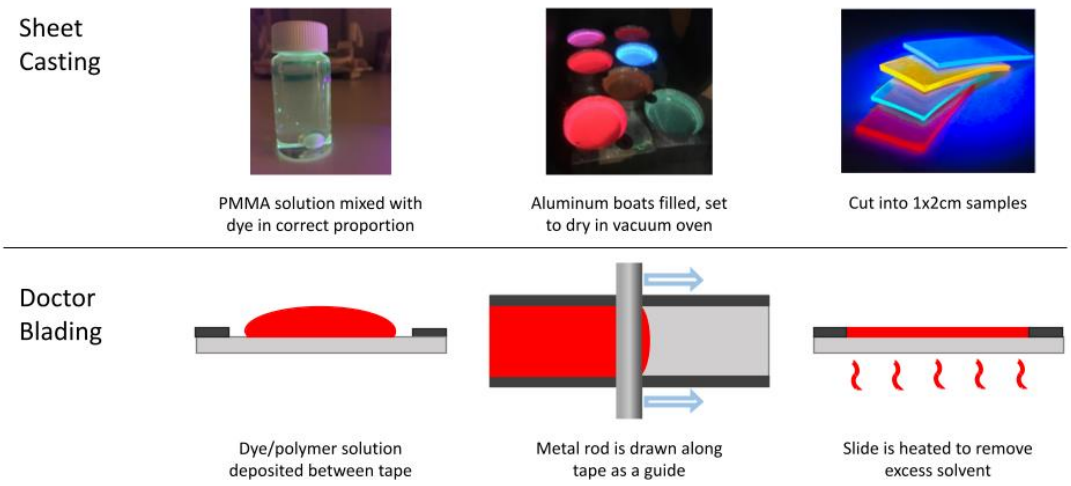

Figure 15: Polymer Film Synthesis - Sheet Casting and Doctor Blading

For film thicknesses in between the above two examples, doctor blading may be used. Simply put, a polymer solution gets troweled into a channel created by sticking tape to opposite edges of a glass slide. This achieves a film thickness close to

the thickness of the tape used, and can result in fairly smooth samples. A dedicated doctor blading actuated steel rod may be used, or a fresh razor blade if none is available.

Inorganic or Hybrid Semiconductor Systems

Let's take a second to define a semiconductor and see an important manipulation we can make. As briefly mentioned previously, a semiconductor is a solid state material whose most energetic electrons (in the valence band) have a minimum threshold of energy to acquire in order to jump to the next set of occupiable states (conduction band). This difference in energy between the two bands is known as the bandgap, and is one of the most important characteristics of most semiconductors. It is effectively a measure of how 'stuck' each electron is as it exists localized around a particular atom within the lattice. They have found many applications in modern life, from computer transistors to LEDs, and much more. While the bandgap determines the crystal's function, the structure determines the bandgap. A perfect crystalline structure, with infinitely repeating pattern, will have a very clean, well-defined bandgap. However, the presence of any defects (and there always are) may create additional states an electron can occupy within the bandgap. These are called *trap states*, and tend to negatively affect the function of the material. In a semiconductor fluorophore, this often manifests as a decrease in PLQY. When there is a clear bandgap, temporarily excited electrons are much more likely to radiatively relax once they have reached the band edge. When trap states are present,

there will be a portion of electrons which relax thermally by way of these trap states, instead of releasing a photon.

The advent of nanocrystal (NC) technology has driven a new branch of semiconductor physics. Although there are many reasons to make nanocrystals, one is to minimize crystal defects to improve their function. A smaller crystal leaves fewer opportunities for defects to form, depending on the synthesis method used. Additionally, NCs tend to be capped with a *ligand*, which completely surrounds the NC, chemically bonding with surface states. Surface states of a crystal can serve as traps if unbonded electrons exist. Ligands can reduce trap states and physically protect the crystal from degradation from exposure to the elements.[16]

One can take this further to create a *quantum dot* (QD). While a NC falls in the size range of about 1-100 nm, a QD is about 1-10 nm. What really distinguishes the two are that a QD has a diameter which is on the order of the wavelength of the electron wave functions. This creates a scenario called quantum confinement, which effectively re-quantizes the energy levels. In this way, a QD starts to look like a single atom in terms of its optical characteristics. As the size of the crystal decreases, the electronic energy levels split, going from continuous bands to discrete states. As this happens, the difference in energy between the highest occupied state and the lowest unoccupied state increases from the original band structure. One consequence of this is that the fluorescence of the crystal (if it exhibits PL) blueshifts toward higher energies.

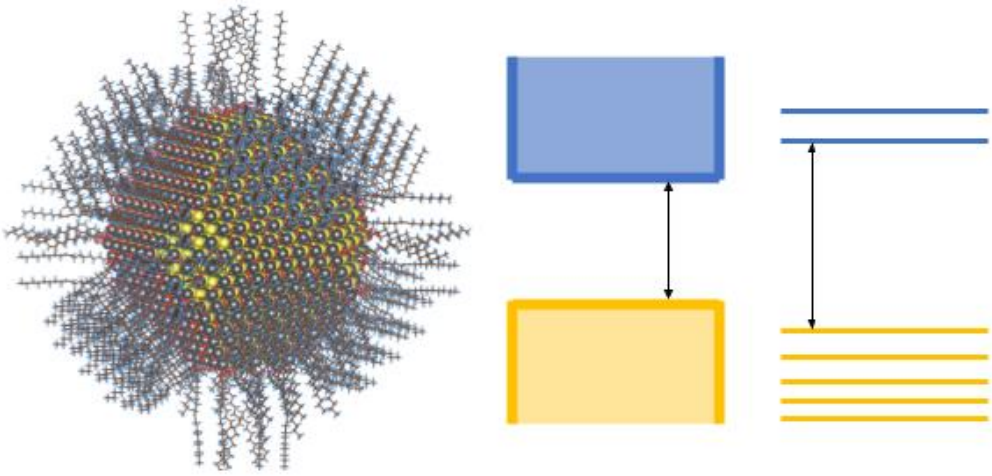

Figure 16: Quantum Dot Structure and Energy Level Splitting

Quantum Dot Synthesis

Quantum dots may be synthesized in many different ways. Here, I will provide one such way which is particularly well suited to a chemistry wet lab with few specialized instruments. Specifically, we will highlight a process used for formation of CsPbBr3, a green emitting fluorophore. Ligand Assisted Reprecipitation Process (LARP) takes advantage of the solubility mismatch of precursors in polar and nonpolar solvents. First, CsBr and PbBr2 are dissolved in a fairly polar solvent such as dimethyl formamide (DMF). Ligand species to be used are then codissolved in the same vial. The goal here is to have all solutes be dissolved, but just barely so that any change in environment could cause them to drop out of solution. [17]

Table 1: Mixing ratios for perovskite quantum dots (modified from Enlow, et.al)

Precursor/ Chemical	*Molar Mass (g/mol)*	*Mass to Add (mg)*	*Volume to Add (μL)*	*μMol Present*	*Moles per mole Cs*
CsBr	212.809	42.56	-	200	1
CsCl	168.36	33.67	-	200	1
$PbBr_2$	367	183.50	-	500	2.5
$PbCl_2$	278.1	139.05	-	500	2.5
Oleic Acid (OA)		-	126.2	400	2
Oleylamine (OLA)		-	131.6	400	2
Toluene	92.14	-	1000	-	5 (L/mol_{Cs})

To effectively facilitate this process, a separate vial of a nonpolar solvent (like Toluene) is prepared with a stir bar placed in it. The vial is set on a stir plate and allowed to spin at a high RPM, until a noticeable vortex is formed. The precursor solution is then pipetted directly into the vortex, whereby its solutes quickly crash out of solution. If the correct ratios are maintained, this will lead to growth of perovskite crystals. It is, however, undesirable to maintain this reaction for too long, as larger crystals will form which have little to no PL qualities. To this end, the codissolved ligands serve to bind to surface sites as the crystals form. When the surface is completely covered in ligand, it can no longer grow any larger and the size is essentially capped. A higher ratio of ligand to precursor achieves a smaller quantum dot, and is typically desired.[18]

General Characterization Methods

Photoluminescence Spectroscopy

Emission spectra for luminescent materials are taken by illuminating a sample with a beam of monochromatic light at a specified wavelength, and detecting what wavelengths are emitted by the sample. The excitation light source is a pulsed xenon lamp, and its wavelength selected by way of a diffraction grating monochromator. This beam falls incident on a sample at an angle which minimizes the amount of reflected light to the detector port, as shown in figure 18.

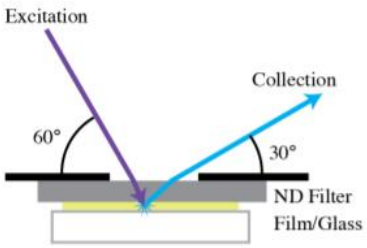

Figure 17: Surface PL Diagram

Photoluminescence (PL) from the sample is emitted isotropically (in most cases, barring any intentional molecule orientation). This leads to a fraction of this light being waveguided to the edge of the glass slide, and the remainder "escaping" from the surface and refracting at angles dictated by Snell's Law. As such, only a small percentage of PL undergone is actually seen by the detector. However, despite this fact, the detector can often become saturated with a strongly fluorescing sample. In this case, a neutral density filter is placed between the beam and sample, attenuating both the incoming and outgoing light. A monochromator on the detection side is scanned in the specified range to yield a PL spectrum in this way.

UV-Vis-IR Absorption Spectroscopy

Our absorption spectrophotometer works with two monochromators running in tandem. White light from the source is fed into the first, which sets the wavelength of light incident on the sample. Transmitted light enters the detection monochromator grating which is set to the same wavelength as the first. By scanning the two synchronously, one can determine the transmission coefficient for a range of photon wavelengths. The following equation relates the measured transmission to absorption coefficients.

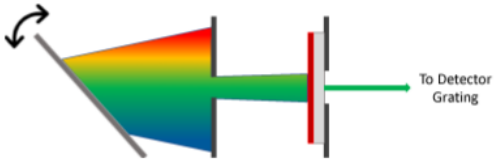

Figure 18: Transmittance/Absorbance Schematic

$$I_0 = I_t + I_a + I_r \tag{5}$$

Since the light source serving as the input has a known intensity (I_0) per wavelength, and the transmitted light (I_t) is directly measured, two of four of the above terms are immediately known. If there were no reflected light, it would be a simple matter to say that…

$$I_a = I_0 - I_t \tag{6}$$

...and obtain a value for absorption to be further interpreted, but not having information about the reflected light complicates matters. One way around this is to configure a second detector positioned to directly measure the light that is reflected by the sample. For this to work, the sample must be placed with its normal angle

bisecting the angle between source and detector, necessitating rigorous alignment procedures. However, it is much more convenient to employ the use of a reference sample with no fluorophores (blank sample) and make a reasonable assumption to eliminate the reflectance term altogether. In the case of dyes embedded within a polymer matrix, and if further simplified by orienting the incoming beam normal to the sample surface, the sample reflectance is dominated by the index of refraction of the polymer itself, as governed by the Fresnel Equation:

$$R = \left|\frac{n_1 - n_2}{n_1 + n_2}\right|^2 \tag{7}$$

Normal incidence is the standard for our measurements here, although any angle used would lead to the same simplification. Before we measure a sample spectrum, we measure the spectrum of a blank first. When we do take the spectrum of the sample, the software automatically gives us the sample transmittance as the difference between the reference and sample output intensity readings. Using the subscripts S and R for sample and reference respectively, and adopting the simplified nomenclature $t = I_t$, $a = I_a$, $r = I_r$;

$$t = t_R - t_S \tag{8}$$

...where t is the transmitted intensity of the dye alone, without any interaction with the matrix itself. This is what we want to measure anyway, and it follows that;

$$t = (a_S - a_R) + (r_S - r_R) \tag{9}$$

...and when we enforce the assumption that the two reflectances are equal;

$$t = (a_S - a_R) \tag{10}$$

The end result is that one can obtain a value for absorbed light of a dye by itself, by knowing just the transmission values of a sample and a reference. From here, we can employ the Beer-Lambert Law to obtain values which become useful for data analysis. Specifically, we want a value for absorbed light which scales with thickness and dye concentration of our sample. This value is known as absorbance (A);

$$A = log\left({I_0}/{I_t}\right) = -log(T) \tag{11}$$

...where transmittance (T) is the proportion of transmitted intensity to source intensity. We can specify the scalability of absorbance with the equation;

$$A = \varepsilon cd \tag{12}$$

...where c is the concentration in moles per unit volume, and d is the path length of light through the material. The quantity ε is known as the molar absorption coefficient (or extinction coefficient), and is a constant for a given material. This quantity will appear in a future section when we discuss energy transfer. Utilizing absorbance becomes necessary when refining absorption and PL data. Either we can use precise thickness measurements to confirm that two samples have the same dye concentration, or we can assume the same concentration and account for small

differences in sample thickness by scaling the data match at critical wavelength values.

Quantum Yield Measurements

Photoluminescence quantum yield (PLQY) is a measure of how efficiently a molecule or material fluoresces the light that it absorbs. Specifically, it is the ratio of number of photons emitted to the number of photons absorbed by the material from some excitation source. The excitation should be monochromatic light, and although the definition leaves some ambiguity, is commonly set at or near the peak absorption wavelength. For typical materials, unless a rare phenomenon called *photon downconversion* occurs, the maximum realized PLQY is 1, meaning that every electron promoted to an excited energy level relaxes back into the ground state via a fluorescent pathway. Molecules which have fewer and lower energy complex vibrational pathways tend to exhibit higher PLQY. It has been reported that certain fluorophores benefit from higher concentrations, where the ensuing aggregation leads to a stiffening of the molecule's "backbone"[19]. However, typically the opposite is true. When a molecule's PLQY decreases upon increasing the concentration, this is called "concentration quenching". As follows from Beer's Law;

$$Absorbed\ Fraction = 1 - 10^{-A} \tag{13}$$

Integrating sphere:

For measurements which require a tally of all input and output photons, an integrating sphere is often the tool for the job. As expected, this instrument is a hollow sphere (typically 4”-10” diameter?) whose inner surface is coated with highly *diffusively reflecting* white paint. This sphere has several ports for the purpose of 1.) Letting light in from a known source 2.) Letting light exit toward a spectrophotometer 3.) Inserting a sample. Light can be introduced to the chamber by way of a light guide (either liquid or fiber optic) or a system of lenses and a cutoff filter placed in the input port. With no sample in the sphere, input light will simply reflect (diffusely) off the interior surface many times, before ultimately encountering the exit port which leads to another light guide. With a sample in place, a fraction of the input light passes through and is directed to the output, while the remainder is either absorbed or reflected by the sample. The portion of absorbed photons which lead to fluorescence are now shifted to a lower energy, and likewise reflect off the inner surface until encountering the output port. By integrating the total photon count before and after a threshold value, we can obtain the ratio of emitted and absorbed photons yielding our PLQY.

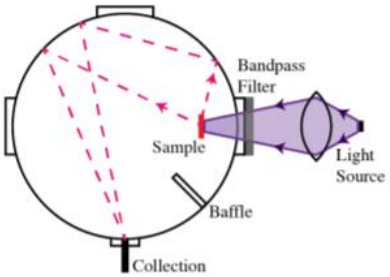

Figure 19: Integrating Sphere Cross Section

This calculation; however, requires a precise relationship between photon energy and photon “count” within the spectrophotometer. This may be determined by calibrating the spectrophotometer with a light source of broad and very well-known

spectrum. Commonly, a tungsten/halogen light source is used for this purpose. When a stable current is sent through this incandescent style bulb, a precise blackbody curve is produced.

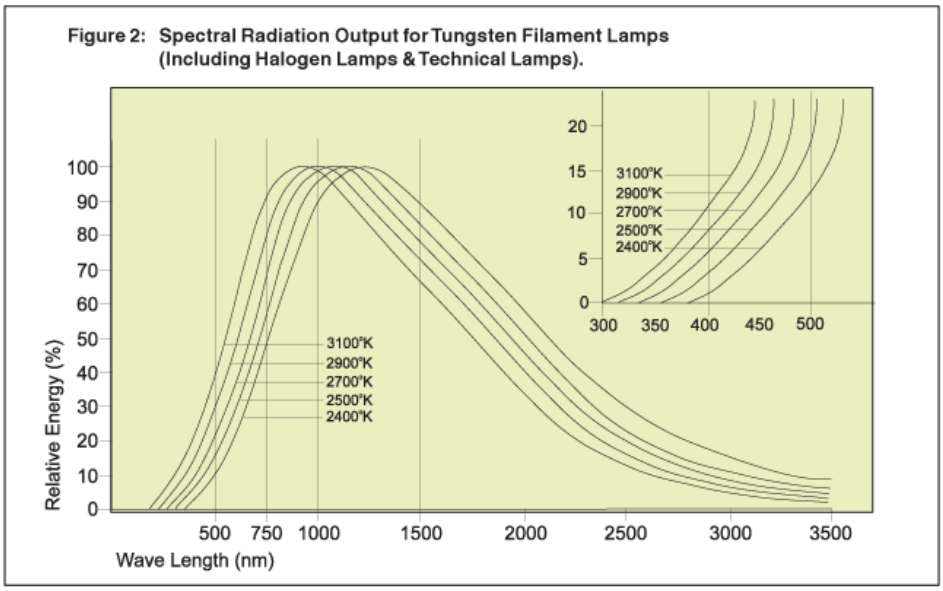

Figure 20: Spectrophotometer Calibration Light Source Spectra

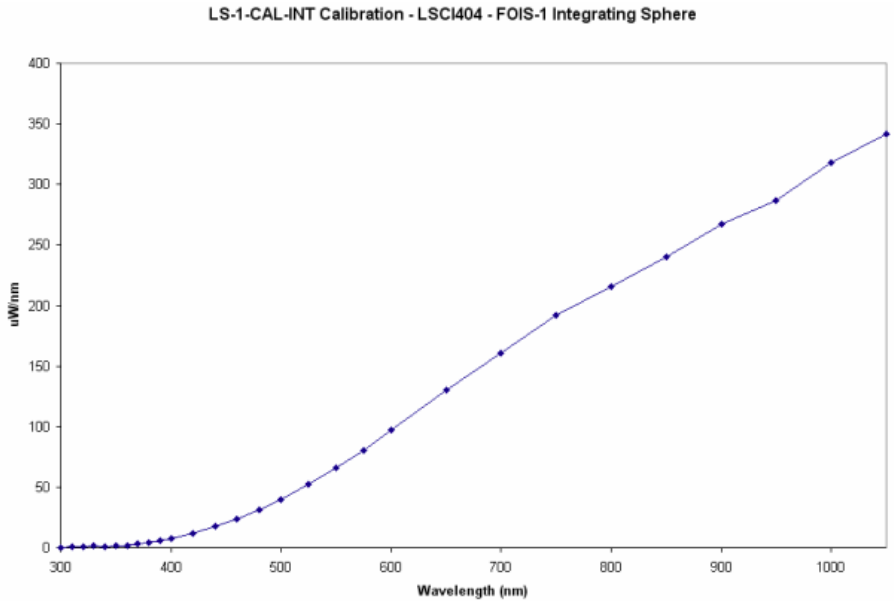

Figure 21: Calibration Curve for Integrating Sphere

Inaccuracies will be noticed if there is a low photon count for a given range in the spectrum for the calibration light source, however. To sidestep this issue, a *relative PLQY* may be calculated as follows.

$$\varphi_S = \varphi_R \frac{I_S - I_B}{A_B - A_S} * \frac{A_B - A_R}{I_R - I_B} \tag{14}$$

...where φ is the PLQY, subscripts S,R, and B represent the sample, reference, and background respectively, I and A represent the spectrometer photon counts in the emission and absorption ranges respectively. This technique takes advantage of a dye with a well-known quantum yield over the range tested, effectively calibrating the count number using this second sample itself. In the case of these UV dye studies, Lumogen Violet 570 (LV570) was used, which has a perfect PLQY of 1 in this range.

Relative measurements were taken in this case, because of the weak UV emission of our calibration lamp, as illustrated above.

Coupled to the integrating sphere is an Ocean Optics Jaz spectrophotometer. It senses photons by way of a linear array of silicon transistors or a charged-coupled device (CCD). Therefore, the maximum detectable wavelength is roughly 1100nm, corresponding to silicon's bandgap energy of 1.1eV. A high enough flux of photons incident on the CCD results in a small current, and manifests as a number of "counts". This particular device has a saturation point of about 60,000 counts. Therefore, one must set the integration time within the software to limit the number of incoming photons and get accurate results. The user may also specify the number of scans to average. A higher number results in smoother data, eliminating some of the noise.

Multiple Dye Interactions

For reasons previously discussed, organic dye systems tend to absorb light only in a narrow range of wavelengths. However, LSCs display higher gain the more incoming light they actually absorb. Since the sun is closely approximated by a blackbody of temperature 5000k, green light is the most abundant, with a sharp decline in the UV-A region. One way of absorbing more broadly over this range is to incorporate multiple dyes which have complementary absorption spectra. Another motivation for using multiple dyes is to tune the color of the LSC, often striving for a broad, neutral density absorption over the entire visible range resulting in a "tinted

window" look. Now one must consider interactions between two or more dye species, as molecules which absorb in a higher energy range may emit at wavelengths which fall into the absorption range of the second dye.

Radiative Transfer:

The simplest type of interaction different species of dye in such a system may perform is based on the transfer of energy with an intermediate photon. In the two-dye example, the species with the higher HOMO-LUMO gap, hereafter referred to as the *donor*, absorbs a photon and emits a lower energy photon via fluorescence. Then, the species with the lower HOMO-LUMO gap, hereafter referred to as the *acceptor*, absorbs the PL photon from the donor and emits a second photon of even lower energy. If this photon avoids the LSC loss mechanisms, it will then be absorbed by the PV and add to the photocurrent. Energy transferred in this way; however, is subject to quantum yield losses from both donor and acceptor.

$$\boldsymbol{\eta} = \frac{\boldsymbol{\varphi_D} \int_0^\infty \boldsymbol{\Phi_{sun}}(\lambda)(\mathbf{1} - \mathbf{10}^{-\boldsymbol{A_D}(\lambda)})\, \boldsymbol{d\lambda} * \boldsymbol{\varphi_A} \int_0^\infty \boldsymbol{PL_D}(\lambda)(\mathbf{1} - \mathbf{10}^{-\boldsymbol{A_A}(\lambda)})\boldsymbol{d\lambda}}{\left(\int_0^\infty \boldsymbol{\Phi_{sun}}(\lambda)\, \boldsymbol{d\lambda}\right)^{\mathbf{2}}} \quad (15)$$

Donor candidates for LSCs should fall close to the UV range, which presents a problem since UV fluorescent dyes often have either low PLQY or degradation issues. Many carbon bonds have a binding energy which coincides with photon energies of UV light. This leaves them susceptible to damage under UV radiation.

While UV blockers are often added to polymer systems to counteract this, these blockers would negate the utility of a UV fluorophore, since they would compete for UV absorption. Thus, it would be ideal to find another transfer mechanism which does not involve the emission of the initial photon.

Forster Resonance Energy Transfer (FRET):

When an electron is promoted into an excited molecular orbital, this creates a transient dipole moment. Forster figured out that this action has the ability to create a local dipole field, which may induce an excited state in a neighboring molecule if certain conditions are met. First, the donor PL spectrum must overlap sufficiently with the acceptor absorption spectrum. The figure of merit for this is known as the *overlap integral (J)* and is the result of taking a normalized integration of the two.[20]

$$J(\lambda) = \frac{\int_0^\infty F_d(\lambda) * \varepsilon_a(\lambda) * \lambda^4 \, d\lambda}{\int_0^\infty F\,(\lambda)\, d\lambda} \tag{16}$$

Here, ε is known as the *extinction coefficient* and is given by dividing the absorbance spectrum by the thickness of the film. It is a material constant, making calculations convenient. Variables are subscripted with *a* or *d* to denote acceptor and donor.

This interaction is also acutely dependent on the separation distance between the dipole active parts of both molecules. Following from the inverse cube dipole dependence on distance, FRET efficiency actually goes as 1/r^6.

$$E_{FRET} = \frac{1}{1 + \left({}^{r}/_{R_0}\right)^6} \tag{17}$$

Here, R_0 is a parameter defined as the separation distance at which a two dye system will experience 50% FRET Efficiency, known as the FRET critical distance. This is a convenient way to visualize the functionality of it. However, for experimental determination, the following form is more useful;

$$E_{FRET} = 1 - {}^{F_{da}}/_{F_d} \tag{18}$$

The functional form of the parameter R_0 will be described in a future section covering the experiment carried out to investigate the effects of FRET. For the moment, though, it is important to address exactly how resonance transfer skirts around the quantum yield losses incurred by radiative transfer. As will be seen, the QY of the donor does appear in the calculation for the FRET critical distance, specifically, $R_0^6 \sim \varphi_d$. The key here is that the functional form does not depend linearly on donor QY, because of the extra +1 term in the denominator. Below is a plot of many overlaid FRET Efficiency curves, each assuming a different ratio of separation distance to R_0. For the sake of ease, I have set this ratio as if the quantum yield were unity. However, the x axis shows a variable donor QY.

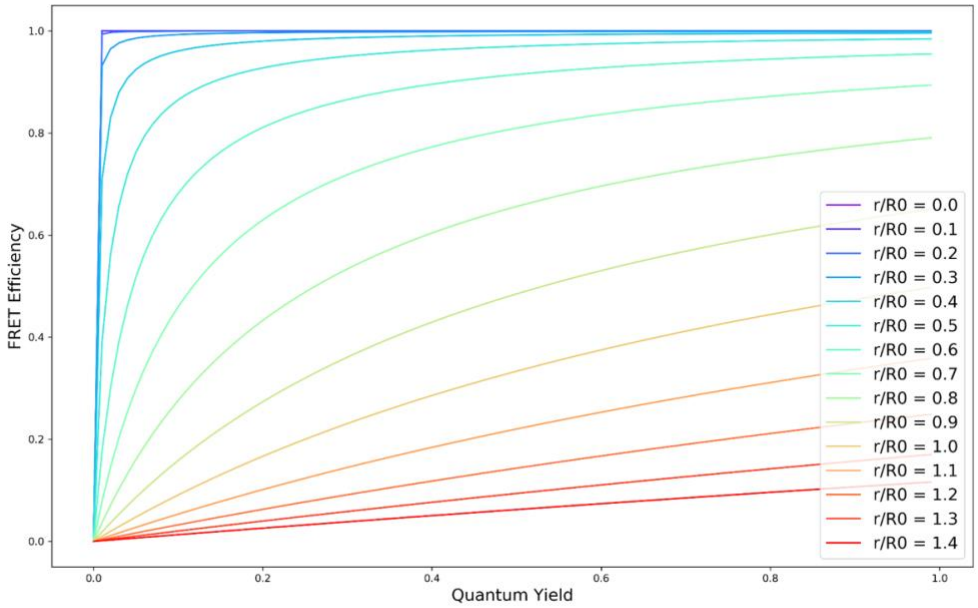

Figure 22: Response of FRET Efficiency to changes in donor QY

Another factor which favors FRET over radiative transfer is a lowered chance for photon reabsorption. If a donor emits a photon, it will have some probability of being intercepted by another donor before it can make its way to an acceptor. If the donor has a low QY, this would incur a loss. However, with resonance transfer, there is no intermediate photon to be absorbed, and the system should experience only minimal reabsorption losses.

Exploring Dye Combinations

When computing PLQY of a dye whose PL peak lies close to the excitation light source wavelength, extra steps become necessary. This is due to the fact that

there is overlap between the excitation and PL counts, making it impossible to simply set a threshold wavelength between them to stop counting one, and start counting the other. Although in this case, the overlap is quite low, it is still good practice to perform a deconvolution.

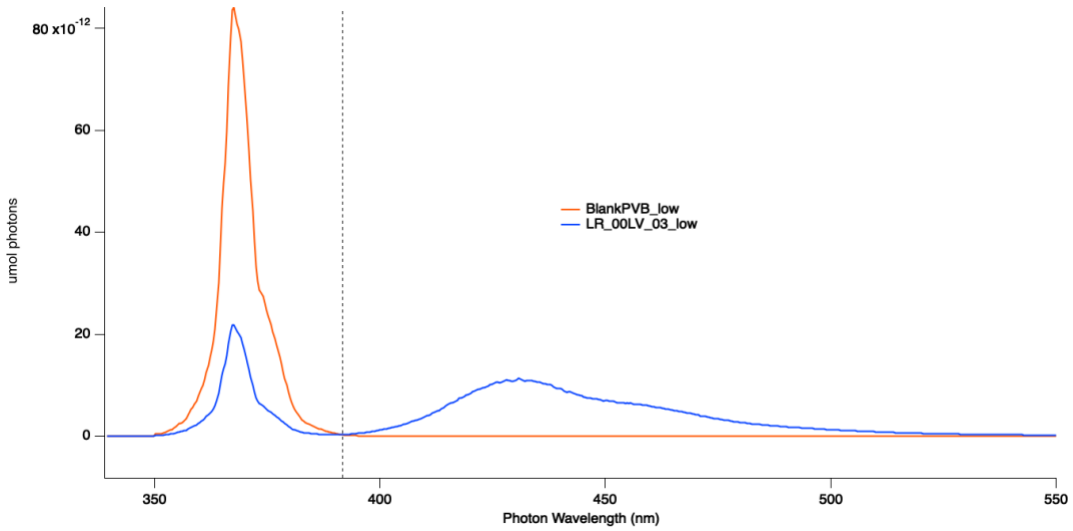

Figure 23: Decomposing Excitation and PL Spectra from Integrating Sphere

A python script was written to perform a least squares fit of a scaled excitation peak from the blank sample, to that of a sample, within a specified region. This fit yields the deconvolved excitation light remaining after passing through the sample, and works well as long as absorption is consistent over the range of the peak. By subtracting this peak from the data, a pure LV570 PL peak can be obtained. To count photons in each region, each deconvolved peak is now used during the integration. Here, because of the presence of two dyes, we break the spectrum into three distinct regions: excitation (UV), LV570 PL (Blue), and LR305 PL (red). There is no need to

deconvolve between the two dyes as there is a large gap in wavelength between the two.

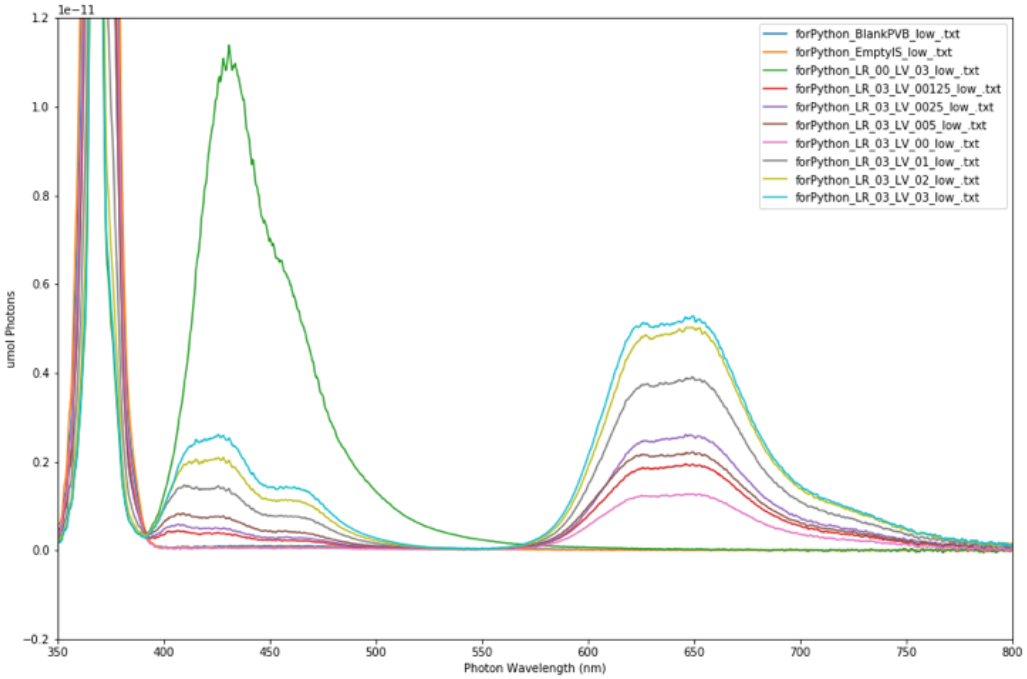

Figure 24: LR305 and LV570 Combination Integrating Sphere Spectra (raw data)

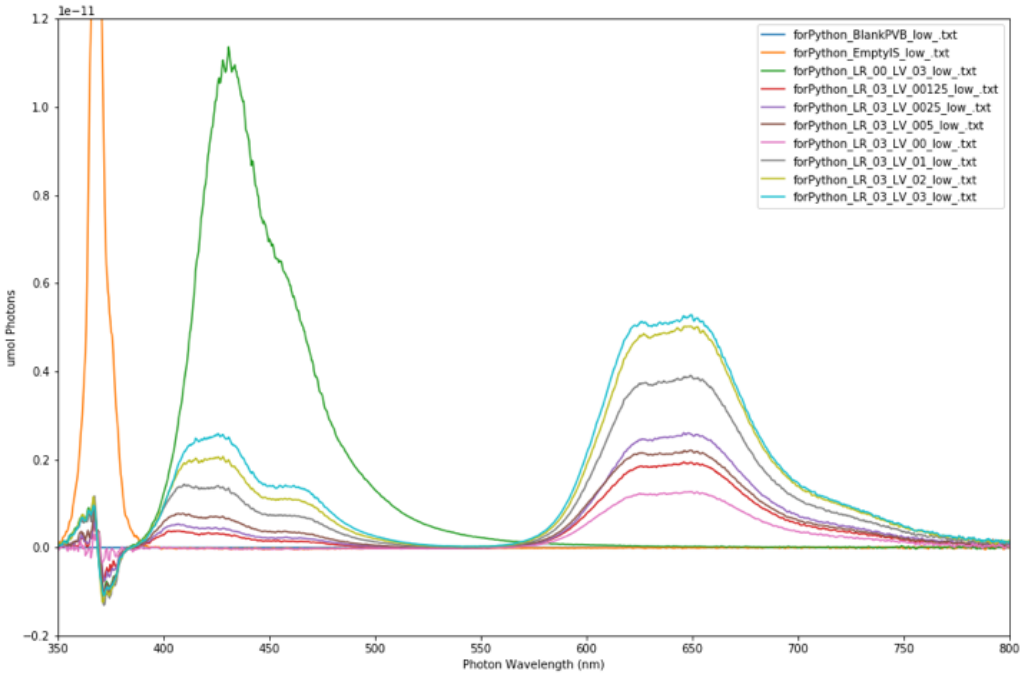

Figure 25: LR305 and LV570 Combination Integrating Sphere Spectra (excitation peak subtracted)

In all, six combinations of the two dyes were tested with mixing ratios ranging from 1:1 to 1:24 (LR305:LV570). Additionally, pure LR305 and LV570 samples were made with the maximum single dye concentration of 0.03% by weight each, as well as a blank PVB sample. Integrating sphere measurements were made under both UV and white light illumination. UV excitation was used to determine quantum yield of both individual dyes and in combination. Shown below are all samples before and after performing the UV peak subtraction.

Light excitation is provided by a UV LED emitting with a peak wavelength of 380 nm, and a 400 nm high pass filter placed in line. Experiments were performed at two different light intensities, achieved by operating the LED at two different currents

using a Keithly programmable power supply. For low intensity excitation, the current was limited to 50mA, and was limited to 500mA for a 10 fold increase for high intensity. The integration times were set to 250ms and 1000ms respectively, so as to not saturate the detector.

Table 2: Low intensity excitation, LR305 and LV570 combo summary table

LV570 % by Weight	LR305 % by Weight	Dye Ratio	Percent Absorbed	PLQY	LR/LV PL Ratio
0	0.03	0:1	0.12	1.12	inf
0.00125	0.03	1:24	0.19	1.28	8.49
0.0025	0.03	1:12	0.30	1.07	7.68
0.005	0.03	1:6	0.29	1.08	4.36
0.01	0.03	1:3	0.54	1.01	3.82
0.02	0.03	1:2	0.67	1.06	3.42
0.03	0.03	1:1	0.73	1.08	2.99
0.03	0	1:0	0.75	1.02	0.01

Table 3: High intensity excitation, LR305 and LV570 combo summary table

LV570 % by Weight	LR305 % by Weight	Dye Ratio	Percent Absorbed	PLQY	LR/LV PL Ratio
0	0.03	0:1	0.18	0.39	inf
0.00125	0.03	1:24	0.26	0.51	4.65
0.0025	0.03	1:12	0.37	0.47	4.42
0.005	0.03	1:6	0.37	0.48	2.64
0.01	0.03	1:3	0.59	0.51	2.41
0.02	0.03	1:2	0.72	0.56	2.22

0.03	0.03	1:1	0.76	0.57	1.96
0.03	0	1:0	0.79	0.69	0.01

A few important trends emerge from the integrating sphere data. For one, the PLQY for all samples is much higher during low intensity excitation. At the same time, the percent of light absorbed is about the same between the two intensities. This indicates that, although the material is able to absorb the same fraction of incoming photons, more of that energy is converting to heat as the excitation intensity goes up. This illustrates a well-known phenomenon of excitation saturation of a dye. A fluorescence event takes a certain amount of time to proceed, on the order of nanoseconds to microseconds (these particular dyes being on the low end of this range). As a result, if a molecule has not yet relaxed but is encountered by an absorbable photon, it will not be able to emit a second downshifted photon. This results in the dye heating, and over long periods of time may even degrade the molecule.

One important aspect of an LSC is the spectrum of light it imparts to the plants below. Using a white light excitation from a solar simulator, we can investigate the total photon output from an LSC system. Because this is performed inside an integrating sphere, the data will reflect both direct and waveguided light. If coupled to PV cells as is typical for a system like this, the waveguided light would be absorbed by the cells, and would not add to the spectrum seen by the plants. However, we will

take this to be an indicator of overall spectral shifting capacity of the LSC dye system.

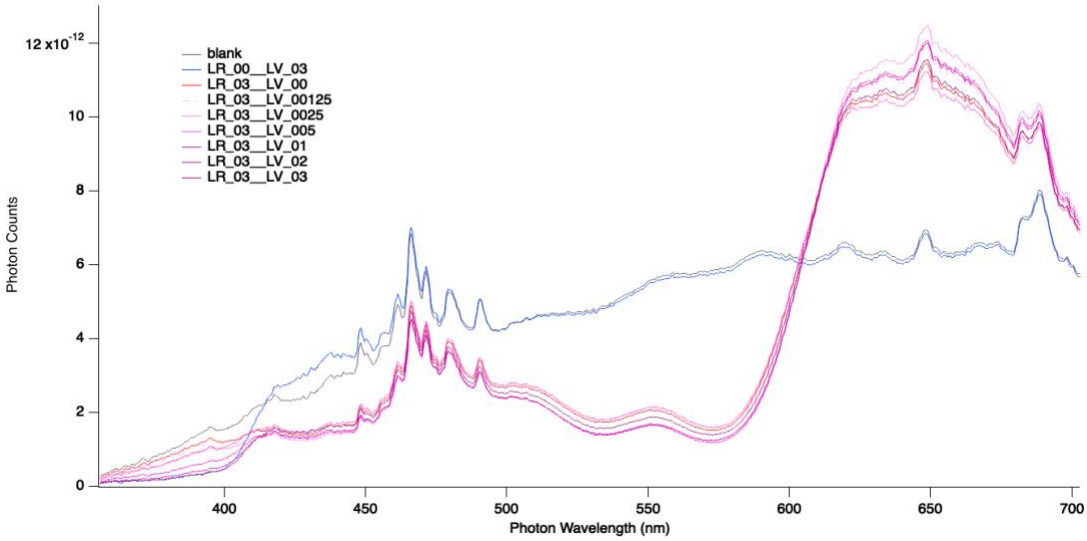

Figure 26: LR305 and LV570 Combination Integrating Sphere Spectra (white light excitation)

It is clear from the plot that only samples which contain the LR305 have a considerable impact on the spectrum. LV570 on its own does noticeably remove UV light and replace it with an excess of blue light. For the combination samples, the amount of UV subtraction occurs linearly with the amount of LV570 added. However, any addition of blue light from the LV570 is overshadowed by the absorption of LR305 in that region. This is still a potential benefit to the plant, though, because of the increase in red light imparted as energy is transferred, either radiatively or via FRET, to the acceptor dye LR305. Reduction in UV light is a

benefit since plants cannot utilize those wavelengths, and it is even involved in degradation of plastics in the waveguide or even the plants themselves. Even with this in mind, we can observe that the changes are only slight due to the relatively low flux of UV light in proportion to other wavelengths.

Aggregation Induced Forster Resonance Energy Transfer in Multi-dye Luminescent Solar Concentrators

Dye Selection

To enhance the gain factor and overall effectiveness of our LSCs, any additional dyes used should be chosen to have absorption ranges which have

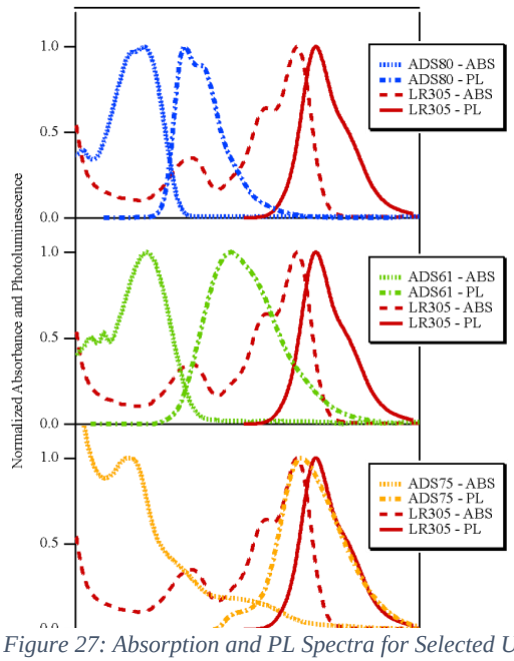

Figure 27: Absorption and PL Spectra for Selected UV Dyes Overlaid with LR305

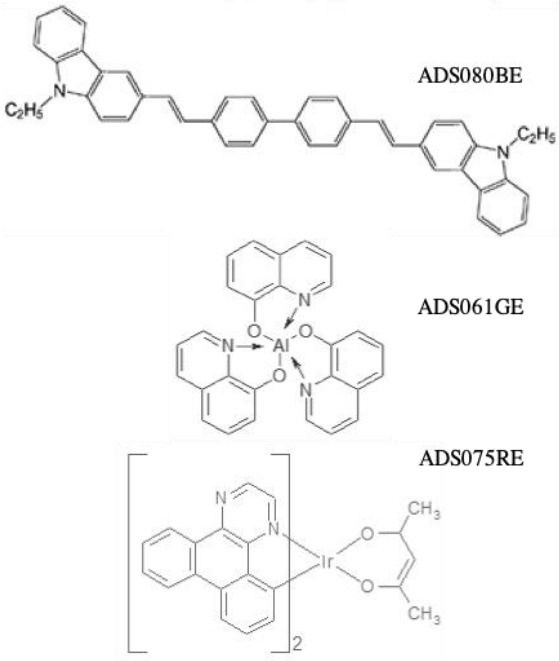

Figure 28: Molecular Structures of Selected UV Dyes

minimum overlap with that of LR305, yet maximum overlap with the AM1.5 spectrum. Additionally, they should exhibit sufficiently high quantum yield and low rate of degradation when exposed to UV light. Since the fluorescence from the UV dye falls in a usable range, it is permissible for its PL spectrum to avoid overlap with LR305 absorption. In general, having a high overlap here leads to efficiency losses due to less than unity QY of the acceptor. However, a high overlap can prove beneficial at high concentrations if the donor has a relatively low QY because of the effect of FRET. To satisfy these requirements, three commercially available UV dyes from *American Dye Source* were chosen to study, ADS080, ADS061, and ADS075. Like many fluorophores, the first two of these molecules exhibit a multitude of aromatic rings arranged symmetrically about their center of mass. This type of ring structure tends to lead to high fluorescence due to singlet state excitations made possible by conjugated π-π bonds. Furthermore, PLQY of molecules which have aromatic rings stacked tightly, instead of connected by single bonds, benefit from the rigidity provided by this type of connection.[21]

Another consideration for dyes is they must be soluble in a compatible solvent with the polymer into which they are introduced. This turns out to be one of the biggest challenges in the study. Not only should it dissolve both ingredients, but it should have a low enough partial pressure (and thus evaporation rate) to leave a high quality film. If the solvent evaporates too quickly, it leaves bubbles in the film as it dries, which are difficult to completely remove during post processing.

Experimental Design

Light emitting oligomer ADS080BE and light emitting metal complexes ADS061GE and ADS075RE (American Dye Source) were dissolved at 0.5 g/L in non-polar solvents 4-methylanisole, chlorobenzene, and 1,2-dichloroethane (Fisher), respectively. Lumogen F Red 305 (BASF) was dissolved at 3 mg/mL in each of the solvents. For simplicity, we will henceforth refer to the fluorophores as ADS80, ADS61, ADS75, and LR305, listed here in order of increasing wavelength emission spectrum. Solutions were mixed with poly-methyl methacrylate (350,000 MW, Spectrum Chemical) at various concentrations to evaluate dyes individually and blended (ADS with LR305), in a thick cast and a thin, doctor-bladed form.

Sheet Cast Samples

Individual fluorophores were combined with polymethyl methacrylate (PMMA), dissolved at approximately 150 mg/mL in the corresponding dye solvent, at 0.03% dye to PMMA by weight, selected for the similarity of the LR305 absorbance to that of previous work. Combinations of the ADS and LR305 dyes were added to the PMMA solution each at 0.03% dye, for a net dye concentration of 0.06% by weight. The solutions were cast into a thick sheet by depositing the solution into an aluminum dish and removing the solvent via a vacuum oven set to 75 C for 72 hours. The resulting pucks were pressed into 550 μm +/- 50 μm sheets by hot press, with dual platens heated to 125 C and pressing at 90 PSI. Sheets were cut into 1 cm x 2 cm samples by hot knife.

Doctor Bladed Samples

Individual and combination solutions were mixed with PMMA at 200 mg/mL in the corresponding solvents. Low concentration samples of individual fluorophores were set at 0.03% for LR305 and ADS80, and at 0.04% and 0.05% for ADS61 and ADS75, respectively, to catalog spectra for each fluorophore in PMMA without interference of reabsorption. For FRET studies, the concentration of LR305 was held constant at 0.3% dye by weight, similar to fabrication techniques in previous work. Concentrations of the UV dyes were set based on testing at various concentrations; ADS80 was set to 0.3%, ADS61 to 0.4%, and ADS75 to 0.5% dye by weight. These concentrations were used in samples of the individual fluorophore and in combination with LR305. The fluorophore/PMMA ink solutions were deposited onto 3 in x 1 in borosilicate glass slides via the doctor blade method, using an Industry Tech Auto Draw III automatic drawdown machine. 3M Scotch 810 Magic tape was adhered at the edges of the slide to set the blade height, giving films 2 – 7 μm thick, depending on the solvent used.

Characterization

Absorbance measurements were taken with a Jasco V670 spectrophotometer, using a clear PMMA sample or glass slide as a baseline. The molar extinction coefficient for LR305 was calculated using spectra from this instrument, with a peak decadic absorbance of 0.9737, corresponding within error to other reported values.[9], [20], [22], [23]

Surface fluorescence was measured with a Perkin Elmer Fluorescence Spectrometer LS-45, which excited samples with monochromatic light incident at 30° and detected photoluminescence (PL) at 60° from the surface, illustrated in Figure 1 a). Optical density filters (Newport FSR-OD30 and -OD50, optical densities 0.3 and 0.5, respectively) were used to prevent saturation of the detector. Excitation spectra were taken in the same setup, with the emission set at 610 nm and excitation ranging from 300 nm – 550 nm. Any comparisons of PL between samples using this instrument were made with the same filter in place. Measurements were performed on both low concentration and high concentration samples.

A 4" integrating sphere (Labsphere) coupled by fiber optic to an Ocean Optics Jaz spectrometer (350 – 1050 nm range) was used for quantum yield of low concentration sheets. Samples were suspended 0.75" from the light source port to ensure proper blocking from the baffle, seen in *figure 20*. UV excitation was provided by a 365 nm LED, powered by a DC power supply, focused on a 5 mm square at the sample after passing through a 325-385 nm bandpass filter (Thorlabs). The power density of the excitation light after entering the sphere was 2.3 mW/cm^2.

The spectrometer power density, and thereby photon count, was calibrated with a Labsphere calibration lamp across the visible range; unfortunately, limited light in the UV region prevented accurate calibration in that range. Quantum yield, φ, was therefore calculated using a relative measurement by

$$\varphi_S = \varphi_R \frac{I_S - I_B}{A_B - A_S} \frac{A_B - A_R}{I_R - I_B} \quad (19)$$

where *I* is the integrated emitted photon count, *A* the integrated absorbed photon count, and subscripts *S, R, B* representing the sample being tested, the reference sample, and a blank (clear) sample, respectively.[24], [25] As a reference sample, Lumogen F Violet 570 (BASF) was cast at 0.03% by weight in the same sheet method given above. The 100% quantum yield of LV570 in PMMA and its high absorption of UV light made this ideal for comparison against the variety of emitters when combined with the calibration lamp.

FRET critical distance, R_0, in high concentration films was calculated from the relation

$$R_0^6 = \frac{9000 \ln(10) \kappa^2 \varphi_d}{128 \pi^5 N_A n^4} \frac{\int_0^\infty F_d(\lambda) \varepsilon_a(\lambda) \lambda^4 d\lambda}{\int_0^\infty F_d(\lambda) d\lambda} \quad (20)$$

κ^2 being the dipole orientation factor, taken to be 0.476 as reported in Steinberg et al,[26] φ_d the quantum yield of the donor particle, N_A Avogadro's number, *n* the index of refraction of the host medium (1.49 for PMMA), F_d the donor emission spectrum, ε_a the molar extinction coefficient spectrum of the acceptor particle, and λ the wavelength.[20], [27] Quantum yield was calculated from the integrating sphere measurements, as given above, emission spectra were taken from the LS-45, and molar extinction coefficient calculated as mentioned previously; the integrand was then numerically evaluated using the trapezoidal method.

The efficiency of FRET transfer, *E*, was calculated from taking the ratio of emission of the donor in the presence of the acceptor, F_{da}, to the emission of the donor particle alone, F_d:

$$E = 1 - \frac{F_{da}}{F_d} = 1 - \frac{\tau_{da}}{\tau_d} \tag{21}$$

F_{da} /F_d was determined by integrating the emission of the blend and deconvolution of this into the contributing spectra. The ratio of donor emission in the blend to the emission of the donor alone gives the needed value. Further discussion may be found in the supplementary information.

These calculations ignore the possibility of radiative energy transfer from the donor to the acceptor; however, at these concentrations of ~10^{-4} M, FRET can be expected to be the dominant mechanism of energy transfer. [22]

A final calculation of Förster's relations give the estimated average particle separation, *r*:

$$E = \frac{1}{1 + \frac{r^6}{R_0^6}} \tag{22}$$

As a comparison, and to understand dye behavior and aggregation in the samples, separation was calculated using;

$$r = (N_A c)^{-1/3} \tag{23}$$

...where c is the concentration (M), to find the average center to center separation of dye molecules, assuming a homogenous mixture.[28]

To extract excited-state lifetimes, time-resolved photoluminescence (TRPL) experiments were performed using time-correlated single photon counting on a home-built apparatus. Thin films containing single dyes and dye blends were excited with a pulsed supercontinuum picosecond laser (Super K EXTREME, NKT Photonics) coupled to an acousto-optic filter and an external RF driver (Super K SELECT, NKT Photonics). Measurements were carried out at an 80 MHz pulse repetition rate with fluorescence being measured in a front-face geometry. The excitation pulse was first rotated by 90° by an achromatic ½ λ plate (Thorlabs) before being linearly polarized by a Glan-Thompson polarizer (Thorlabs). Thin films were excited with vertically polarized light (375 nm), and emission was collected at magic angle polarization (54.7°), with the emission wavelength centered at 435 nm for ADS80 and ADS80/LR305 blend, 491 nm for ADS61 and ADS61/LR305 blend, and 575 nm for the ADS75/LR305 blend. Emission from the ADS75 dye was either too weak for detection or the fluorescence lifetime falls outside of the time window of detection of this system. Emitted light was collimated and then focused by a set of achromatic doublets (Thorlabs) onto a Spectra Pro SP-2300 monochromator (Princeton Instruments). A Photomultiplier tube (Becker and Hickl) was used to record the time-resolved fluorescence decay. An SPC-130 photon counting module (Becker and Hickl) coupled to a Simple-Tau 130 table-top TCSPC system was used for photon counting. Collection was carried out until ~10,000 photon counts were reached in the

main channel. Magic angle data was baselined by subtracting the average of the first 30 collected data points (prior to the rise onset). Fluorescence lifetimes were determined via forward convolution with the measured instrument response function (obtained using a scattering Ludox sample) and a sum-of-exponentials model. This was done using the DecayFit (Fluorescence Decay Analysis Software 1.3, FluorTools, www.fluortools.com) MATLAB package developed by Dr. Soren Preus, using non-linear least squares fitting minimization. Goodness of fit was determined by minimization of the chi-squared parameter and by visual inspection of the plotted residuals.

Measurements of both low and high concentration samples were tested under white light for simulation of practical application. For low concentration an Oriel Solar Simulator with xenon arc lamp, filtered with a Newport combined AM0/AM1.5G filter, was coupled to the integrating sphere with a Newport liquid light guide (transmission range 340 – 800 nm). For high concentration, edge emission was detected using a custom setup using the same light source and spectrometer. The resulting spectra can be extrapolated to give approximate enhancements expected in an LSC design based on the parallel layout featured in Corrado et al and similar to commercially available panels.[10] In addition, changes to the blue, green, and red spectrums of light passing to agriculture below may be estimated.

Results

Normalized absorbance and emission spectra of each UV fluorophore and LR305 at low concentration in thin film may be seen in *figure 27*, with details of peak absorbance and luminescence found in Table I. The molecular structure of each dye may be found alongside in *figure*. The ADS dyes show peak absorbance in the UV-A range, with additional absorbance in ADS75 extending farther into the UV. Both ADS80 and ADS61 show limited absorbance beyond the end of the violet portion of the spectra (450 nm), limiting competition with LR305. ADS75, on the other hand, exhibits a significant absorption tail overlapping LR305 absorbance.

Table 4: UV dye combination summary chart

UV dye	λ_{ex}^{max} (nm)	λ_{em}^{max} (nm)	Stokes shift (nm)	A_{Single}	A_{Blend}	φ *Individual*	φ Blend
LR305	577	597	20	0.065	-	0.945 ± 0.048	-
ADS80	385	435	50	0.635	0.699	1.003 ± 0.044	0.979 ± 0.043
ADS61	388	491	103	0.059	0.125	0.264 ± 0.037	0.694 ± 0.042
ADS75	366	579	213	0.639	0.727	0.328 ± 0.015	0.416 ± 0.019

All UV fluorophores show emission within the range of LR305 absorbance, making them prime candidates as donor molecules in both radiative and Förster energy transfer. The emission peak for LR305 registers as 596 nm, as expected with excitation below 400 nm and no reabsorption in the sample.[29] Assuming this holds true for all samples, there should be no shifts to the UV emission spectra as well. ADS80 emission has a shoulder to the right of the primary peak, appearing to approximately reflect the absorbance peak ratio, as expected. While this dye has the lowest overlap integral and misses the majority of LR305's absorbance, it has the potential to contribute to shorter wavelengths also used in photosynthesis that are otherwise reduced by absorption from LR305. However, the short Stokes shift increases the likelihood of reabsorption at higher concentrations or thicknesses, shifting away from peak photosynthetic wavelengths. The emission spectra of ADS61 covers a larger portion of absorption in LR305, including the secondary peak and shoulder, giving it a higher overlap integral with LR305. The higher Stokes shift reduces potential over reabsorption at thicker geometries and higher concentrations. Emission of ADS75 overlaps best with LR305's primary absorbance peak, giving it the highest overlap, largest Stokes shift (and reduced potential for reabsorption), and greatest potential for FRET.

Low Concentration

Sheet samples at a 0.03% concentration were tested for PLQY alone and in combination with LR305 at an excitation of 370 nm, following Equation 20 and using

LV570 as a reference with a yield of 1.000 ± 0.010. [30] These values can be found in Table I and an image of the samples may be found in Figure 16. The spectra of the surface photoluminescence can be found in Figure 3, where each has been scaled by the peak of the most fluorescent sample in the set. By comparing the LR305 – which is the same spectra in each set – we can see that ADS80 is the most intense, followed by ADS75, then ADS61, reflecting trends in absorbance and PLQY.

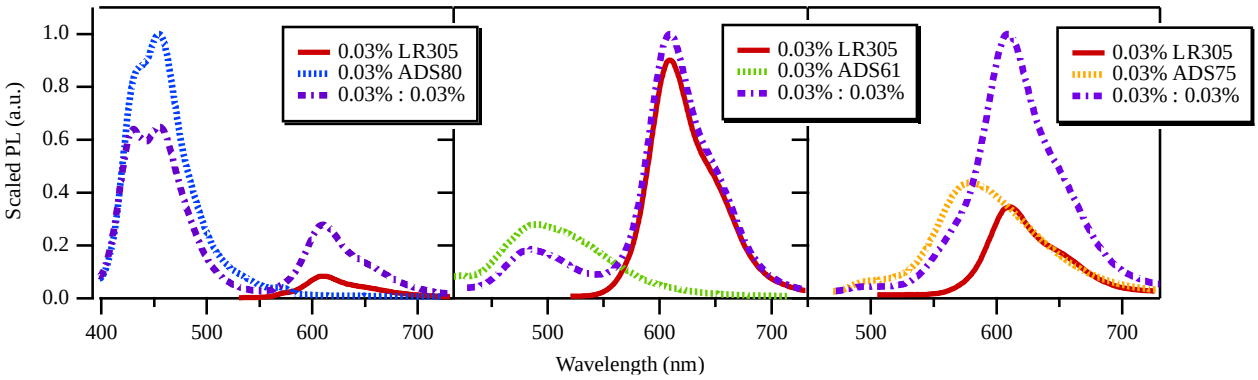

Figure 29: Surface PL Spectra of Dye Combinations in Low Concentration

LR305 gives a PLQY of less than the reported 100%. It is important to note the peak emission of LR305 in our thick samples as 610 ± 1 nm. Wilson et al report the peak emission of LR305, at very low concentration in 3 mm sheets and excited from 320 to 490 nm, at 597 nm, as seen in the thin low concentration samples.[29] This indicates that at our chosen concentration and thickness, we are observing self-absorption and red-shifting due to aggregates in the system. Though Wilson reports 100% QY in the presence of these aggregates – concluding that these must be *J*-

aggregates – it is possible that our system has a very small number of *H*-aggregates, and therefore gives a small loss in quantum yield.[10], [31] The absorbance of the blends approximately follows the expected sum of contributing spectra ($A = \sum_{i=1}^{n} t_i c_i \alpha_i$, where *n* is the number of samples, *t* is the thickness, *c* the molecular concentration, and α the molar absorption coefficient) allowing for slight deviations in thickness and error in concentrations, and can be seen in Figure S1 of the main paper (not included here).[32] The decadic absorbance of each sample at 370 nm is given in Table I.

Table 5: FRET critical distances and efficiencies for UV dye combinations

UV dye	Concentration UV:LR305	R_0 (Å)	FRET Efficiency (SSPL)	FRET Efficiency (FLM)	r (Å)
ADS80	0.3%:0.3%	42.1 ± 1.3	0.61 ± 0.03	0.28 ± 0.02	39.2 ± 1.2
ADS61	0.4%:0.3%	38.4 ± 1.2	0.77 ± 0.03	0.72 ± 0.02	31.3 ± 1.0
ADS75	0.5%:0.3%	42.9 ± 1.3	0.75 ± 0.03	NA	35.6 ± 1.1

High Concentration

By increasing the concentration of our samples an order of magnitude to ~10^{-3} M and working in thin films, we can expect to be solidly in the resonance energy transfer regime with negligible radiative transfer occurring.[22] Minimal reabsorption in the high concentration samples can be confirmed by the emission peak of LR305 excited with 370 nm light. The surface PL of LR305 cast from 4-methylanisole and

chlorobenzene give peaks at 601 nm shown in Figure 31 (for use with ADS80 and ADS61, respectively), and, while not fully eliminating reabsorption in the samples, demonstrate a considerably reduced effect compared with their thick counterparts. In the dichloroethane cast sample (for use with ADS75), the PL and absorbance (SI Figure 5) show the sample is about half as thick as the others and has peak emission at 597 nm. Assuming that this sample still contains aggregates, this indicates the sample is free – or close to free – of reabsorption and will not be subject to radiative energy transfer.

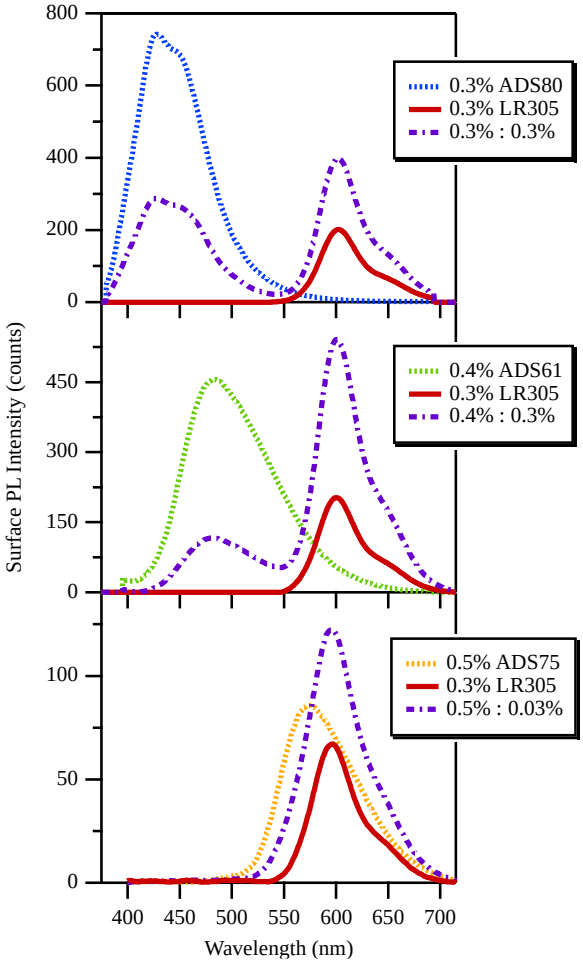

Figure 30: Surface PL Spectra of Dye Combinations in High Concentration

Both low concentration and high concentration samples have shown potential for application in LSC photovoltaic modules. To evaluate the performance of the two-dye systems as a whole, we must understand how they behave under white light. By observing the low concentration samples in the integrating sphere under simulated white light, we can extract expected enhancement in power production of an LSC panel by the fluorophores alone and in combination with LR305, shown in Figure 35 with errors of ±10% of the base value. The reference spectra, along with raw spectra

from each sample, can be seen in Figure S9. By comparing the blended samples with a sheet of un-dyed PMMA, shifts in spectra from incident white light excitation, relative to LR305's performance, inform changes in color tuning of the panel. The power spectra for the sheets, less the reference sheet spectra, can be found in Figure 32, while the relative spectral irradiance can be found in Table 6.

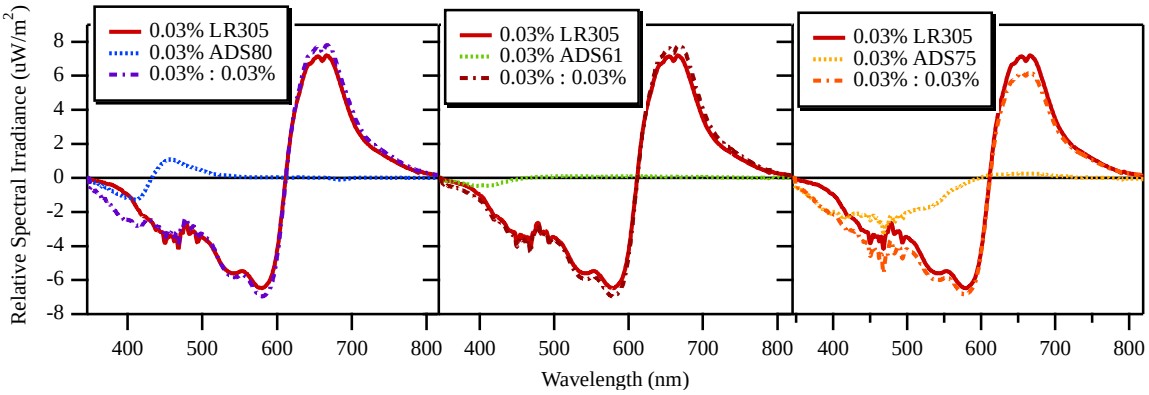

Figure 31: Relative Spectral Irradiance of Low Concentration UV Dyes, Blend, and LR305 Only, Under AM1.5 Illumination

Table 6: UV dye combination relative spectral shifts under white light illumination

Relative Irradiance to LR305	ADS80:LR305	ADS61:LR305	ADS75:LR305
425-500 (Blue)	2.5%	-1.9%	-9.7%
500-600 (Green/Yellow)	-2.2%	-3.3%	-3.9%
600-800 (Orange/Red)	2.8%	2.8%	-3.7%

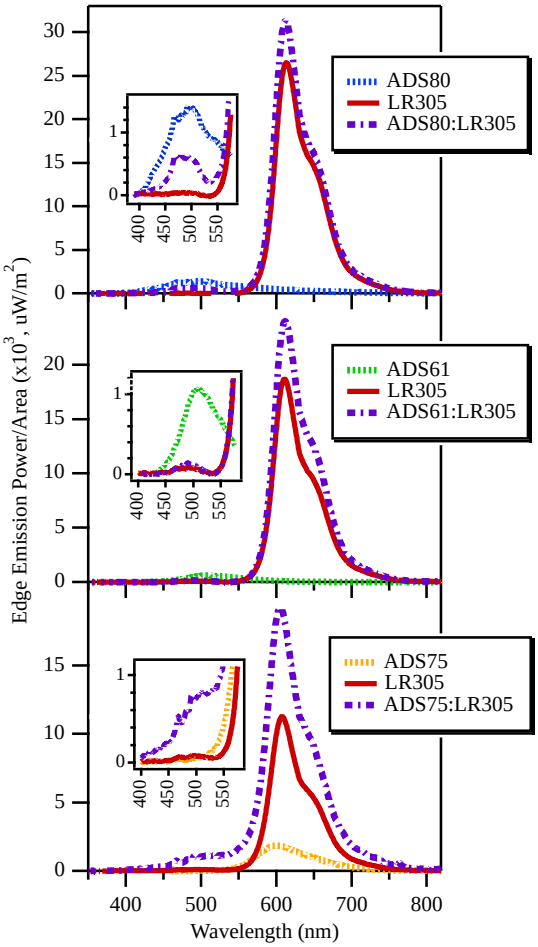

Figure 32: Edge Emission of High Concentration Samples Under AM1.5 Illumination

Conclusions

In ADS80 the small Stokes shift, combined with reabsorption in the sample, leads to the maximum emission appearing at 455 nm and a secondary peak at 431 nm, instead of mirroring the absorption peak intensity as previously seen and further indicating reabsorption in our samples. The other samples show no influence from reabsorption, likely due to their larger Stokes shifts. The ADS80 blend shows even

emission between the peaks in the donor, where the PL coincides with the secondary absorption peak of LR305. In the initial emission event of the blend, the light is split between reabsorption in ADS80 and absorption in LR305, resulting in less PL of the secondary peak compared with the donor alone. In ADS61, there appears to be a blue-shift in the donor emission; the high absorbance of LR305 from 500-550 nm leaves behind light less likely to be absorbed. ADS75, though subtle, can be seen in the broadening of the emission peak, predominantly in the 500-600 nm range. Excitation spectra confirm energy transfer from the donor to LR305 in all blends, though small in ADS61 and ADS75, and can be found in Figure S5.

PLQYs for the individual dyes give ADS80 at near-unity, with ADS61 and ADS75 reporting significantly lower. Though reabsorption is exasperated in the integrating sphere, ADS80's 100% yield is unaffected; the minimal reabsorption in ADS61 and ADS75 should have little effect on the yields. However, the drop in LR305 QY from unity could have been enhanced by reabsorption in the sphere. The observed QYs for the blends are greater than what may be predicted from the absorbances and PLQYs of the individual components, assuming only radiative transfer. By deconvoluting the spectra of the blend, discussed in detail in the

supplementary information, we delve deeper into why this may be.

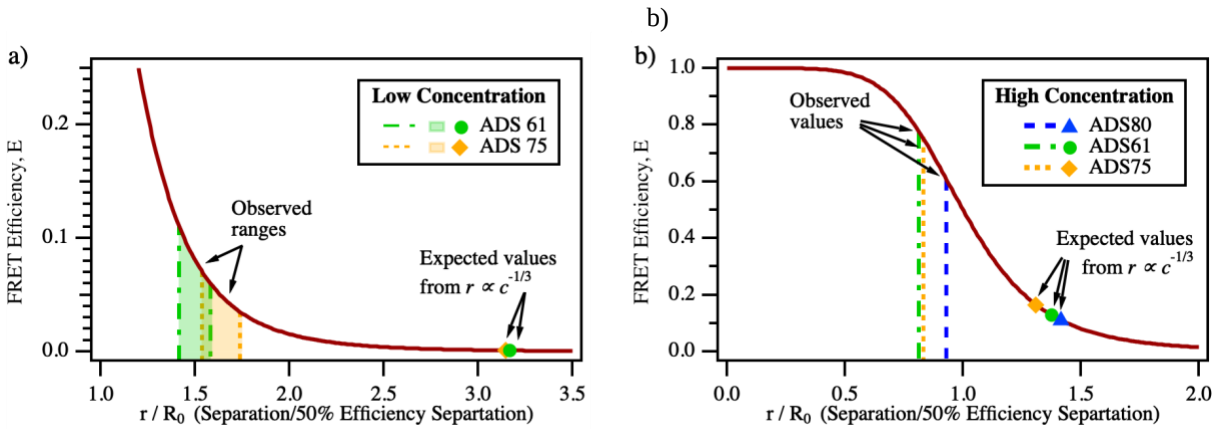

Figure 33: FRET Efficiency as a function of particle separation, observed and expected values

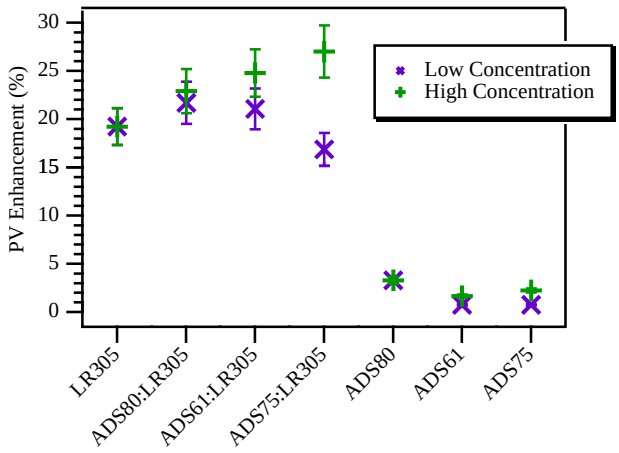

Figure 34: Predicted enhancement to PV from each dye blend

Conclusion

We've provided an in depth look at three UV-absorbing fluorophores with a range of emissions across the visible spectrum, with a focus on their application in power generating greenhouses. First reports of quantum yield in PMMA are given for each, along with the absorbance and emission spectra. Multi-dye systems of these dyes in combination with Lumogen F Red 305 were characterized to understand how the dyes would interact, what kind of efficiencies we could find from these blends, and how they would perform in application. Samples were characterized at low and high concentrations, in which observations of radiative energy transfer and FRET were observed and aggregation in samples was deduced. This aggregation proved beneficial, enhancing transfer efficiencies and the yields from each blend.

At low concentration, ADS80 outperforms the other two dyes both alone and when blended with LR305. The 100% PLQY and high absorption coefficient contribute to high performance in enhancement and net yield, with limited loss from radiative energy transfer, which can be clearly observed in luminescence spectra. At high concentration, though ADS80 maintains a high level of performance, the role of FRET becomes evident and the enhancements from FRET, aggregation, and high absorption make ADS75 the best candidate for enhancing power generation in LSCs. In addition, ADS80 improves the spectral yield for agricultural applications by the restoration of blue light makes ADS80, making it the most interesting candidate for incorporation into existing LSC modules.

To understand in more detail the effects of aggregation in these systems, further studies at the molecular level will need to be explored. However, we have gained a good understanding of how the incorporation of these dyes may enhance the performance of our existing LSC module, making it a more competitive choice in future building integrated photovoltaic applications.

Computational Modeling

To better understand the way in which energy transfer happens in LSC polymer matrices, a computer code was developed to simulate the net result of many thousands of individual fluorophores interacting. Forster's original theory provides a direct way of determining the efficiency of dipole-dipole energy transfer between a single donor/acceptor pair. This single pair is separated by some distance r, has some difference in orientation represented by κ, and is assumed to only interact with its nearest neighbor. All of this goes out the window when we are describing a macroscopic system with Avogadro's number of particles of each dye species.

With such a complex system, it is best to turn to computational approaches. A python code was written to explore how spacing of dye species within a polymer could predict, and affect, FRET Efficiency. Randomly positioned points do not fall into any type of repeating structure where one could easily point to a spacing distance. While the previous "expected" values were calculated using a separation distance which would be realized if all particles were positioned in a perfect cubic

lattice, each having 6 nearest neighbors (NN) with the same distance. The reality is far from being this perfect. The plot below summarizes particle NN spacing under different configurational assumptions.

Spatial Configuration *(akin to point group)*	**Formula for NN spacing 'd'** *(C=dye molecules per nm^3)*	**Coefficient**	**Coordination Number**
Simple Cubic	$d = C^{-1/3}$	1	6
Body-centered Cubic	$d = \frac{\sqrt{3}}{\sqrt[3]{4}} C^{-1/3}$	1.09	8
Face-centered Cubic	$d = \frac{\sqrt[3]{4}}{\sqrt{2}} C^{-1/3}$	1.12	12

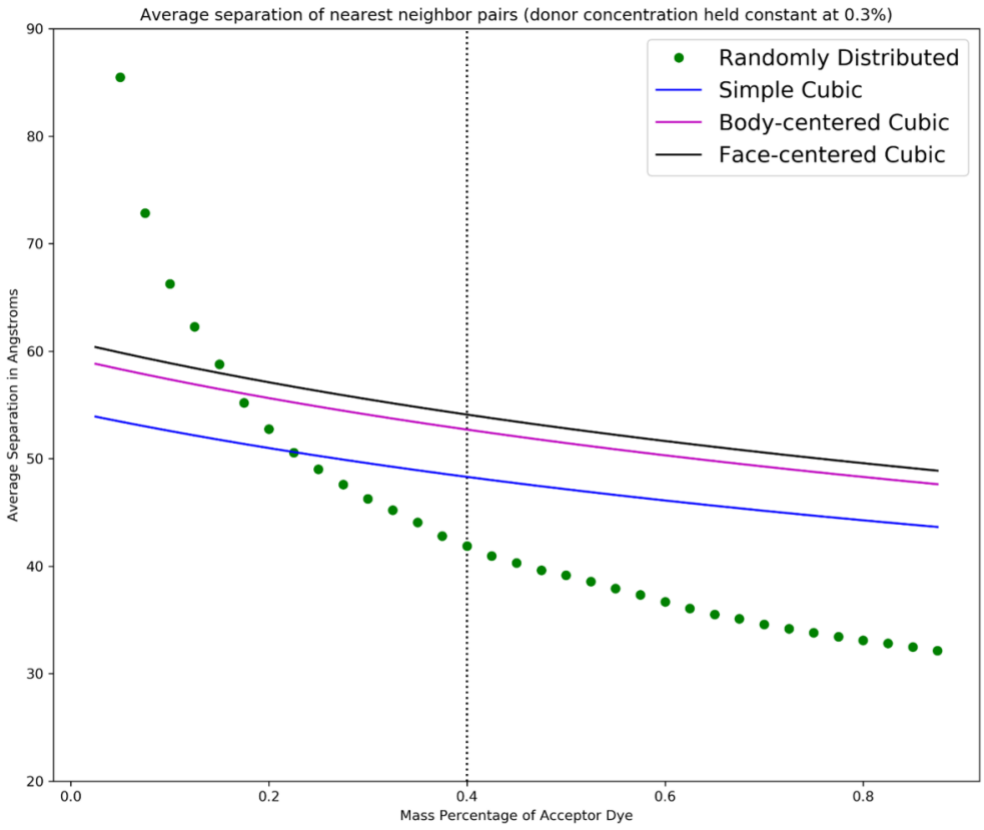

Figure 35: Spacing between nearest neighbor pairs under various spatial configurations

Drawing some inspiration from solid state physics, the plot above compares the random distribution with simple cubic, body-centered cubic, and face-centered cubic spacings. Note that although face-centered cubic lattice structure is known to have the tightest packing structure, it actually does not have the smallest separation distance. This is due to the fact that we are considering a set number of particles in a *fixed volume*, changing the narrative from the stacking problem. As can be seen, at low concentrations, the random distribution leads to much higher average NN spacings. However, as we move to higher concentrations, the average NN spacing goes below that of any of the regularly spaced lattice structures.

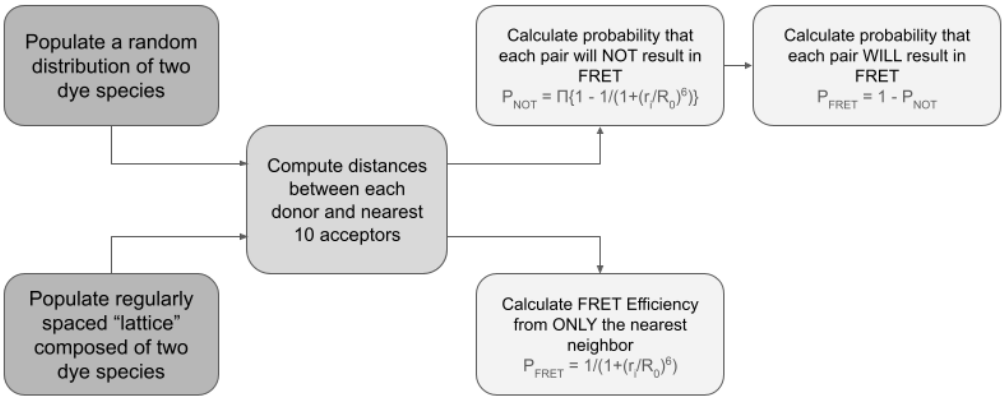

Figure 36: Flow chart for FRET Efficiency Simulation Code

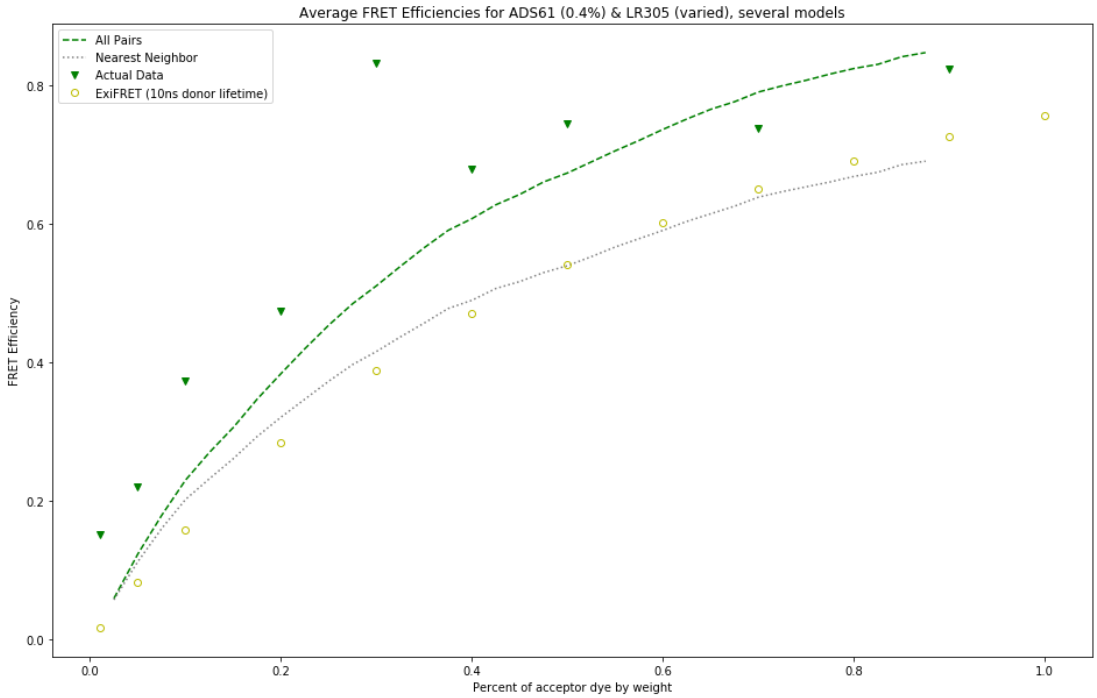

Figure 37: Observed FRET Efficiency compared to various models for ADS 61

'Exifret' is a program created by the Corry Research Group at Australian National University, and was used as a baseline for comparison with the present program.[33] Shown above are the results of simulation to calculate FRET Efficiency for a combination of LR305 and ADS80, keeping the concentration of the former constant, and varying the concentration of the latter from 0.025% to 0.9% by weight (with PMMA). Shown are results from identical parameters in Exifret, the simulation considering either just the nearest neighbor, or the nearest ten neighbors, and the data from the previous section. The nearest neighbor simulation is almost identical to that of Exifret. The minor differences here may be from differences in calculating separation distance (center-center vs edge-edge). Center-center measurements, which the simulation uses, will predict a slightly higher distance which yields a lower

predicted FRET Efficiency, explaining the discrepancy which intensifies at higher acceptor concentrations. Another difference is that Exifret takes fluorescence lifetime into consideration, and will cancel out a FRET event, which would have otherwise occurred, if the acceptor molecule involved is already in an excited state. This will lead to overall lower efficiencies, especially at higher concentrations. Since the discrepancy is actually in the opposite direction of this, the effect is taken to be small enough to be ignored.

For the case of ADS 61, the actual data and the multiple pairs simulation are in fairly close agreement with one another. This would suggest that considering FRET Efficiencies with multiple neighbors is a more accurate way of viewing multiple dye interactions within a large system like an LSC. Since Forster's original theory really only described a single pair of molecules, it's no surprise that it would fall short when considering many molecules, often having several neighbors just fractions of a percent further away than the NN. Furthermore, it is suggested here that simply finding an average value for the NN, and plugging that into *equation 20* is insufficient.

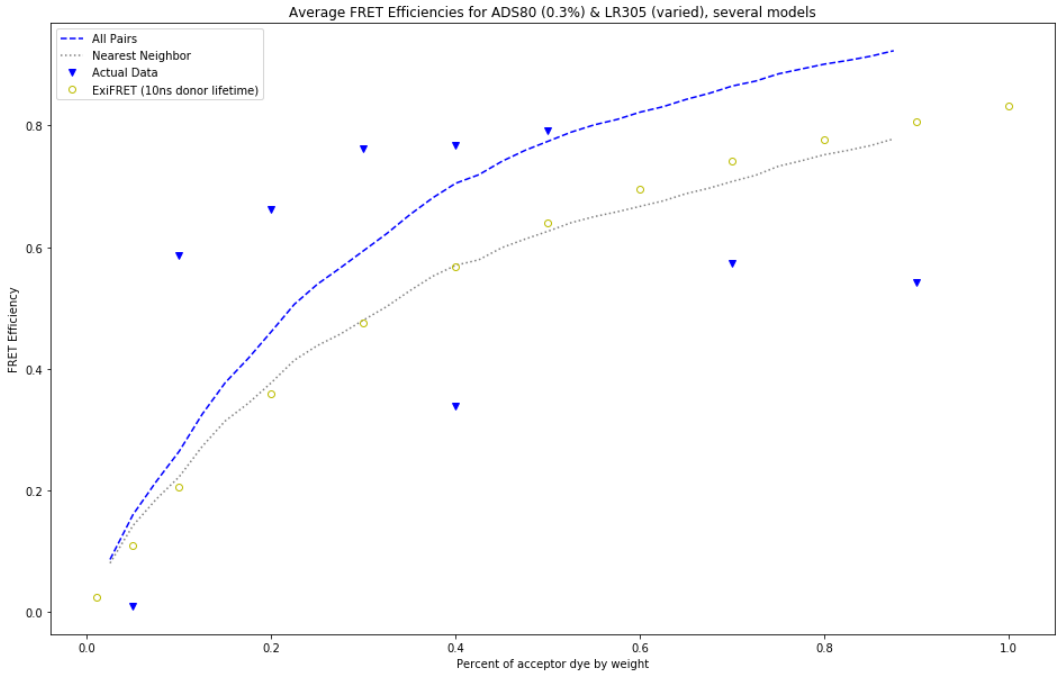

Figure 38: Observed FRET Efficiency compared to various models for ADS 80

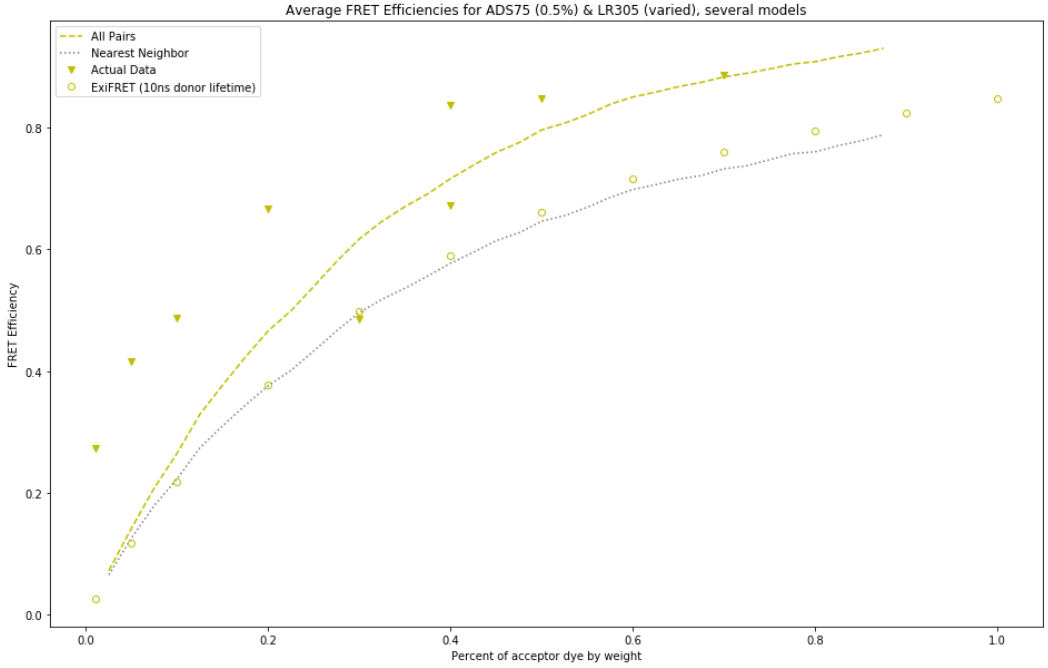

Figure 39: Observed FRET Efficiency compared to various models for ADS 75

The same simulation for the other two dyes reveals a similar, albeit less convincing, relationship between the various methods. In all cases, the measured values for FRET Efficiency start higher than the prediction at low concentrations, and then fall below as it increases. This could point to some systematic experimental error, potentially tied to the integrating sphere and its calibration. However, it may also point to aggregation in the system. If the two dye species are tending to clump together, rather than simply be arranged randomly, that could explain higher FRET at low concentrations. In this case, we might get closer spacings than the simulation would predict.

To ensure the model works as desired, a series of tests were conducted to gain confidence on certain parameters. Shown below are two such tests. The first is to see how many next nearest neighbors is sufficient to consider for an accurate result of the many pairs simulation. The parameter tested, called 'thresh', is tested by iteratively increasing the number of donor-acceptor pairs to calculate E_{FRET} for, within the already generated list of closest particles. From this test, I conclude that 10 NNs is enough for accuracy.

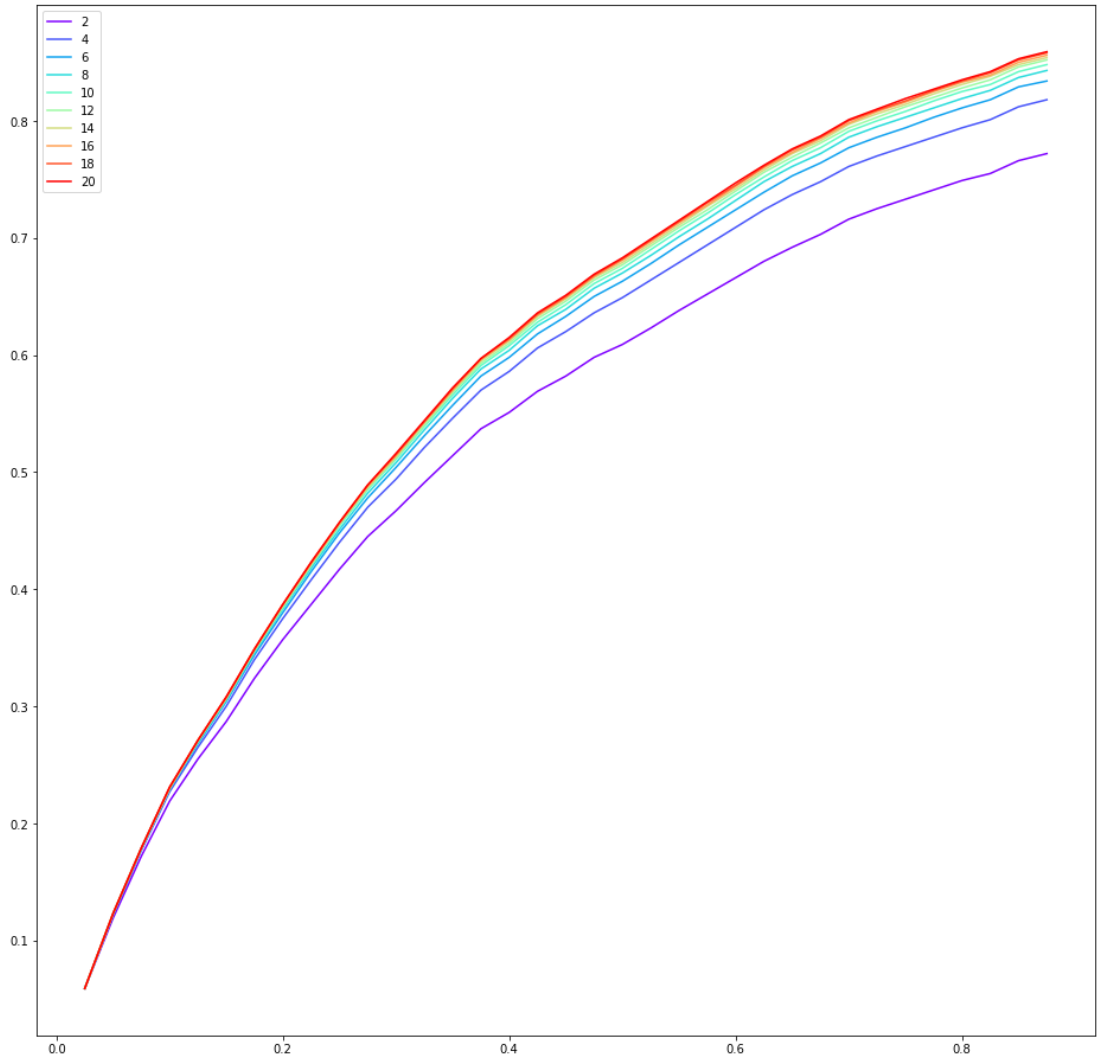

The next test performed is to see the effect of one random seed over another. A computer language such as Python has no way of truly generating a random number, with which to populate a volume with particles. Instead, it yields quasi-random numbers by doing arithmetic on extremely large numbers. The exact conditions which it starts with determine what values it will produce, and these starting conditions are wrapped up in a parameter called a ‘seed’. Each time a program is run with a given seed value, it will produce the exact same “random” numbers. By iteratively populating the volume with particles based on varying

random seeds, I have obtained a range of values which encompass all possible values within the simulation. These ranges are shown for both single and multiple pair simulations as the shaded region between bounds.

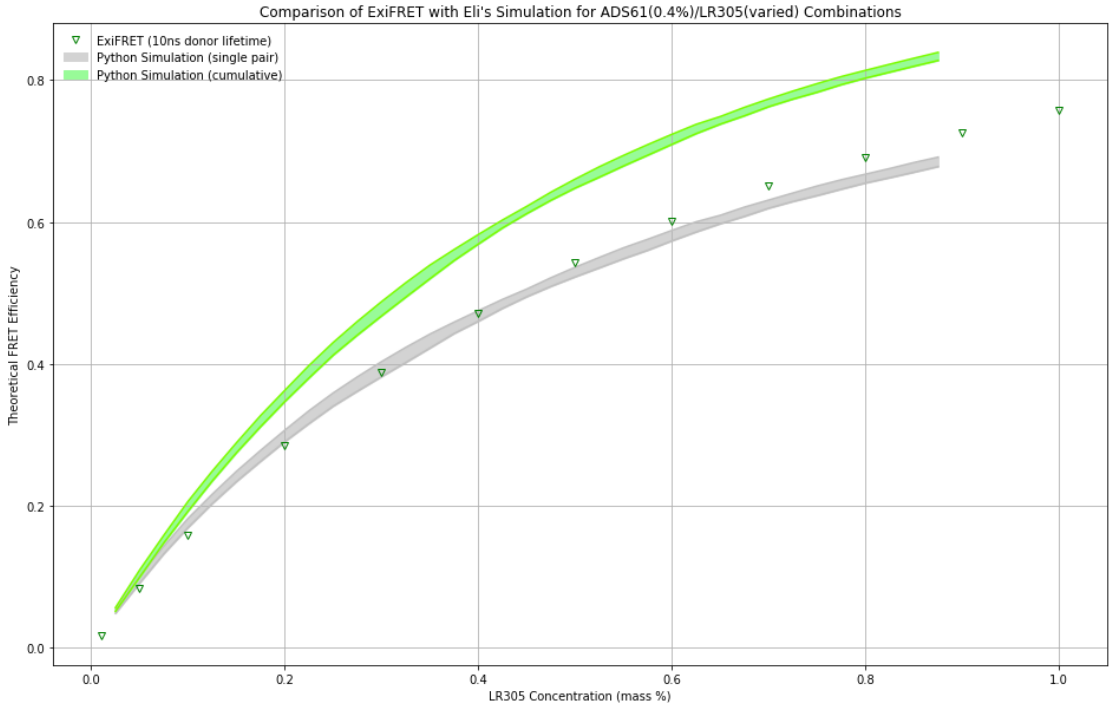

In all cases, the single pair simulation is very close to Exifret. Also in all cases, the multiple pair model fits the data better than either previous simulation. The previous assertion that dye aggregation in our system is leading to higher than predicted FRET Efficiencies is reinforced by the model developed. This helps to solidify the notion that there are J-aggregates present in our system, benefitting the overall quantum yield.

CHAPTER 2: Redox Active Materials for Hydrogen Production

Background

Hydrogen is the simplest element, consisting of (most commonly) just one proton and one electron. Unless locked up in other molecular bonds, pairs of hydrogen atoms will spontaneously form covalent bonds becoming H_2 gas. It is, of course, quite combustible! In fact, that is the whole point of trying to use it as a fuel. In the presence of oxygen and heat, water vapor will be formed, along with excess energy in an exothermic reaction. No hydrogen gas is present in Earth's atmosphere due its extremely low density compared to the other gases which make up air, therefore any hydrogen fuel we use must be synthesized from other molecules containing the element.

Redox Reactions for Solid State Applications

Before discussing the methods commonly used for generating hydrogen, let us describe the chemical processes of reduction and oxidation. These terms are often misunderstood, in part because the words themselves seem to imply something else entirely. Throughout human history, we have noticed the effects of oxidation in pigments or food items, without really understanding the root cause. As it turns out,

oxygen in the air is fairly reactive, and will tend to remove electrons from neighboring atoms within molecules. While oxygen is the *oxidizing agent* we might most frequently encounter, other molecules (diatomic chlorine gas for example) can be strong oxidizing agents as well. When an atom has had an electron removed from its valence shell, it is said to have been *oxidized*.

Whenever one atom is oxidized, another must have been reduced because the number of electrons cannot change. An atom is said to have been reduced when it *gains* an electron. This terminology seems to be a holdover from the unfortunate decision to call the charge of an electron negative; by gaining an electron, the charge on that atom "decreases" and it thus reduced. Any atom, either by itself or residing within a molecule, has a property known as an *oxidation state*. This is simply the value of localized charge immediately surrounding that atom (in terms of the elementary charge unit e). A lone atom of sodium, for example, exists in an oxidation state of zero, because it has a neutral charge. Likewise, metallic sodium is also at zero, because all of the sodium atoms are sharing electrons equally, with none of them gathering around one site more than another. However, in table salt, sodium exists in an oxidation state of +1, while the bonded chlorine atom exists at -1. In this case, the two elements are locked in an ionic bond and we can think of Cl as 'stealing' the electron away from Na.

Elements within the first two, and last few columns of the periodic table, tend to have exactly one oxidation state they can exist in while molecularly bonded.

Potassium, for example, has one valence electron. To form a stable configuration, it will give up that one electron and, in turn, be left with a full set of eight electrons in its valence shell. This thinking works for simple elements which utilize s and p orbitals only. However, once we get into elements which contain d orbital electrons, these simple rules no longer apply.[34] The transition metals in particular often may exist in several different oxidation states, depending on their nearest neighbors, or formation parameters like temperature.

The wide range of observable oxidation states in this region is largely a result of the complex nature of the d orbital. Following from the Schrödinger equation applied to the atom, the d orbital (having angular momentum number, ℓ=2) has a $2\ell + 1 = 5$ spatial states, with two electronic spin states in each, resulting in 10 total electronic states. Though higher in angular momentum, these d orbitals are lower in energy than the atom's highest s orbital electrons. The highest oxidation state which can be realized by an element in this section is given by its 'group number', or the roman numeral above each column followed by the letter B. Atoms tend to lose their highest energy electrons first, in this case belonging to the s orbital. The configuration of the resulting d orbital configuration after ionization has much to do with its stability. Having no electrons left in the d orbital (d0) is quite stable. In this case, the first two electrons to leave are generally the two (highest energy) s orbitals. After that, shedding all d orbital electrons achieves a full energy shell, just as would be the case with Ca^{2+} for example. As we move to the right within a row, however, more and more electrons have to be removed to achieve this. Usually, after about halfway

through each row, it would require too much energy to ionize an element to a d0 state. Having 5 filled d orbital states (d5) is also very stable, since each spatial state is generally filled first before pairing electrons of opposing spin.

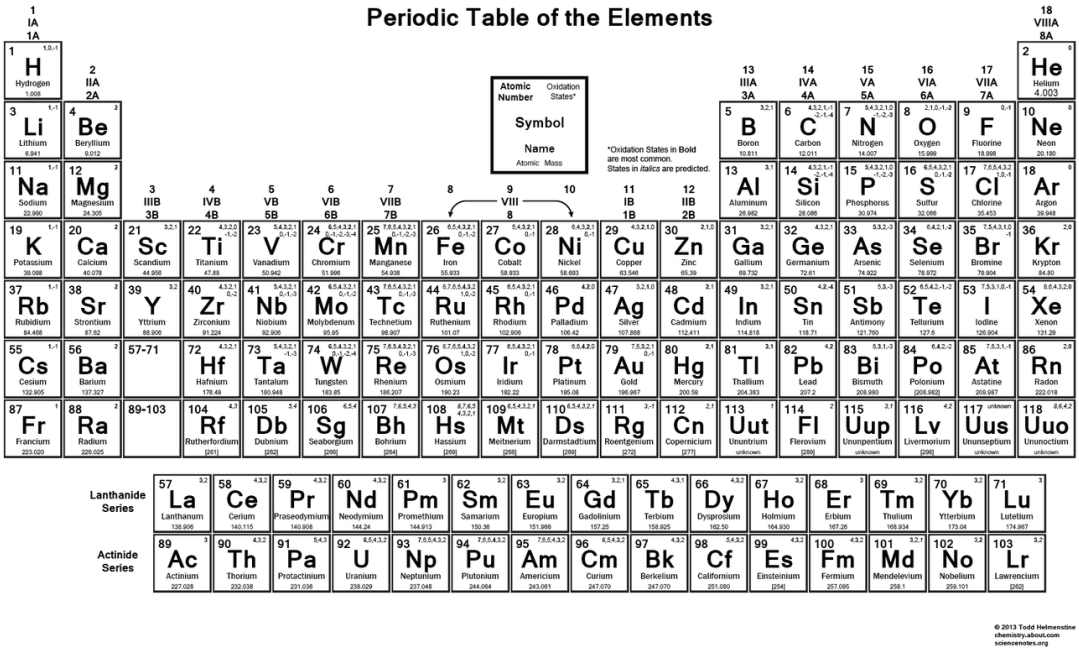

Figure 40: Periodic Table of the Elements, illustrating electron valency and oxidation states

Cations falling in between these two conditions exist, but tend to be less stable. Important to the current work is the example of Manganese. Mn2+ results in a d5 configuration, yet Mn3+ and Mn4+ both exist abundantly in nature. Depending on factors such as the coordination number in its lattice, the latter oxidation states tend to readily become reduced, moving toward the more stable 2+ state. This makes them oxidizing agents, since by gaining an electron themselves, they are taking an electron away from a neighboring atom. Other d orbital configurations are stable for various reasons, but will not be important in the present work.

Common Generation Methods

Fossil Fuel Driven Reaction

The vast majority of industrial hydrogen (~95%) is produced from fossil fuels, most notably by a process called steam-methane reforming.[35] First, a methane source such as natural gas is needed. A pressure tank is filled with methane, whereby high temperature steam is introduced. This steam can be as hot as 700-1000c, and tank pressures from 3-25 bar. The methane reacts with steam to form hydrogen. This initial reaction does not actually produce any carbon dioxide, however, generating the heat required to drive the reaction contributes a considerable portion of the embodied carbon for the entire process. This reaction does, however, produce carbon monoxide.

$$CH_4 + H_2O \xrightarrow{heat} CO + 3H_2 \quad (24)$$

Since it's not very desirable to have a bunch of carbon monoxide lingering as a result of the process, one further step is taken. Carbon monoxide is reacted with water to form carbon dioxide and more hydrogen gas.

$$CO + H_2O \leftrightarrow CO_2 + H_2 \quad (25)$$

This is known as the water-gas shift reaction, and is of great importance to many industrial processes. This reaction can run in either direction and has a

crossover temperature of about 700c, which is the point at which the change in entropy equals the change in enthalpy.

At the end of the day, only one CO_2 is formed for every 4 H_2 molecules formed, which is not too bad. Even still, the amount of energy input makes this a major contributor to global carbon emissions. Similar reactions can take place if other fuels like coal or ethanol are used in place of natural gas, although various byproducts can be formed depending on the purity of the sources.

Electrolysis/ Water Splitting

Perhaps the most popular way to produce hydrogen gas without any input of fossil fuels (or other carbon based fuel) is electrolysis, or the splitting of water by way of a maintained voltage differential. Above a certain threshold voltage (around 1.1v for slightly ionic water) H_2O molecules can dissociate into OH- (hydroxide) ions and H+ ions (which actually tend to closely associate with another water molecule to act as H_3O+). Once split, these ions become charge carriers which conduct a current between the two electrodes. Essentially, instead of another molecule, the anode is the oxidizing agent, and the cathode is the reducing agent. As H+ ions migrate toward the negatively charged cathode, electrons are 'donated' to them in order to form hydrogen gas in the following reaction.

$$4H^+ + 4e^- \rightarrow 2H_2 \qquad (26)$$

Consequently, hydroxide ions formed at the anode contribute electrons which carry the current in the overall anode reaction:

$$2H_2O \rightarrow 4H^+ + 4e^- + O_2 \quad (27)$$

Solar Thermochemical Hydrogen Production

Abbreviated as STCH (pronounced "stitch"), this process also takes its hydrogen from the water molecule, but takes a much different approach than the previous two methods. Unlike steam reforming, there is no fuel consumed, and water is the only material input. And, unlike electrolysis, the energy input is purely in the form of heat instead of electricity. This has potential ramifications for the overall efficiency of the process, which will be discussed later. The basis of operation for STCH is the cyclical formation and destruction of oxygen vacancies in an oxide material. Most transition metals can form multiple varieties of oxides, based on the oxidation state they assume. Iron oxides are a prime example; hematite is a naturally occurring form of iron(III) oxide with formula Fe_2O_3, while magnetite (also naturally occurring) has a formula of $Fe^{2+}Fe_2^{3+}O_4$ and exhibits mixed oxidation states within its unit cell. The possibility to change oxidation states depending on environmental conditions makes it possible to use certain oxides to strip an oxygen atom from a water molecule to produce diatomic hydrogen gas.

$$H_2O(steam) + V_o \leftrightarrow H_2(gas) + O_o + Heat \quad (28)$$

...where V_o is a vacancy at an oxygen site, and O_o is the occupancy of an oxygen site. This is a reversible process, and will proceed to the left or right depending largely on the partial pressure of oxygen (or equivalent) within the reaction chamber. Not all materials can tolerate oxygen vacancies, especially as they are cyclically formed and then filled. To be considered a good STCH candidate, a material must exhibit this, and possess the ability to undergo this reaction within a workable temperature range.

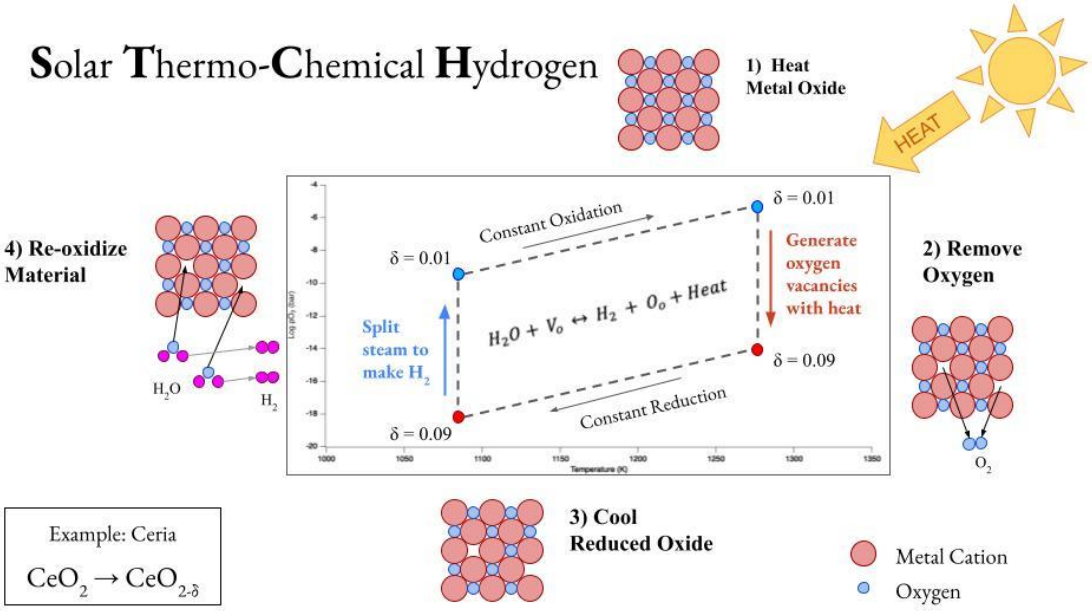

Figure 41: Redox cycle diagram for STCH

It is the forward reaction which produces the hydrogen, and it proceeds spontaneously (provided there is sufficiently high pO2e) because the crystal formation of oxides is much more stable when all sites are occupied. This manifests as a large negative enthalpy value for the O_o term, driving the reaction to the right. In order to reverse the process and create a vacancy, heat must be put into the system.

For STCH, this heat comes from concentrated solar light, which does not interact with any photovoltaics, but rather just heats up the reaction chamber to drive the reduction of the crystal. In this way, the cycle is broken up into two parts: the crystal oxidation stage in which water is split, and the crystal reduction stage in which the vacancy sites are replenished, allowing for the next round of water splitting.

In the oxidation stage, water in the form of steam is introduced into the reaction chamber and the equivalent pO2 of the steam drives the reaction forward. However, a high pO2 is not enough to fully react the material on its own. The surface of the crystalline material will tend to completely react, while the bulk remains largely unreacted. To overcome this, temperatures must remain fairly high even during this step, in order to increase the gas diffusion rate of the solid.

$$\frac{\partial c}{\partial t} = D * \nabla^2 c \tag{29}$$

This is the generalized form of the diffusion equation, containing the Laplacian operator. Here, ‘c’ is the concentration of some ion or vacancy, and is in general a function of both position and time. It is apparent that a higher diffusion constant (D) will lead to a higher ion flux ($\frac{\partial c}{\partial t}$). This partial differential equation can actualize in many forms, depending on the geometry of the particles involved, and boundary conditions. In the simplest 1-d case, if we imagined a rod with its center filled with vacancies and left to find equilibrium, equation 30 solves to become a series of gaussian peaks which broaden over time until the whole rod is evenly filled

with vacancies. In our case, the situation is more like a sphere with uniform vacancies which are being filled from the outside in. Whenever the reaction has gotten satisfactorily close to completion, we can call this our cycling time. It is, of course, of economic importance to make this as fast as possible.

In the reducing stage, the temperature is raised further, and pO2 is kept as low as possible. Nitrogen gas is commonly used for this due to its abundance and low cost. As the reduction reaction proceeds, oxygen gas is evolved into the chamber, which must be evacuated throughout the process. Depending on the redox material used, the reduction temperature may need to be as high as 1200-1400c in order to achieve high enough rates to make the process economically viable. A mirror field solar concentrator can easily achieve temperatures as high as this. The challenge becomes keeping the needed temperature low enough that a reaction chamber can be made which will not melt! Quartz has a melting temp of 1650c, but has a glass transition temperature around 1200c, limiting its range for STCH. Most materials with higher critical temperatures are cost prohibitive. Thus, the search for STCH materials is driven largely by having a low reduction temperature.

The benchmark material for STCH is ceria (CeO2). In its pristine form, ceria contains a cerium atom in a 4+ oxidation state. Cerium is much more stable in this form, but may also exist in a 3+ state. Ceria which has been reduced to have oxygen vacancies, will readily strip oxygen from water at high rates, due to enthalpic

favorability. However, due to the high stability of the 4+ state, it requires temperatures of over 1400c to viably reduce.

Industrial Need

Like other fuels, hydrogen can be used to drive any number of processes which convert stored energy to usable forms. I'll break this down into three categories; electricity generation, transportation, and industrial feedstock.

The vast majority of electricity on the planet is generated by using a fuel source to heat water, which consequently drives turbines as steam to move electrons. In principle, hydrogen gas is capable of performing this exact same function, replacing traditional fuels like coal or natural gas. The main benefit, of course, is that burning hydrogen produces only water vapor (but still some NO_x compounds), unlike the latter two which also produce carbon dioxide (along with a slew of other unwanted organic compounds). Energy conversion by way of fuel cells can avoid unwanted emissions, and obtain higher efficiencies (cite highest) due to the reduced energy loss through heat. The main downside to fuel cells is the necessity for expensive catalysts like Platinum to operate viably. Many researchers are looking for new, lower cost catalysts for this and other related processes. Fuel cells are also the primary option for utilizing hydrogen in vehicles. For these two categories, incorporating hydrogen would be a new approach, which leads to a handful of logistical issues. For one, hydrogen gas on its own is highly reducing, and will degrade many common metals which are currently used to store conventional fuels.

For high pressure hydrogen storage, specialized tanks are needed which often employ carbon fiber hulls with a different material lining the inside. Because of this and its small physical size, hydrogen is also more prone to leaking, which is a recipe for disaster, especially inside a personal vehicle. Alternative methods for storing hydrogen often involve performing a second reaction to "store" the hydrogen in a different chemical. Ammonia and methane are both candidates for this, but are beyond the scope of this paper.

Another important use for hydrogen is in industrial feedstock. An important example of this is the formation of ammonia for use in synthetic fertilizer. The EIA has stated that without synthetic fertilizer, sadly could not maintain enough crops to support the earth's population at our current food consumption rates. Until 1909, only a handful of microorganisms were capable of converting atmospheric diatomic nitrogen into compounds usable by plants, in a process called nitrogen fixation. We eventually learned that we could convert N2 ourselves, by pumping in heat at high pressure in what is called the Haber-Bosch process. Today, this process accounts for over 1% of human carbon emissions, partly due to the need for hydrogen gas to complete the reaction. If green hydrogen were used in place of fossil fuel derived hydrogen, we could cut this down by a large margin.

The steel industry is another area which has considered expanding the use of hydrogen in its processing. Converting from iron oxides into metallic iron requires the use of strong reducing agents. Hydrogen fits the bill, and is used in the steel

industry today in conjunction with carbon monoxide. However, these are produced by reforming natural gas, which produces both of these products in the same reaction, but also consumes a lot of energy with a high carbon footprint. It is being explored to use hydrogen as the only reducing agent in steel formation.[36] This would cause big decreases in carbon emissions of the industry if the hydrogen were sourced from renewable means

Multiple and Nonlocal Cation Redox in Ca-Ce-Ti-Mn Oxide Perovskites for STCH Applications

Theoretical work carried out by Ellen Stechel's team at ASU had identified $Ca_{2/3}Ce_{1/3}Ti_{1/3}Mn_{2/3}O_3$, hereby referred to as CCTM2112, as a potential material for STCH. Specifically, they hypothesized that redox could occur on both A and B sites of this material, which could have positive impact on its water splitting capabilities. A close analog of CCTM2112 was synthesized, with an exact stoichiometry of $Ca_{0.65}Ce_{0.35}Ti_{0.3}Mn_{0.7}O_3$, and tested for STCH activity.

Stagnation Flow Reactor Experiment

To simulate the conditions of a working STCH reactor, the stagnation flow reactor (SFR) was created. A laser is used to heat the reaction chamber, and user specified gases are able to flow at known rates for either oxidation or reduction steps. A coupled mass spectrometer is used to determine accurate quantities of each redox

step product, either oxygen or hydrogen, as a function of time. When integrated over one half cycle, a figure of merit can be obtained which indicates how much hydrogen is produced per cycle, per mole of oxide. This figure partially demonstrates how economically viable the STCH material is. Another key aspect is the amount of time it takes to adequately reduce the material and subsequently reoxidize it. Putting these together, we can see the full utility of the material as being how much hydrogen is produced per mole of oxide per day. Below is a plot tracking how much product is generated over the course of a few cycles.

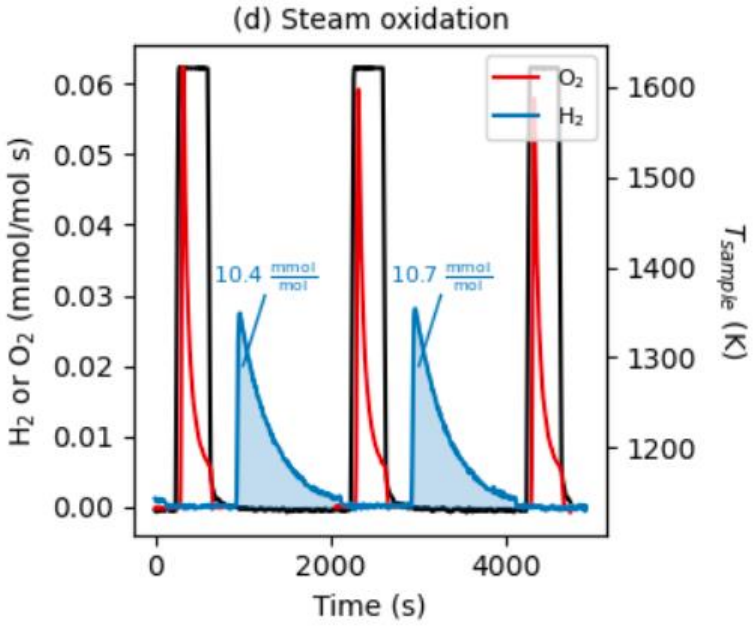

Figure 42: Stagnation Flow Reactor cycling data for water splitting

By standardizing the conditions, including time spent in each half step, we can compare many different potential STCH materials. CCTM2112 shows immense

promise as it has been observed to produce significantly higher amounts of hydrogen, per mole of oxide, than other leading materials.

Table 7: Comparison of state of the art STCH oxide material performance

Metal Oxide	**Conditions**	**µmol H_2 per gram Oxide**	**mmol H_2 per mole Oxide**	**Reference**
$BaCe_{0.25}Mn_{0.75}O_3$	*	140	7.3	[37]
$Sr_{0.6}La_{0.4}Mn_{0.6}Al_{0.4}O_3$	*	194	8.2	[37]
CeO_2	*	50	2.9	[37]
CeO_2	Tred = 1800 K, pO2 = 1×10-4 bar	~170	~10	[38]
$Ca_{0.65}Ce_{0.35}Ti_{0.3}Mn_{0.7}O_3$	*	298.8	10.4	This Work

*Tred = 1623.15 K (330 s), Tox = 1123.15 K (1200 s), and 40 vol% H2O

Magnetic Moment Measurements

A transition element which undergoes a redox reaction, gaining or losing an electron, may experience a change in magnetic moment. Every electron has a quantum spin number of ½, and these can be said to exist in a spin up or spin down orientation. If a certain state of an atom has a net spin up, say, when all electrons are accounted for, it will exhibit a magnetic moment. If this atom loses electrons during a reaction, it might lose those high energy d orbital electrons which tend to align with the same spin orientation, thereby decreasing its moment. Many different possibilities exist here, but measuring µ can reveal a lot about specific oxidation states within a

material. Shown below is a summary of such a series of measurements conducted on CCTM.

Table 8: Magnetic moment measurements of CCTM elements during redox

Element	Mean ± σ	Minimum	Maximum
Ca	0.00 ± 0.00 (Ca^{2+})	0.00 (Ca^{2+})	0.00 (Ca^{2+})
Ce	0.28 ± 0.23 (Ce^{4+})	0.06 (Ce^{4+})	0.68 (Ce^{3+})
Ti	0.05 ± 0.02 (Ti^{4+})	0.03 (Ti^{4+})	0.08 (Ti^{4+})
Mn	3.77 ± 0.24 (Mn^{3+})	3.10 (Mn^{4+})	4.50 (Mn^{2+})
O	0.01 ± 0.01 (O^{2-})	0.00 (O^{2-})	0.05 (O^{2-})

Quaternary Oxide Perovskite Study for STCH Performance

Material Selection Criteria

To temper the voracious oxidation potential of cerium III, other elements with the opposite effect can be introduced into the material. Manganese is an element of interest here, because it may exhibit a wide range of oxidation states, most commonly 2+,3+,and 4+. Mn 4+, and to a lesser extent 3+, are strong oxidizing agents. This means that they oxidize something nearby, which in turn makes the Mn species itself become reduced. This complements the highly reducing Ce3+, which readily oxidizes to split water. With this in mind, theoretical work led by Ellen Stichel's group at ASU to identify a structure which incorporates both cerium and manganese was underway.

One promising structure they identified is the perovskite (Ca,Ce)MnO3, where Ca and Ce copopulate the 'A' site, Mn occupies the 'B' site, and oxygen is the anion. In this configuration, both elements can be associated with a single oxygen atom, moderating the enthalpy of formation of a vacancy at that site. However, this phase is not stable as shown by in operando XRD measurements, which showed CaMnO3 with most or all cerium caught up in the CeO2 phase. The introduction of titanium at the 'B' site was shown to stabilize the structure, and gives us our material of interest.[39]

$$(Ca_{1-x}, Ce_x)(Ti_{1-y}, Mn_y)O_3 \tag{30}$$

Here, x and y are numbers between 0 and 1. We can think of each cation site of this perovskite as existing in *solid solution*. A solid solution is when a crystalline material can have a site of a unit cell occupied by two or more different elements with a random distribution. This is distinguished from a system such as an intermetallic mixture, in which there are regularly placed elements at particular lattice points. Effectively, we can think of CCTM as a structure with the lattice properties of $CaTiO_3$, but each cation site may be randomly populated with any of the cations in the mix. Additionally, the fact that both sites have potentially redox active elements has been hypothesized to have an important, beneficial effect for STCH. When oxygen would leave the crystal structure, it could "choose" to reduce one of its neighbors over the other. Because there are two species neighboring one oxygen, there are more available states and thus a higher entropy.

Solid State Synthesis Reactions

We most often think of chemical reactions which take place in the presence of some kind of solvent. Baking soda is added to vinegar (acetic acid diluted in water) to form sodium acetate, water, and the telltale carbon dioxide which causes the volcanic eruption. However, compounds do not always need a solvent as a means of delivery. Many geological mineral formation events are examples of this. For example, when titanium-rich pockets within the Earth are subjected to sufficient heat and pressure in low silica regions, they may react with ubiquitous calcium and oxygen to form Perovskite ($CaTiO_3$)[40], the namesake of the class of semiconductors so widely studied today. This mineral, also known as Calcium Titanate, forms the basis of the material under investigation in the current work to split water and form hydrogen gas.

Synthesis in a laboratory setting allows for the fine tuning of formation parameters such as pressure and temperature. The lack of solvents in the process makes for a simpler and cleaner synthesis. Long exposure to a high temperature allows for fewer defects when compared to a rapid solvent based process like [example]. Ions are able to migrate to their lowest configurational energy state in this way, leading to a high purity product. The following is adapted from my manuscript written on the study regarding synthesis.

Precursor stoichiometric ratios were selected based on theoretical work performed by [Ellen Stichel's group], and were narrowed down to a group of six to be tested. All precursors were stored in a dehydration box, maintaining a humidity of no

more than [4%]. MnO2 powder (Alfa Aesar, 99.9%) was dehydrated prior to any further processing. CaO (), Ce2(CO3)3 (), Mn2O3 (), and TiO2 () were ground in an agate mortar and pestle prior to weighing. Ground precursor powders were passed through a sieve, and the portion under 75 um was used. Stoichiometric amounts of each precursor were weighed out and added to a [40mL?] glass vial, before stirring to mix with a scoopula. The mixed powders were then added back to a clean mortar and pestle to be ground once again all together to ensure the most homogeneous mixture possible before adding contents back into vial.

Approximately 4 grams of powder mixtures were added to a 1" circular stainless steel die and gently tamped first, to achieve even distribution. To ensure high particle interaction and minimal air pockets, dies were then hydraulically pressed at ambient temperature, high vacuum (approximately 10-9 bar), and maximum uniaxial pressure of 149 MPa (21,700 psi) resulting in a maximum force of 75.6 kN (17,000 lb). The details of this pressing procedure can be found in the SI. The resulting pellets were then transported to a CM tube furnace with alumina tube, placed in an alumina "boat" lined with platinum foil, and [annealed?] at 950C primarily to evolve out any carbonates as carbon dioxide. Pellet masses were recorded before and after to ensure completion of this process.

The resulting pellet was then ground once again in a mortar and pestle, packed into the same die, and vacuum pressed with the same procedure as before. Resulting pellets were then [annealed?] for a second time, now reaching a maximum

temperature of 1500C, and holding this for 20 hours to allow for a full solid state reaction to occur. These much harder pellets were then forcefully ground into a fine powder to be further studied.

Redox Cycling

To simulate the alternating oxidizing and reducing conditions that a STCH material must undergo, the following steps were taken to use the CM furnace for this purpose. Three alumina boats, lined with Pt foil and containing two pellets each, were placed on a custom-made, castable alumina "sled" which was then slid to the exact center of the tube to ensure that all samples experienced the exact same cycling conditions. Next, a pair of alumina baffles (made by the same casting process) were placed at either end of the furnace tube to prevent component damage and sample contamination. End caps with gas flow ports were fitted onto each end of the furnace tube. For reducing conditions, pure nitrogen gas was flowed through the tube at and the furnace was ramped up to a temperature of 1200C, which was held for 16 hours before ramping back down. Oxidizing conditions were achieved by the same temperature ramping schedule, but flowing compressed air (21% Oxygen) instead of N2.

Three full redox cycles (one reduction, followed by one reoxidation) were conducted sequentially and with minimal interruption. At the beginning and after every half cycle (7 total), aliquots in the 100 ug range were taken and stored for

further analysis. Masses of each powder sample were also recorded (before and after removing aliquot) at the end of each half cycle in an attempt to directly measure changes in oxygen vacancies arising from redox cycling. The details of this procedure can be found in the SI. After three full cycles, the samples were subjected to one final reduction step, but for 84 hours at 1200C this time, resulting in what is being called our “deep reduced” samples.

It is imperative that each sample experiences identical temperature conditions during the cycling to compare their redox behavior to one another. After undergoing one cycle, it was noticed that the samples placed in the middle region of the CM furnace were much more reacted than any placed on the outside. Furnaces like this claim to be uniform in temperature within a region extending beyond where the samples were placed, but this needed to be verified. To investigate this, a [type k?] thermocouple with fused silica rod measuring ~20” long was used to profile the tube furnace. Two temperatures were tested, 1000 and 1100 C. After the furnace had reached the desired set point, the thermocouple was slid along a custom aluminum shelf, made just for this purpose, into the center of the tube from the outside, progressing the tip at one inch increments. At each increment, the thermocouple was left until the measured temperature stabilized (~15s) and then recorded.

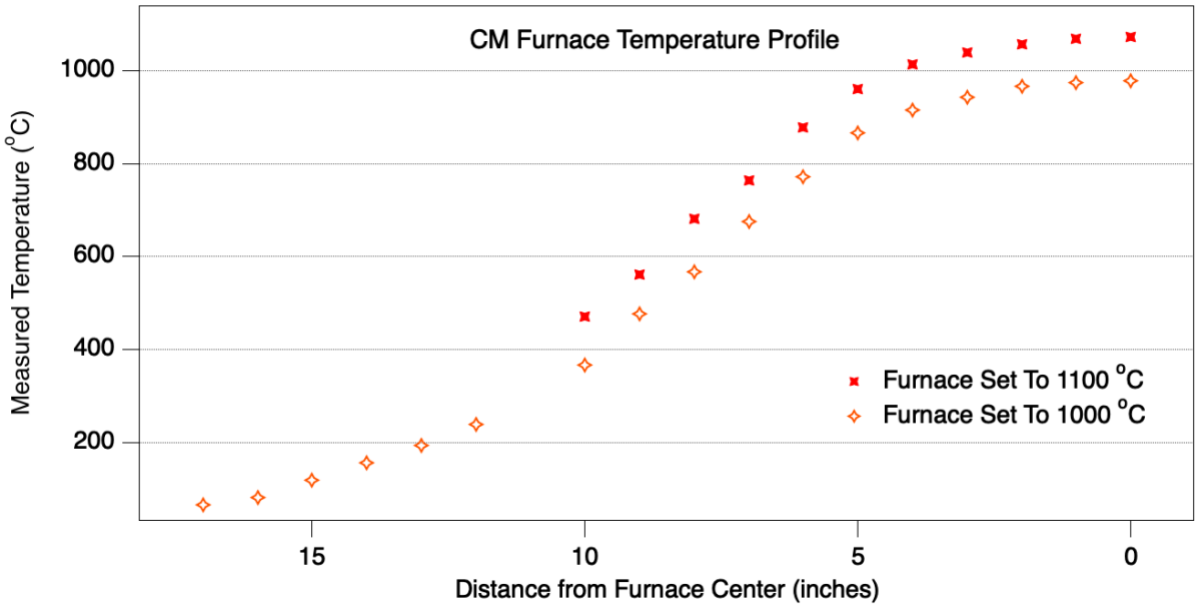

Figure 43: Tube furnace temperature profile illustrating inconsistencies

The results of this furnace profile indicated that there was a substantial difference in temperature experienced by each alumina boat containing samples during redox cycling. To address this, a custom "sled" was made using a castable refractory alumina. This allowed all 6 samples to be placed in the exact center of the tube, which otherwise would be impossible due to the curved interior surface.

Characterization Methods

Thermogravimetric Analysis (TGA)

For samples which undergo a change in mass with environmental changes, TGA is an important tool for characterization. Examples of this are water adsorption on a material surface increasing its mass, or loss of mass due to carbonate groups

evolving out of a material into carbon dioxide as heat is applied. Measurements allow the researcher to observe how quickly, and in which temperature regimes, chemical reactions take place. In the current research, TGA has been used to analyze the reduction and oxidation of CCTM as it loses and gains oxygen molecules from its surrounding atmosphere. Let's take a look at how a TGA machine works, and preliminary results of redox cycling CCTM.

Inside of a TGA are two thin lever arms made of [alumina?], about 20 cm long, with small (~5mm) cups on the near ends. These lever arms attach on the far end to sensitive force meters, and are used to measure sample mass with high resolution. The arms sit inside a retractable tube made of [], which makes an airtight seal when closed. This allows for user specified gas or combination of gases to be flowed through the chamber, past the samples, during operation. The tube also serves as a furnace, allowing for internal temperatures of up to 1300c. A metal pan is placed in each lever arm cup, one of which contains the sample. The type of metal is determined by the desired operating conditions. High temperatures or reactive samples warrant the use of a platinum pan. Platinum has a high melting temperature (1700c), and resists chemical reactions, but it is quite expensive due to its relative scarcity and high industrial need. Therefore, when possible, an aluminum pan should be used.

The reason for having two pans is to account for any changes incurred by the pan itself during operation. Otherwise, any water adsorption or pan oxidation would

errantly show up as a change in mass of the sample, compromising the data. To this end, the mass data registered is always that of the sample arm subtracted by the reference arm.

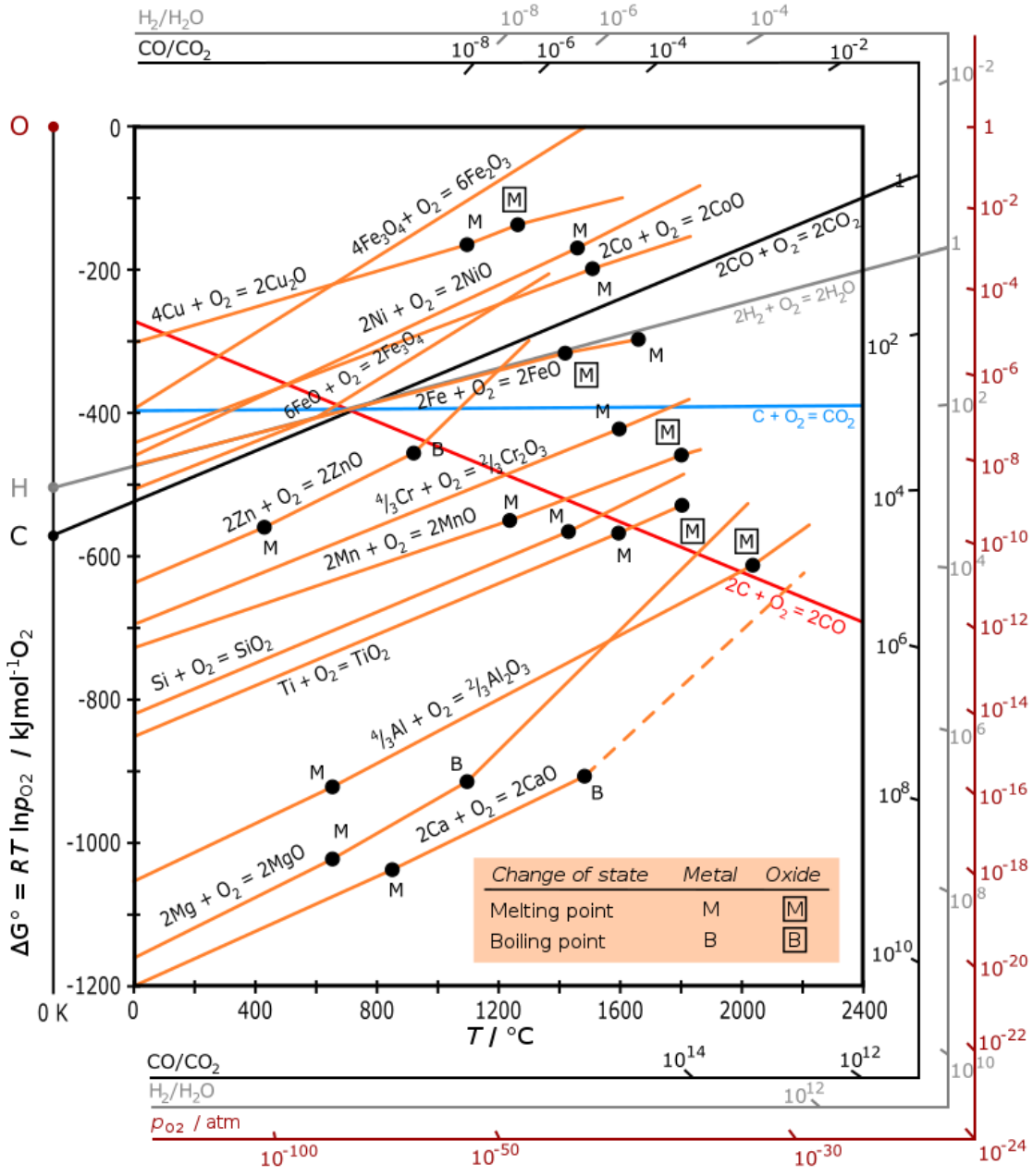

Figure 44: Ellingham Diagram illustrating the changing Gibb's Free Energy for oxidation of various metals

For this experiment, oxidizing conditions were achieved by flowing CO2 [mL/min] at 800 C, and reducing conditions by flowing N2 at 1200 C. Carbon dioxide can be used as a reducing agent as it contains oxygen atoms, and it becomes exactly as reducing as water around 800 C. The effects of temperature and partial pressure of oxygen (or effective pO2) can be visualized with the help of an Ellingham diagram.

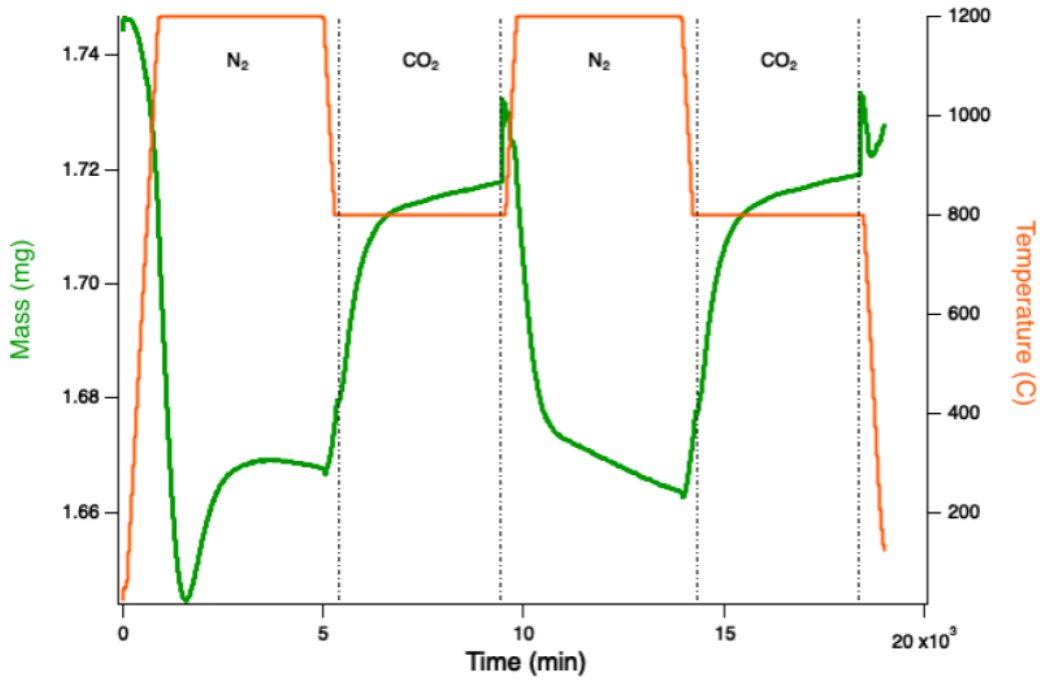

Figure 45: TGA data for CCTM006

As expected, a clear periodic change in mass can be seen as the chamber is cycled between reducing and oxidizing conditions. The first reduction often has a complicated TGA profile resulting from any number of factors, and is usually

disregarded. In this case, we see a dip followed by a momentary increase in mass before leveling off in the first N2 cycle. This may be a result of air trapped within the packed powder reacting with the material, but this is pure speculation. The relevant change in mass, to be used in determining our oxygen δ, is drawn from the peaks and valleys of the remaining cycles. If we take our average peak to be 1.72 mg (just before the sharp cusps) and valley to be 1.67 mg, we can calculate a δ of 0.3 using the following equation:

$$\delta = \frac{\left(1 - {m_f}/{m_i}\right) * M_{mol}}{M_{oxygen}} \tag{31}$$

Powder X ray diffraction

Powder X ray diffraction is a powerful and versatile tool for almost any branch of materials science. It operates under the principle of Bragg's Law, whereby x rays are reflected off crystal planes within a sample, yielding information on lattice spacing and configuration. Here, λ is the x ray photon wavelength, and is commonly that of the copper kα line (1.54 Å). This law describes at which angles incident photon beams will constructively interfere to return a detectable signal reflected on the other side. By virtue of their infinitely repeating lattices within their *space group*, crystal systems exhibit coplanar lattice repetitions in many orientations. These are called Bragg Planes, and they are the reason we see x-ray diffraction patterns. Each Bragg plane is given a name based on the Miller indices which describe its normal

line. As these planes deviate from the 'primary' planes (defined by Miller indices 100, say) the spacing between planes gets smaller, and thus higher 2theta values are needed to achieve constructive interference. Details of the *point group* of the crystal system determine whether a space group peak would become amplified, subdued, or even negated altogether due to secondary interference effects. The entirety of this complex network of effects is compiled into databases, and then used to compare with sample measurements, typically using computer software.

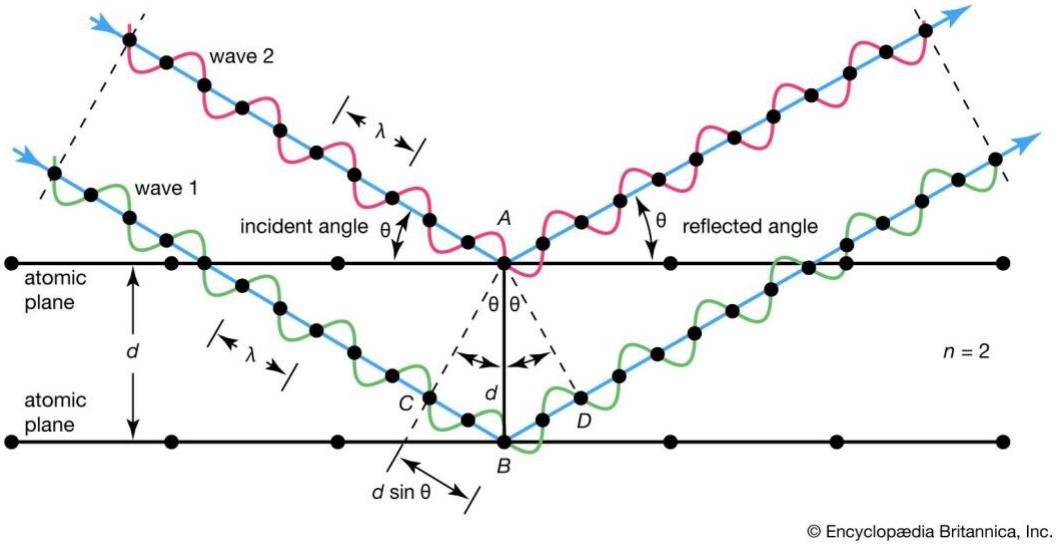

Figure 46: Bragg planes illustrating interference of x-rays

$$n\lambda = 2d * \sin(\theta) \qquad (32)$$

Powder XRD was performed on CCTM by first pulverizing the material, then packing it into a small capillary tube. This tube is then rotated at the point of x-ray beam intersection while the detector moves synchronously with the sweeping emitter. This rotation ensures that no bias is given to any particular Bragg Plane orientation during the packing process.

Phase Analysis:

We can use XRD data to determine relative amounts of any number of given phases. Details on this procedure are given in the next section.

Grain size:

The sharpness of xrd peaks is also a fairly good indicator of how big the grain size is. In particular, large grain size will result in sharp peaks. This is because a larger Bragg plane diffracting x rays results in a more coherent diffraction pattern on the other side. Much like how a diffraction grating will produce a much more segregated pattern than will a double slit of the same spacing.

X-ray Absorption Spectroscopy:

General Theory

Each element has its own characteristic electron cloud, filling orbitals from low to high energy. When considering chemical reactions or [most?] optical interactions, the highest energy valence electrons are the ones making the transitions which lead to these effects. However, it is possible to cause the inner *core* electrons to transition as well, and the energy required to do this falls in the x-ray range of the electromagnetic spectrum. Specifically, XAS observes the process of core electrons getting promoted to the continuum of states accessible within the crystal lattice. To achieve this, a broadband xray source is needed, most commonly provided by a synchrotron source. This can be thought of as a "white light" source, since a broad spectrum of photon energies are contained within. This white light beam passes through a monochromator specially designed to handle x rays. This allows the user to scan through a range of photon energies. The outgoing beam intercepts the sample, whereby core electrons are subjected to a single photon energy at a time. We can think of there being three distinct regions of the ensuing absorption spectrum. The first is known as the pre-edge, and represents electrons promoted just above the fermi layer. The second is where absorption really

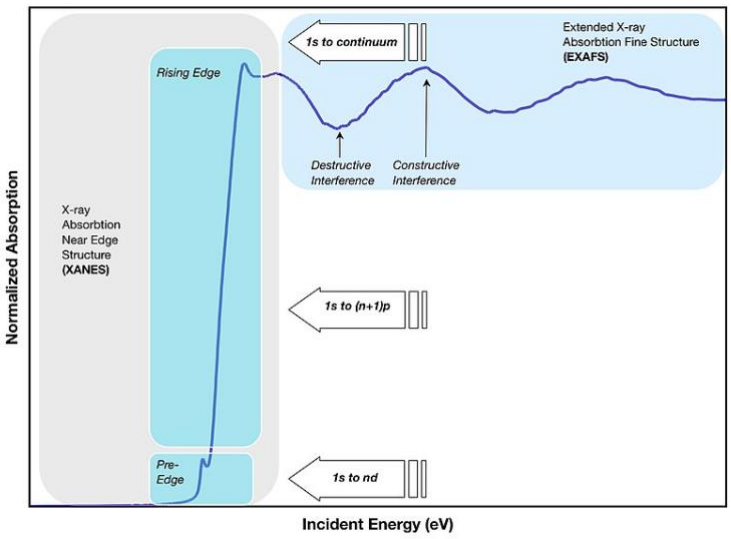

Figure 47: Idealized x-ray absorption data to show distinct regions

ramps up, and is known as the rising edge. Here, electrons are starting to be completely dissociated with the original atom, delocalizing into the continuum states. Third is a long tail region which oscillates as the electron's wave function interfere constructively or destructively. This third region (called EXAFS) has important applications for determining atomic placement within the crystal lattice, but will not be discussed in detail here.

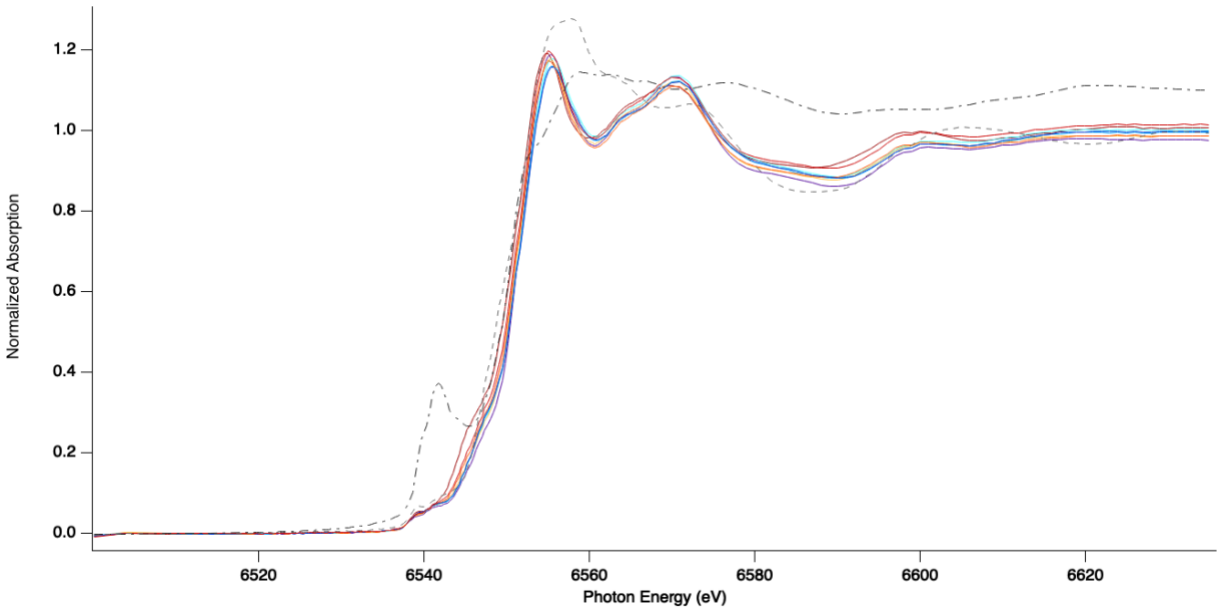

Figure 48: XANES data for Mn K edge of all CCTM samples

Compositional Analysis

Oxidation states were determined by XANES experiments carried out at the SSRL beamline 10-4. Photon energies between 5000-7000 eV were used to obtain x-

ray absorption spectra for each sample at each redox half step, resulting in a total of 48 samples to measure. Sample holders with 8 slots were prepared with powder from each of the seven sampling points for a given stoichiometry (with one left blank), by adhering capton tape fully on one side, putting a scoop of powder in the appropriate slots, then adhering capton tape to the other side. After shaking this around to get a thin, even coating, one side of tape was removed and excess powder allowed to fall out and be collected as waste. Sample holders were mounted on a motorized stand in line with the x-ray beam after passing through a monochromator and adjustable aperture set to 2x8mm. The beam continues on to be intercepted by a thin foil of metallic Ce or Mn (to align spectra taken at different times) and finally the photon count detector. To probe possible redox activity on A and B sites, both Cerium L3 Edge (5723 eV) and Manganese K Edge (6539 eV) regions were scanned. These regions were chosen because they are both classically allowed transitions, making their intensity much stronger, and they fall in the same range to scan on one beamline. References containing known oxidation states of Ce or Mn were scanned, and their XAS spectra compared to those of the samples.

X Ray Data Analysis Techniques and Results

XANES Data Preprocessing

The xray spectroscopy software package Athena was used to process the raw XANES data from SSRL. The software which manages the data collection on

beamline 4-1 saves five columns; a real time clock value (always 1.0), photon energy (in eV), initial intensity (I_0), intensity after passing through the sample (I_1), and the intensity after passing through the reference (I_2). Absorbance is calculated in exactly the same way in x-rays as it is in UV-vis light as explained in chapter 1. Here, sample absorbance is given by $\log(I_0/ I_1)$, and reference absorbance by $\log(I_1/ I_2)$. Athena was developed by Bruce Ravel, and serves as a standard tool for x-ray scientists at SSRL. This software can perform many functions beyond what will be described here.

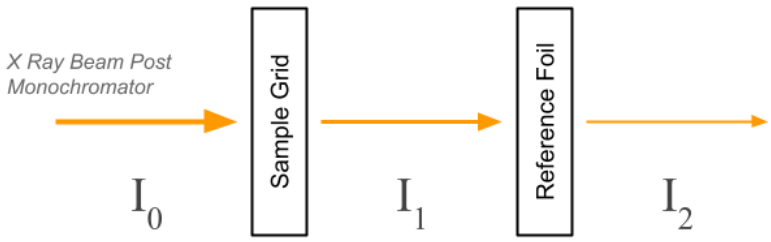

Figure 49: Beamline diagram for x-ray absorption detectors

First, spectra mush be normalized. This is done by first subtracting a background signal. The raw data shows any relevant peaks superimposed with a gentle descending curve. This curve is caused by the energy dependence on attenuation of x-rays within a material. Attenuation is almost linear with energy. To obtain a fit function for the background, the user specifies linear regions both pre- and post- edge, which Athena then uses to compute a linear fit function. After subtracting this function, the height should be normalized to a standard so that any number of spectra can be compared at any point, regardless of the details of the experimental setup. Because of the interference patterns observed after the edge, due to interactions

with neighboring atoms in the lattice, XAS spectra tend to rise to a peak before finally settling down to a lower value. Therefore, normalization entails setting the asymptotic behavior of the absorption data to one. This is achieved simply by dividing the spectrum by a value sufficiently past the band edge.

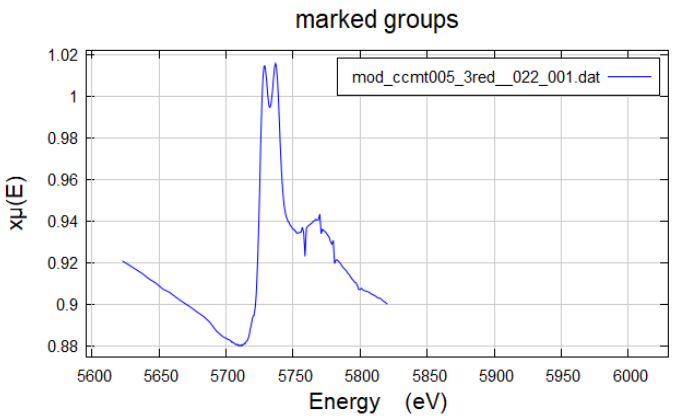

Figure 50: Raw data for CCTM005 Ce L3 edge after 3 reductions

Then, the user may choose to 'flatten' the spectra. This entails fine tuning the post edge background correction so that it settles asymptotically on a horizontal line at y=1.

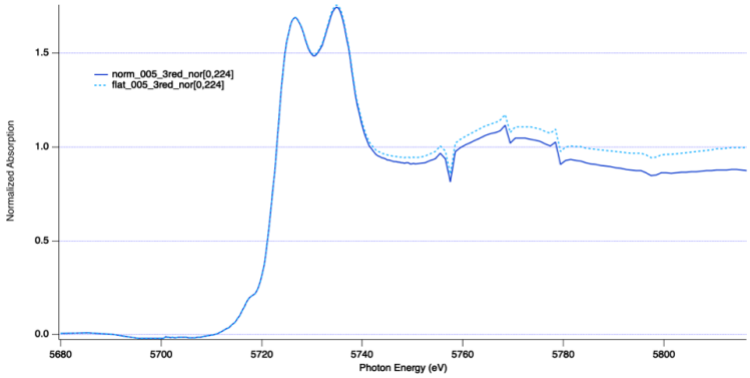

Figure 51: CCTM005 Ce L3 edge (after 3 reductions), after normalization, and after flattening

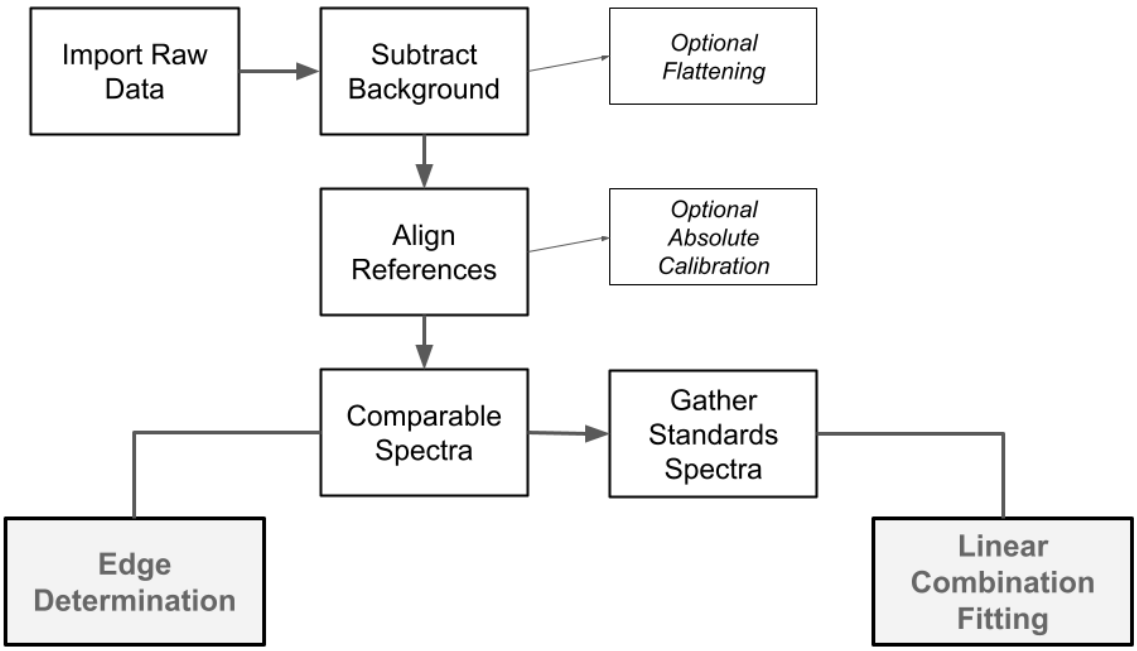

Figure 52: Flow chart for processing raw XANES data

Then, it must be ensured that all the scanning data are aligned properly relative to one another. With many iterations, it is possible for the monochromator motor to offset between runs due to a small amount of hysteresis involved in the gearing. If left uncorrected, this would result in a misinterpreted photon energy value corresponding to the absorption edge. To prevent this from happening, all spectra were aligned using their corresponding reference spectra. After passing through the sample, the xray beam intercepts a thin foil of material containing whichever element is being tested, usually in metallic form. Each scan of a sample simultaneously scans this reference, and it is used to give a standard edge location which does not change between scans. If there were any discrepancy in the photon energies due to hysteresis, this would manifest as a shift in the perceived location of the reference edge. This

shift observed in the reference would then be applied in reverse to the corresponding sample data to undo the unwanted effect. The athena software allows one to shift each scan accordingly, either manually or automatically. The automatic function looks for the best fit of the data within user specified bounds. One can choose any of the above incarnations of the data for the fit function. Alignment for data in this study was done with the automatic function using the derivative of the normalized spectra for the fit function. The resulting fit graphs were inspected manually to minimize errors.

Determining Absorption Edge

Looking at a XANES curve, the first strong absorption peak is known as the "white line". It is known by this name for historical reasons, because the first x-ray absorption measurements were made on photographic paper, and this maximum shows up as a thick white line. However, the white line location is less a representation of the absorption edge as it is the location of the first constructive interference for the electron based on the complex interactions within the lattice. Far more useful is to look at the leading edge of the peak as it rises. There are a couple of common ways to estimate this. One is to use the inflection point in the leading edge as the absorption edge. Since an inflection point in a function is the location of the zero crossing in the second derivative of that function, we can equally visualize this as the location of a peak in the first derivative. With very clean data, this works nicely.[41] However, with noisy data, this method can be problematic because there

is no one clean location to point to for the peak. Many small bumps may exist in the peak which would manifest as multiple zero crossings, leading to ambiguity and erroneous results.

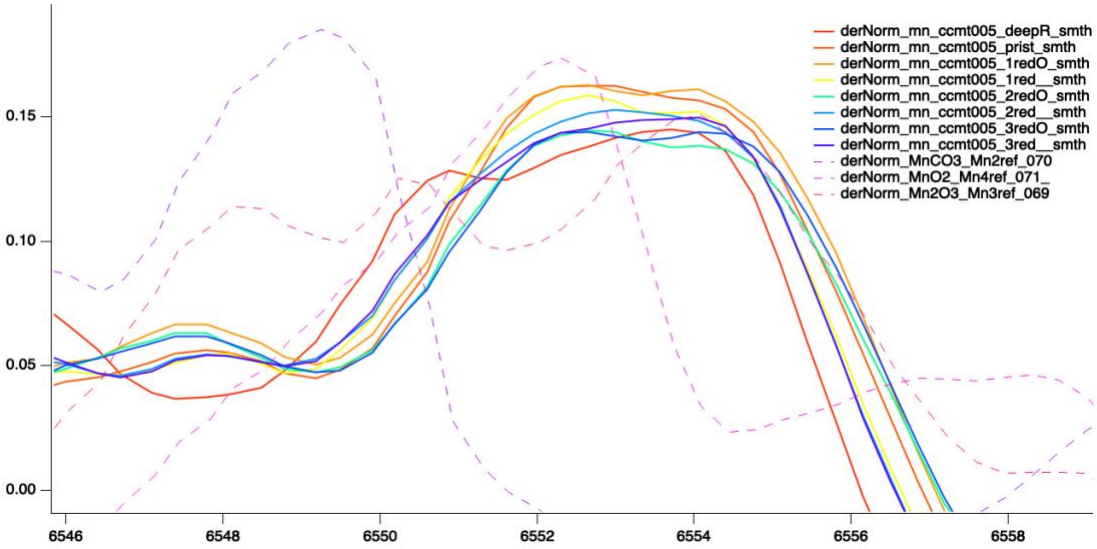

Figure 53: First derivative of Mn K edge across all redox steps for CCTM005 and references

Even with a smoothing function applied, as shown in the above figure, the peak location is not easily pinpointed. More reliable and efficient is to use the photon energy at which the curve crosses a standardized value of absorption as the absorption edge. With the preprocessing yielding normalized, flattened curves, in which the trailing edge approaches an absorption of '1', it is standard to use a value of 0.5 for this crossing. In other words, whatever the x value for each curve where it intersects a

horizontal line at y=0.5, that is taken to be the edge. As shown below, this yields much cleaner results which are largely unaffected by small amounts of noise in the data.

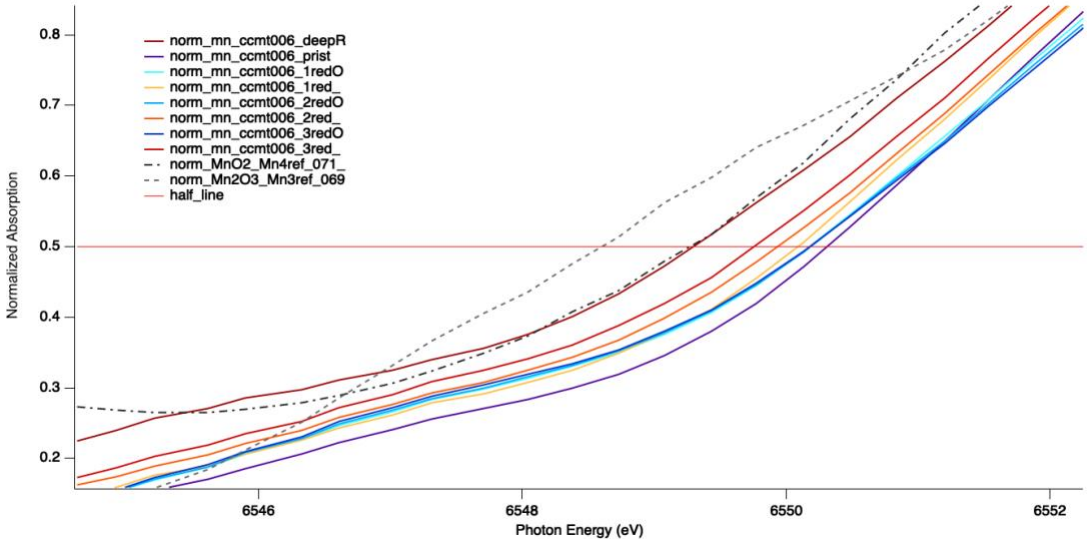

Figure 54: Mn K edge for CCTM006 and references, showing absorption edge via half-line crossing

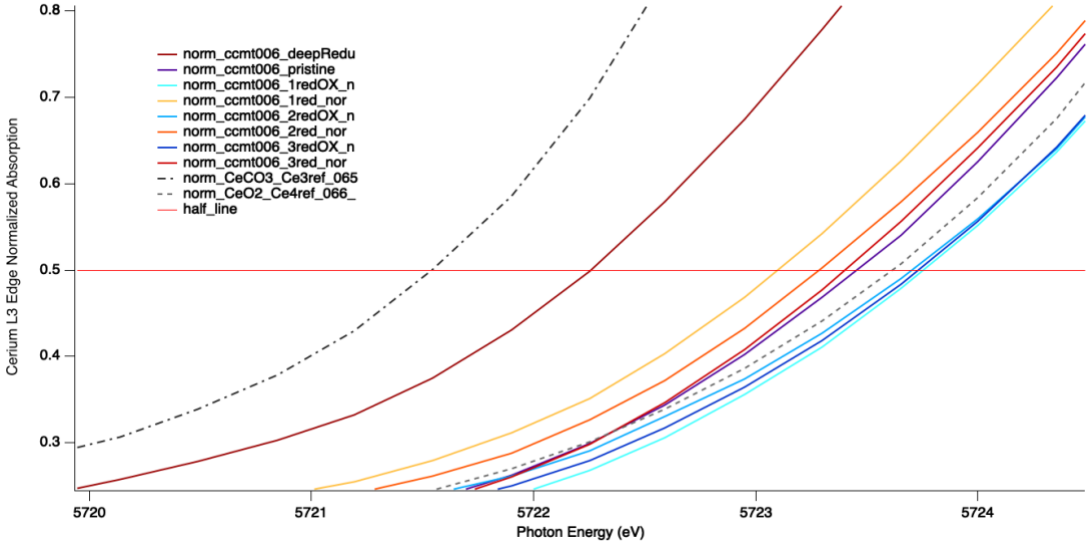

Figure 55: Ce L3 edge for CCTM006 and references, showing absorption edge via half-line crossing

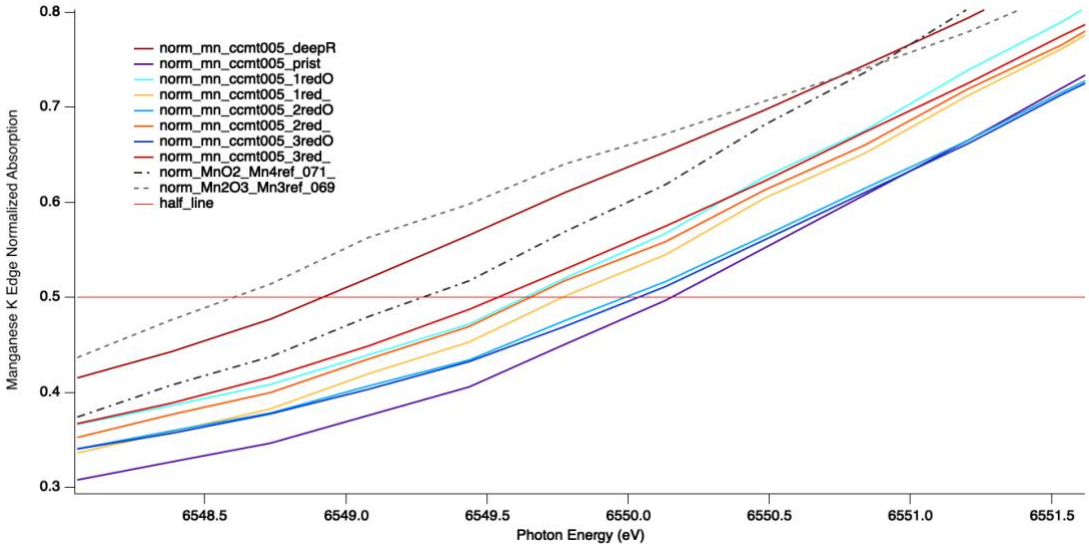

Figure 56: Mn K edge for CCTM005 and references, showing absorption edge via half-line crossing

Plotted alongside the sample spectra are relevant ionic standards. For each element investigated, we are expecting to see some mixture of different oxidation states represented. It is helpful to measure and plot these reference spectra to get a

sense of what portion of each oxidation state is present in the samples. With clean data, it should be possible to perform a linear combination fit of reference spectra to determine this. However, it can be seen from two of the above plots that the XAS spectra of the samples do not fall cleanly between the spectra of the reference standards. Specifically this is true for detection of the Manganese K edge. The Mn standards used were MnO_2 (Mn^{4+}), Mn_2O_3 (Mn^{3+}), and $MnCO_3$ (Mn^{2+}). Manganese demonstrates a wide variety of oxidation states, and they can fairly easily convert from one to the other given enough time. It is likely that the Mn^{4+} reference used in this case was not entirely pure, complicating efforts to determine exact ionic states. The reference in question had been stored for an unknown, but assuredly long, time within the SSRL basement. Despite the relatively high stability of MnO_2, it is possible that some fraction of it had undergone phase transformation to Mn_2O_3 over the course of decades. Therefore only measurements relative to other samples are to be trusted in the data shown. For all cerium spectra, the standards appear to be behaving as one would hope.

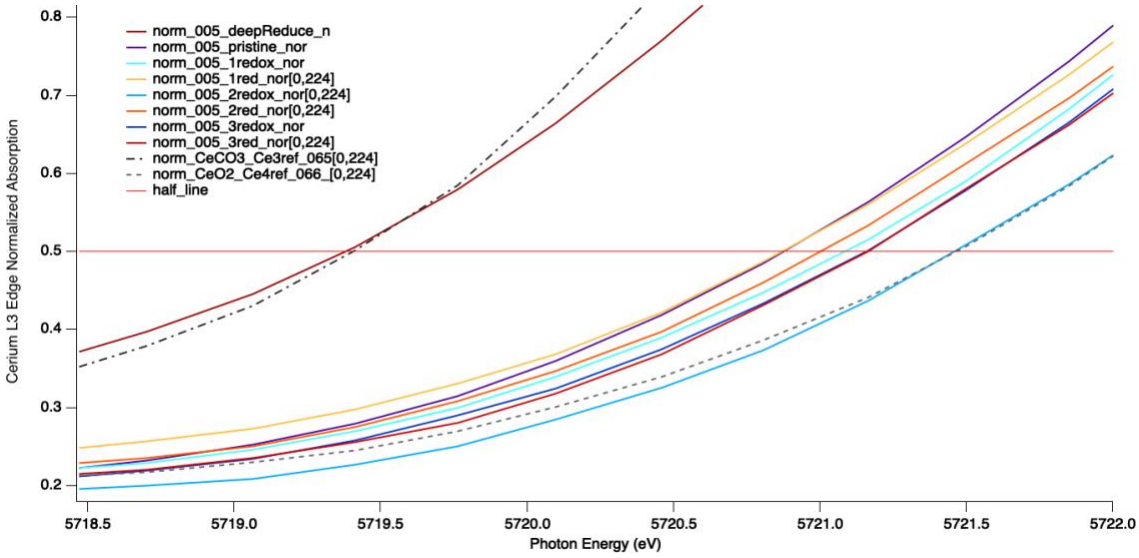

Figure 57: Ce L3 edge for CCTM005 and references, showing absorption edge via half-line crossing

Phase Content

Because of the constraints a particular crystal system imposes on its Bragg planes, XRD is well suited to determine which phase a material is in, or even what fraction of phases are present in a given mixture. To determine this accurately, however, requires that certain rules be followed.

The material is crushed into a relatively fine powder (~_um), and spread thinly onto a substrate such that the grain orientation is completely random. If there is any preferred orientation, some characteristic XRD peaks will be much higher, while others appear much lower or absent altogether. The nature of the XRD 2 theta measurement is that one is observing which Bragg planes *happen* to be parallel to the surface for a particular corresponding 2 theta value. If one of these planes has a

statistical likelihood to be pointing in that direction, one will see a much stronger peak than predicted.

The list of potential phases must be sufficiently small, and well established. Enough crystal phase combinations put together will have too many overlapping peaks to some other combination to be able to distinguish them reliably. Each peak in an XRD plot represents a Bragg Plane of some crystal phase within the sample. If two or more crystal species are present, the resulting plot will be equivalent to each individual plot overlaid with one another. It is common practice to label each peak with the material name and Miller Indeces associated with the plane. This allows us to observe when phase fractions change, or disappear altogether.

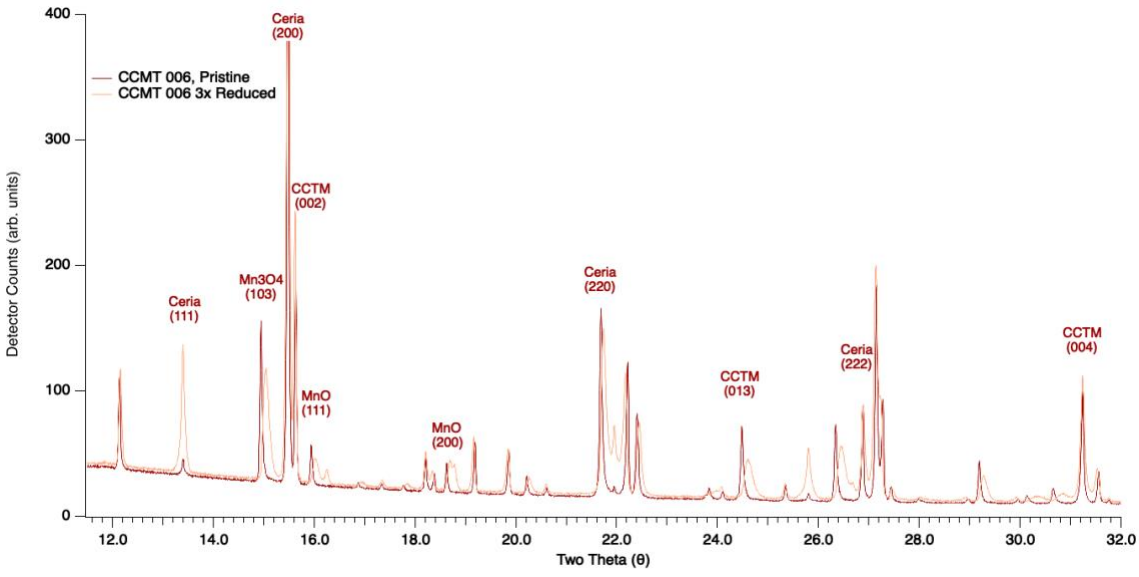

Figure 58: XRD data for CCTM and associated phases with labeled peaks

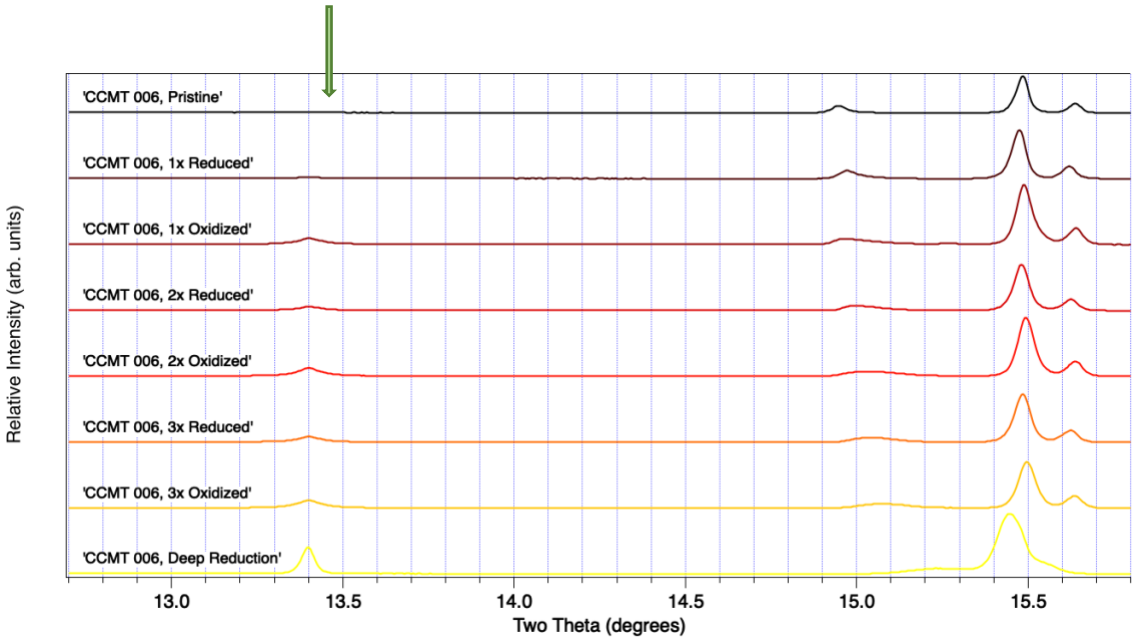

Figure 59: XRD for CCTM006 across all redox steps

It can be seen above that a ceria phase develops throughout the redox cycling of CCTM006. It starts very small, but develops (especially during oxidation steps) until becoming highly pronounced after a deep reduction. The main identifying peak for the CCTM phase, at ~15.65º, remains throughout normal cycling, but disappears entirely after a deep reduction. This is evidently the point where CCTM has been completely decomposed into ceria and other Mn compounds.

The same plot for CCTM008 shown below reveals a different story. It appears to start with no ceria content, and continues to not develop any until the final deep reduction. It also has a much lower signal for alternate Mn phases. This would seem to indicate a higher phase stability, which could help explain its high cycling δ measured from the mass changes.

With some prior knowledge of possible phases present, we can use a database and software to determine explicitly the percentages of each comprising our sample. The following data were obtained using Rietfield Refinement and reveal the phase fractions present in our pristine samples, prior to any redox cycling.

Table 9: Lattice parameter and phase fraction for all CCTM stoichiometries, as determined by Rietfield refinement

Sample Name	*Ce Fraction*	*Mn Fraction*	*'a'*	*'b'*	*'c'*	*CCTM Weight %*	*Ceria Weight %*
CCTM 005	0.35	0.70	5.61394	7.55614	5.35475	98.818	1.182
CCTM 006	0.33	0.67	5.60293	7.56324	5.3574	99.165	0.835
CCTM 007	0.30	0.70	5.56026	7.56281	5.3545	100	0
CCTM 008	0.30	0.80	5.52536	7.55265	5.34687	100	0
CCTM 009	0.30	0.75	5.54313	7.55736	5.3504	99.562	0.438
CCTM 010	0.25	0.50	5.52857	7.60451	5.37273	98.924	1.076

Lattice Parameter Shifting

The distances between lattice repetitions (in 3 dimension) are known as lattice parameters. A crystal can maintain its space group, while expanding or contracting under the influence of any number of physical circumstances. This can occur due to

replacement of one element with another withing the lattice, physical strain, or temperature difference. Even slight changes in these spacings will affect the diffraction pattern observed, and this change can be determined by comparing XRD f rom two samples. Although the theory underpinning these changes is quite complex, the qualitative effect can be seen as a shifting right or left of XRD peaks.

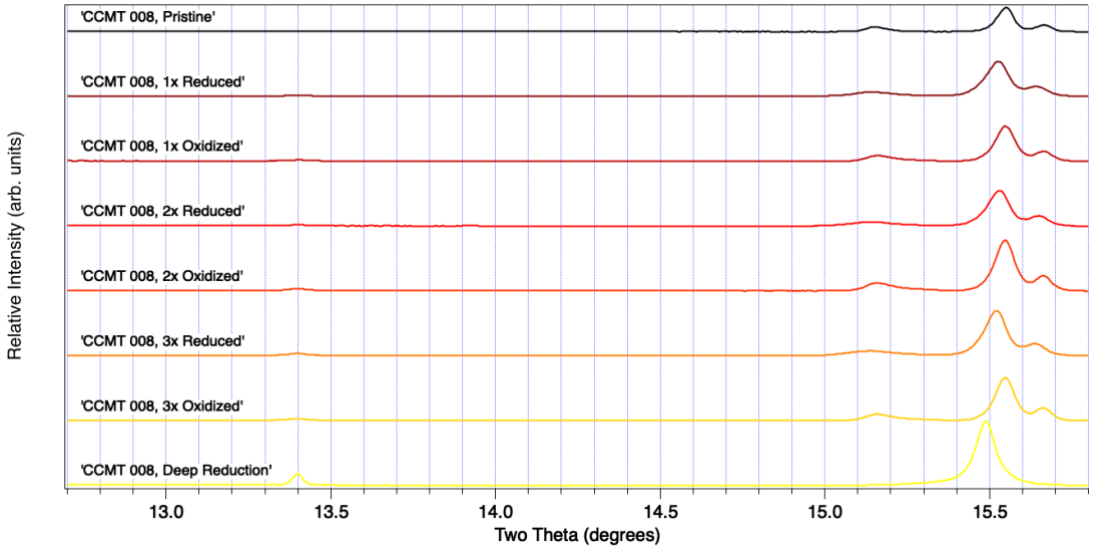

Figure 60: Zoom-in on CCTM008 XRD to illustrate lattice parameter shifting

Here, we can clearly see a shifting to the left for each reduced sample (red tones) and a shift back to the right for oxidized samples (blue tones). Following from Bragg's Law, if the xray excitation energy is held constant, then an increase in 'd' should be accompanied by a decrease in 'θ', effectively shifting a peak to the left. Thus, it is observed that reducing the material overall increases lattice parameters, and reoxidizing decreases them. At first glance, this may feel counterintuitive.

Afterall, oxidizing this oxide perovskite means inserting an oxygen atom into a spot which had been previously vacated.

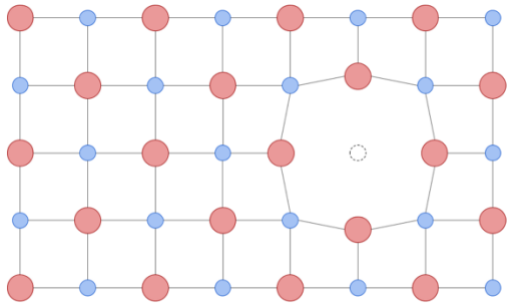

Figure 61: Illustration of lattice parameter expansion due to oxygen vacancy

We can reason this out by noting the high electronegativity of oxygen. While engaged in a chemical bond within the perovskite crystal (or any compound for that matter) oxygen assumes an oxidation state of [-2]. Effectively, this means that two extra electrons have localized around oxygen, and it now constitutes a region of negative charge. All A and B site cations have a positive charge, and they are drawn closer to the oxygen site due to coulombic interaction. This has the overall effect of tightening up the lattice and decreasing the spacing.

In opposition of this, is the smaller effect of expansion of the lattice by the replacement of a smaller cation with a larger one. At first glance, it is tempting to think that replacing calcium (Z=20) with cerium (Z=58) would provide this expansion. However, a closer look reveals that the sizes of the two cations are actually on par. Atomic radius depends much on environmental conditions, including oxidation state and nearest neighbor. Of the samples made, CCTM005 (Ca 0.65, Ce

0.35) and CCTM010 (Ca 0.75, Ce 0.25) represent the largest difference in cerium content. However, examining their relative XRD plots at identical redox steps, we do not see the largest shift in peaks between two samples.

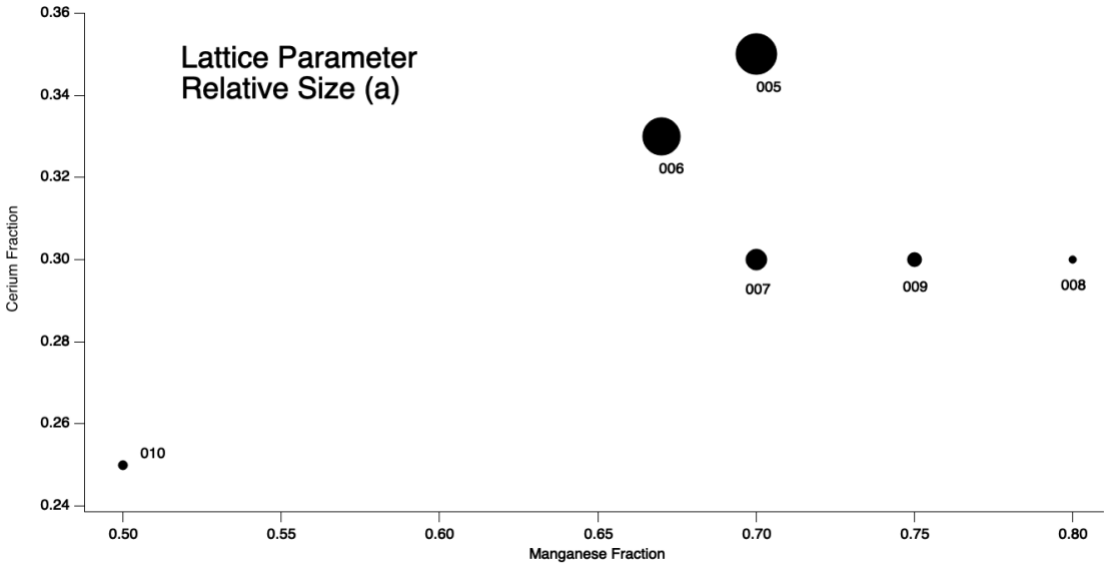

Figure 62: Lattice parameter 'a' across all CCTM stoichiometries

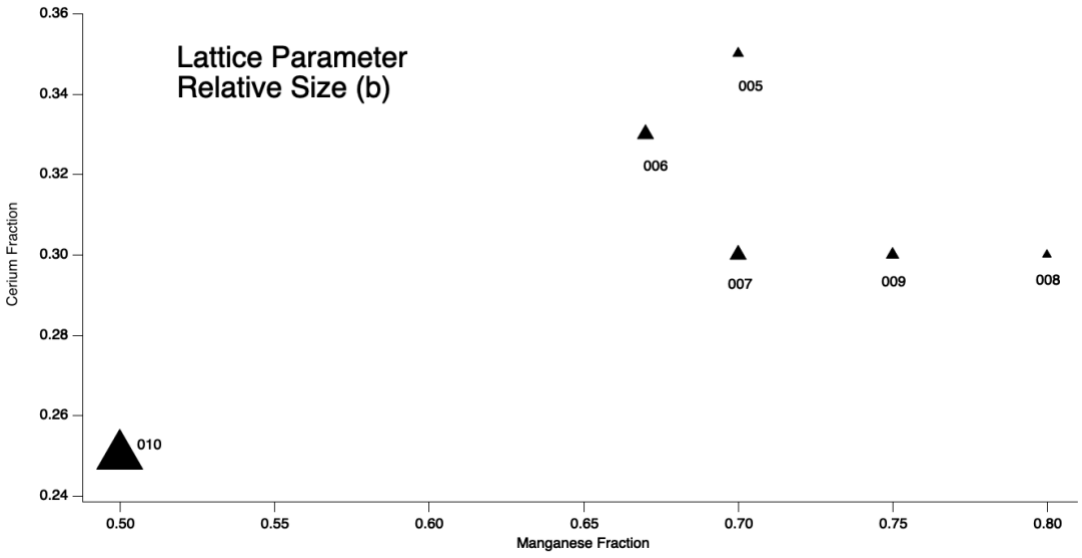

Figure 63: Lattice parameter 'b' across all CCTM stoichiometries

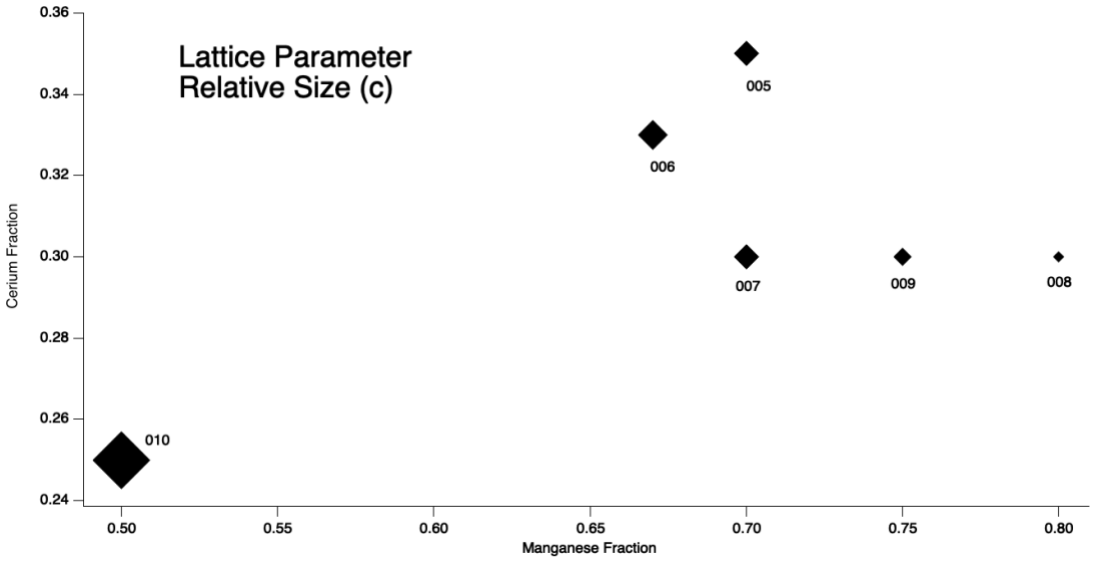

Figure 64: Lattice parameter 'c' across all CCTM stoichiometries

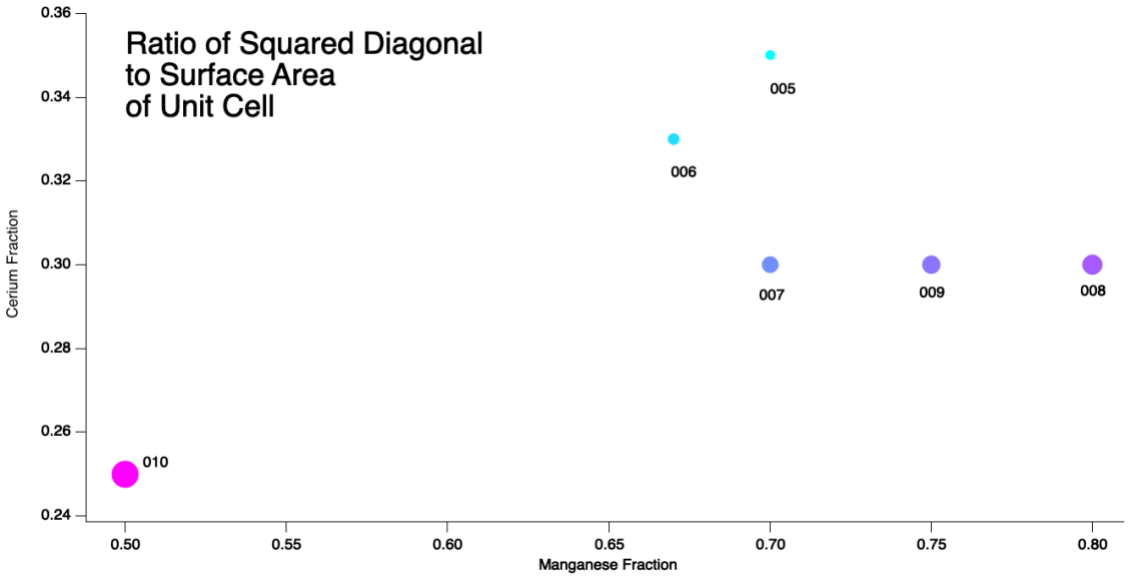

Figure 65: "Squareness index" across all CCTM stoichiometries

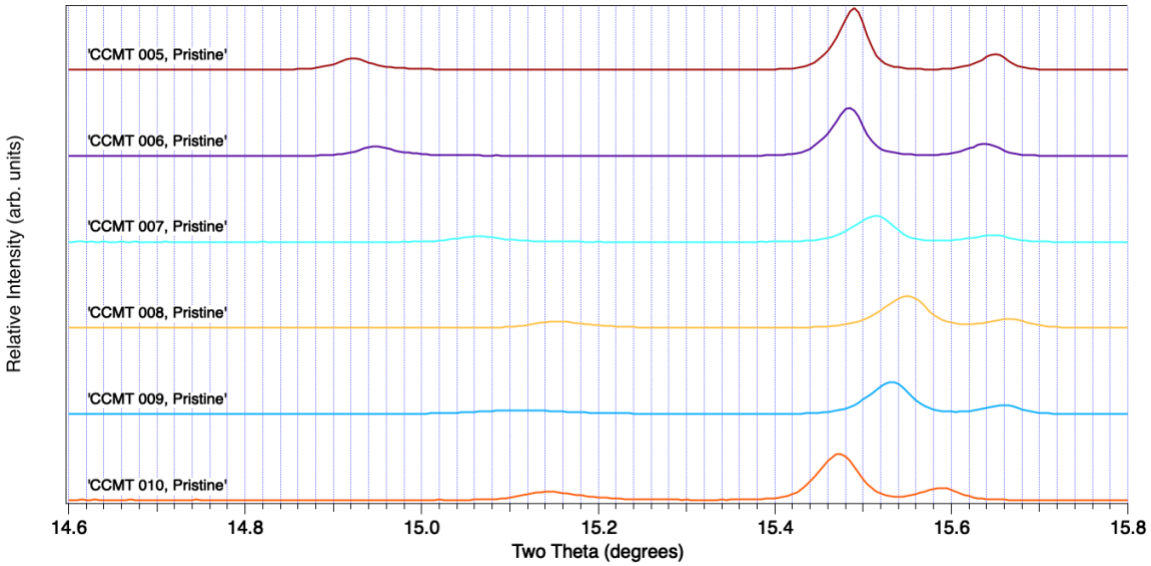

Figure 66: XRD zoomed in for pristine state of all CCTM stoichiometries

For a perovskite to form a stable configuration from two cations and an anion, certain geometric conditions must be met. The physical chemist, Goldschmidt, worked out a formula which summarizes these conditions into one parameter known as the tolerance factor (t).[42]

$$t = \frac{r_A + r_O}{\sqrt{2}(r_B + r_O)} \tag{33}$$

If *t* falls in the range of roughly 0.8 – 1.0, it is generally thought to be stable.

Table 10: Atomic radii of various ionic/oxidation states of elements in CCTM

Element/ Ox. State	**-2**	**-1**	**+1**	**+2**	**+3**	**+4**
Ca				114		
Ce					115	101
Ti				100	81	74.5
Mn (low spin)				81	72	67
Mn (high spin)				97	78.5	
Oxygen	126					

Redox Cycling Mass Changes

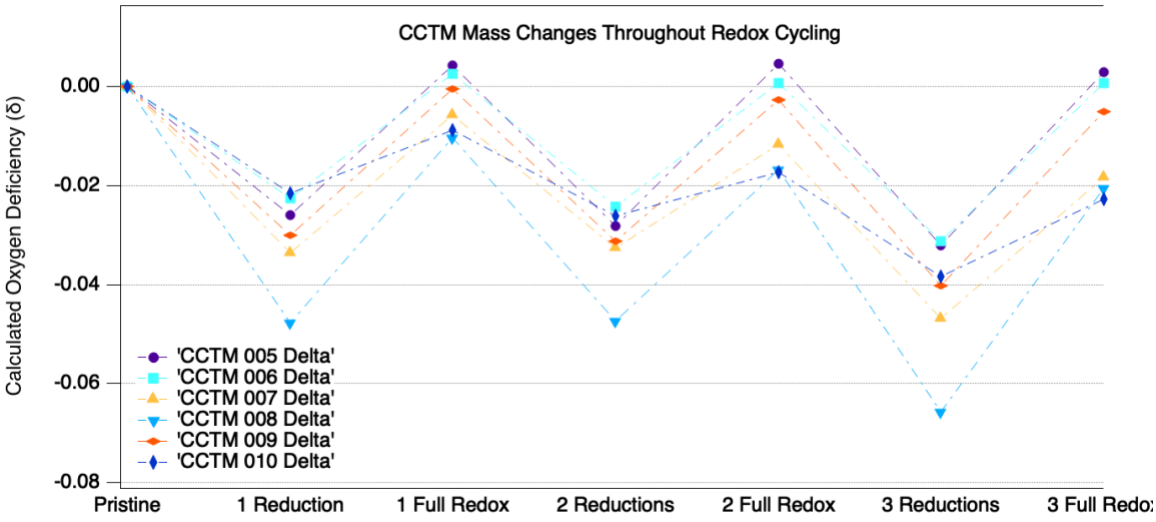

Figure 67: Changes in mass throughout redox cycling for all CCTM stoichiometries, and implied oxygen deltas

While many of the results seem inconclusive or even contradictory, there is one trend which sticks out. The average change in mass between an oxidation and reduction step correlated with the fractional Manganese content of the sample. This change in mass, in turn, is associated with an experimental fraction of oxygen site vacancy δ. In other words, the higher the Mn fraction, the more fully the material can reduce. A higher depth of reduction allows for more oxygen atoms to be split from water molecules, thus generating more hydrogen. When converted to units of δ, these 6 stoichiometries ranged from 0.02-0.04 when averaged over three cycles. The state of the art material ceria typically experiences a maximum δ of ~0.05[37], indicating a potentially competitive material.

To probe the underlying causes of this trend, let's consider another STCH material, BCM. Ba(Ce,Mn)O has been recently studied and reported on as a potential water splitter. It balances the voracious oxygen-stripping properties of Cerium 3, with the reducibility of Manganese 4.

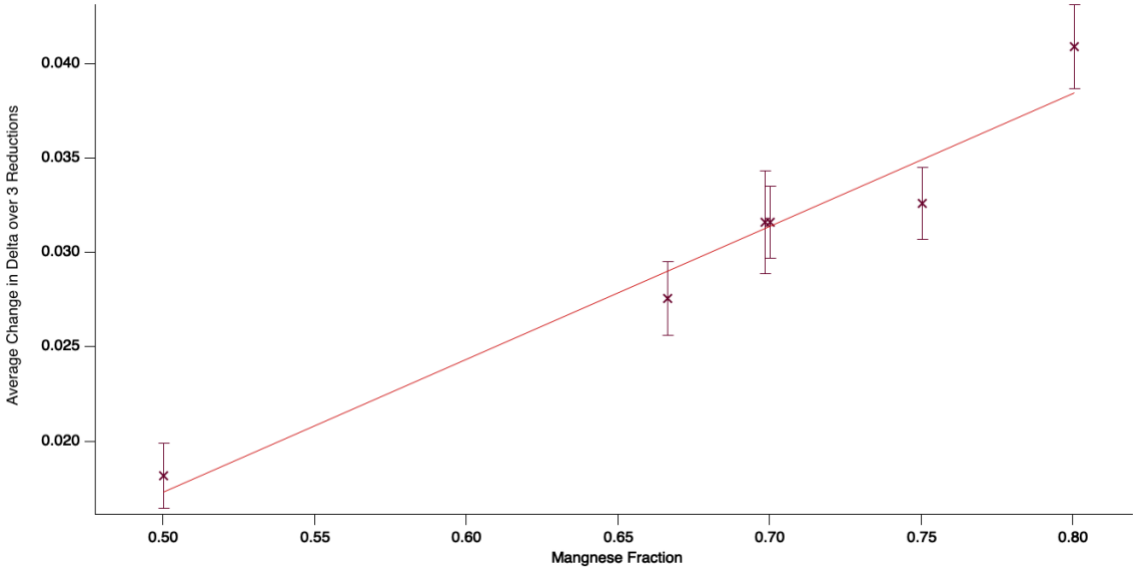

Figure 68: Oxide reduction potential as a function of manganese content

Conclusions and Remarks

To compete with a benchmark STCH material like ceria, new systems must exhibit a high rate of hydrogen generation while also reducing fully at reasonably low temperatures. Reducing the perovskite structure effectively resets the crystal, allowing for the next round of water splitting. Newly identified CCTM2112 has been shown to outperform ceria in terms of hydrogen production capacity as tested in a flow reactor. Additionally, it shows adequate reduction at the relatively low temperature of 1350C. Lowering the reduction temperature is crucial for scalability for industrial application. For reaction chamber designs which incorporate a window to allow light in, quartz is the most viable solution, which cannot operate much past

this threshold. Even the ceramic insulator materials which line the walls of the chamber benefit from lowering the maximum temperature.

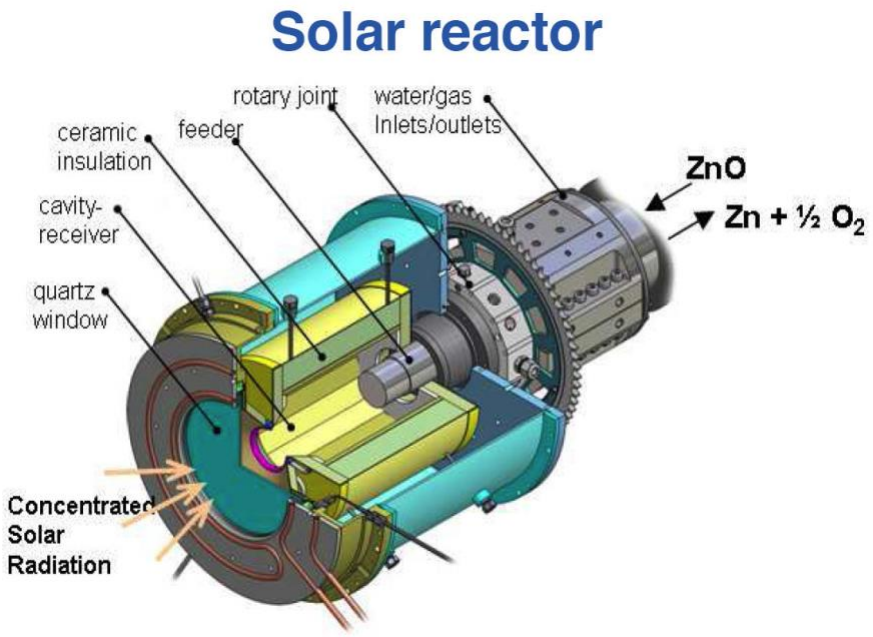

Figure 69: Diagram of a potential real world STCH reactor

Another key finding of the study is that, for a wide range of stoichiometries, CCTM remains stable through high temperature redox cycling. This is reflected in the XRD data by diffraction peaks which always revert back to the previous pattern after shifting. Many materials undergo an [irreversible?] change of phase when exposed to harsh conditions such as high temperatures and highly reducing or oxidizing environments. It is often the case that the new phase does not have the same desired properties as the original, compromising the function of the material. Take the recently investigated BCM alluded to earlier; which initially exhibits a high percentage of the so-called 10H phase. This phase reduces beyond the point where it can recover its mass fully by subsequent reoxidation. However, the majority of the

material is converted to a 12R phase at this point, which does demonstrate full cyclability.[37]

As a general guiding principle, a good STCH material will be one which exists on the brink of stability, allowing oxygen vacancies to form in its lattice, but easily refilling them as well. All the while, the crystal must expand and contract, much like lungs breathing air in and out, without causing any irreversible changes. This is a delicate balance between stability and instability. Certain stoichiometric ratios of CCTM appear to achieve this balance, allowing for vacancies to form and then fill without changing phase. This is due, in part at least, to the combined influence of enthalpy and entropy changes which drive the reaction in opposite ways depending on the cycling conditions. During the oxidation step, a large (negative) change in enthalpy associated with filling an oxygen vacancy drives the reaction forward. This is therefore an exothermic reaction, releasing heat, which can be carried out at relatively low temperature. During the reduction step, enthalpy alone is no longer enough to drive the reaction, because it requires an input of energy to create a vacancy. Fortunately, exposing CCTM to higher temperatures during reduction is able to take advantage of the favorable change in entropy involved in forming vacancies. Formally, the Gibb's Free Energy of a reactants and products is used to determine if a reaction will occur or not.

$$G = \Delta H - T\Delta S \tag{34}$$

Because the energetics influence from entropy (S) depends on temperature, but the enthalpy (H) term does not, the system can cycle along with the temperature. In theory, the ideal H and S would be one which makes G=0 at the mean value of T between high and low… in other words;

$$0 = \Delta H - (1373)\Delta S. \quad \rightarrow \quad \Delta S = \Delta H/1373$$

The emergent material CCTM has shown initial promise as a STCH material, and future work should be directed at optimizing the stoichiometry for water splitting. While a first look indicates that increasing the Manganese content of the B site of CCTM directly corresponds to an increase in redox cycling potential, water splitting measurements have yet to be performed on them to back up this claim. Furthermore, mass change data and XAS peak shifting during redox cycling were not in total agreement.

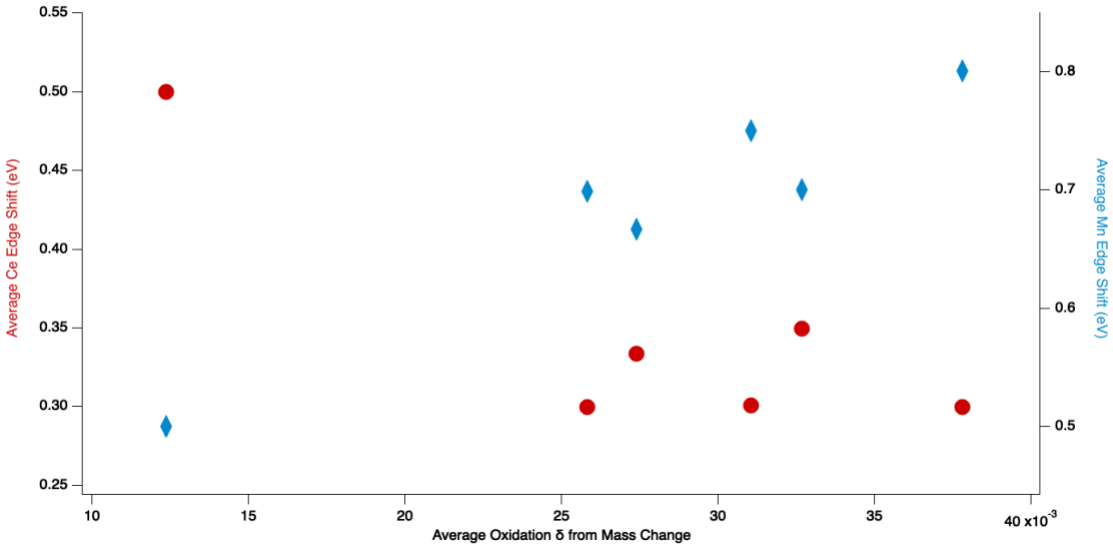

However, the oxidation state alone does not tell us how effectively it will split water if we cannot assume phase purity. It can be inferred from the results that multiple phases are evolving as the redox cycling continues. For the sake of analysis, we will limit these phases to ceria (CeO_2) and Mn_3O_4, which exhibits a mixed oxidation state of Mn, such that each unit cell remains neutral. To illustrate this, below are shown the chemical reactions assuming either perfect phase purity, or complete decomposition, respectively. In the interest of simplicity, each mixed cation cite of the perovskite structure is denoted with its default symbol of A or B.

$$ABO_3 \rightarrow ABO_{3-\delta} + \frac{\delta}{2}O_2 \tag{35}$$

$$ABO_3 \rightarrow AO_2 + B_3O_{4-\delta} + \left(\frac{\delta - 1}{6}\right)O_2 \tag{36}$$

The balancing for the first case is straight forward. For the second case, we have assumed that ceria (shown as AO_2) cannot reduce, and any oxygen δ is due to activity by the manganese oxide. This is realistic due to the aforementioned relative ease of reduction of Mn compounds. The takeaway from the above comparison is that, depending on the phases produced, the same number of oxygen vacancies created can yield very different mass changes. In this way, we can reason why CCTM008 exhibits the highest average mass change despite showing average XAS edge shifting.

Curiously, there did not seem to be a direct correlation between Mn and Ce redox activity, as shown by XAS. For example, CCTM008 shows a shift in XAS edge that is roughly equal for both Mn and Ce. Meanwhile, CCTM010 shows a larger average shift for cerium even than 008, while showing almost no change in the absorption edge for manganese. Because of the compromised references, we cannot directly compare the importance of each element's edge shift, but we can compare their relative activity.

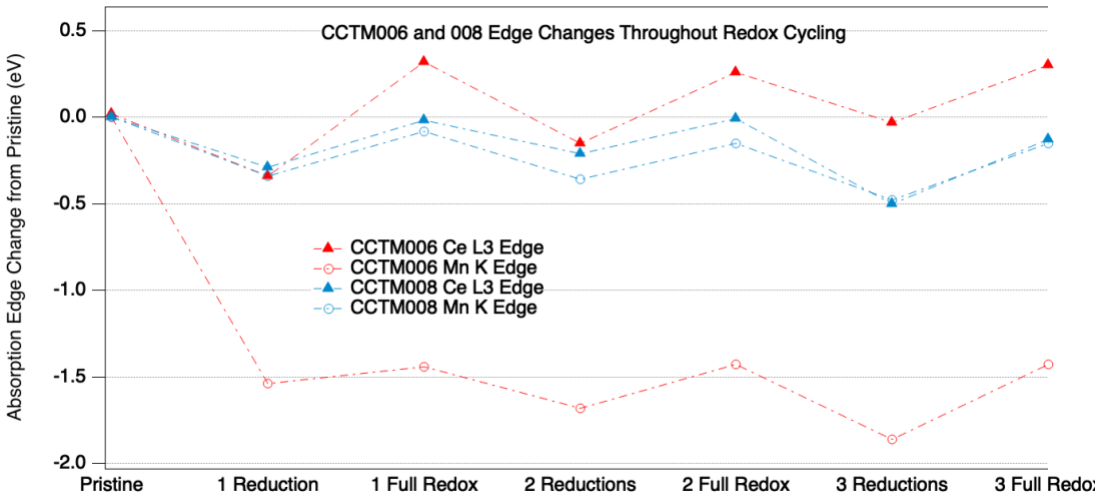

Disregarding CCTM010, which had an extremely low Mn proportion relative to the rest, 006 and 008 represent the lowest and highest presumed water splitting potential based on mass change data. Shown above are the XAS edge shifting data for both redox active elements, for both samples at hand. While 008 shows very regular and balanced shifting on both sites, 006 shows quite the opposite. Upon the very first reduction step, we see the Mn K edge of CCTM006 plummet, indicating extreme initial reduction. From here, Mn proceeds to cycle somewhat regularly.

Simultaneously, the Ce L3 edge actually shows a gradual oxidizing trend throughout cycling. This would most likely imply that pristine (uncycled) 006 starts out with Ce in a mixed oxidation state between 3+ and 4+, and continues to reoxidize to a 4+ state. The large proportion of ceria seen in the XRD data supports this.

From the evidence shown throughout this second chapter, what we can generally state is that CCTM can potentially become a competitive water splitter, and its viability depends largely on its manganese content. Future work should focus on varying the Mn content while fixing the A site stoichiometry at one, or maybe a few, Ce fractions. The original theoretical work pointed to the viability of CCM (containing no Titanium on the B site), but this was found to be unstable and decompose into alternative phases. We should see what the upper bound of Mn content is for this crystal system, and if the trend holds until the limit. If a truly stable stoichiometry of CCTM can be found, economical water splitting for hydrogen production may be possible with nothing but solar derived heat and steam as inputs. As we strive toward a carbon neutral energy economy, solar thermochemical hydrogen may just yet have a seat at the table.

References

[1] "Frequently Asked Questions (FAQs) - U.S. Energy Information Administration (EIA)." https://www.eia.gov/tools/faqs/faq.php (accessed Aug. 23, 2023).

[2] R. G. Newell, W. A. Pizer, and D. Raimi, "U.S. federal government subsidies for clean energy: Design choices and implications," *Energy Econ.*, vol. 80, pp. 831–841, May 2019, doi: 10.1016/j.eneco.2019.02.018.

[3] J. Nelson, *The Physics of Solar Cells*. in Series on Properties of Semiconductor Materials. Imperial College Press, 2003. [Online]. Available: https://books.google.com/books?id=s5NN34HLWO8C

[4] A. Borrelli, "The emergence of selection rules and their encounter with group theory, 1913–1927," *Stud. Hist. Philos. Sci. Part B Stud. Hist. Philos. Mod. Phys.*, vol. 40, no. 4, pp. 327–337, Dec. 2009, doi: 10.1016/j.shpsb.2009.05.002.

[5] A. M. Hermann, "Luminescent solar concentrators—A review," *Sol. Energy*, vol. 29, no. 4, pp. 323–329, Jan. 1982, doi: 10.1016/0038-092X(82)90247-X.

[6] "Dataset on the absorption characteristics of extracted phytoplankton pigments - PMC." https://www.ncbi.nlm.nih.gov/pmc/articles/PMC6461595/ (accessed Aug. 23, 2023).

[7] "Reference Air Mass 1.5 Spectra." https://www.nrel.gov/grid/solar-resource/spectra-am1.5.html (accessed Aug. 23, 2023).

[8] "Perylene," *Wikipedia*. Dec. 06, 2021. Accessed: Aug. 23, 2023. [Online]. Available: https://en.wikipedia.org/w/index.php?title=Perylene&oldid=1059020498

[9] L. R. Wilson, B. C. Rowan, N. Robertson, O. Moudam, A. C. Jones, and B. S. Richards, "Characterization and reduction of reabsorption losses in luminescent solar concentrators," *Appl. Opt.*, vol. 49, no. 9, p. 1651, Mar. 2010, doi: 10.1364/AO.49.001651.

[10] C. Corrado, S. W. Leow, M. Osborn, E. Chan, B. Balaban, and S. A. Carter, "Optimization of gain and energy conversion efficiency using front-facing photovoltaic cell luminescent solar concentratordesign," *Sol. Energy Mater. Sol. Cells*, vol. 111, pp. 74–81, Apr. 2013, doi: 10.1016/j.solmat.2012.12.030.

[11] “ChromatiNet Shade Nets: 20-80% Shade | Quick Ship, Cut to Size, No Mins. | Green-Tek,” Dec. 26, 2016. https://green-tek.com/shade_nets_chromatinet/, https://green-tek.com/shade_nets_chromatinet/ (accessed Aug. 27, 2023).

[12] C. Wang *et al.*, “Efficiency improvement by near infrared quantum dots for luminescent solar concentrators,” in *Next Generation (Nano) Photonic and Cell Technologies for Solar Energy Conversion*, International Society for Optics and Photonics, Aug. 2010, p. 77720G. doi: 10.1117/12.860094.

[13] H. Shen *et al.*, “Rational Design of NIR-II AIEgens with Ultrahigh Quantum Yields for Photo- and Chemiluminescence Imaging,” *J. Am. Chem. Soc.*, vol. 144, no. 33, pp. 15391–15402, Aug. 2022, doi: 10.1021/jacs.2c07443.

[14] B. Valeur, *Molecular Fluorescence Principles and Applications*. 2001.

[15] N. Sahu, B. Parija, and S. Panigrahi, “Fundamental understanding and modeling of spin coating process: A review,” *Indian J. Phys.*, vol. 83, no. 4, pp. 493–502, Apr. 2009, doi: 10.1007/s12648-009-0009-z.

[16] “Influence of Surface Ligands on the Luminescent Properties of Cadmium Selenide Quantum Dots in a Polymethylmethacrylate Matrix | Elsevier Enhanced Reader.” https://reader.elsevier.com/reader/sd/pii/S1875389215013103?token=778559B9DBF3CBE0B2458562F3AFB07C8A3A2725F9BBAC7C134A3B6B8F6A4D029701360793828DA0CB28EFE3F6DAD81F&originRegion=us-east-1&originCreation=20211021203201 (accessed Oct. 21, 2021).

[17] E. T. Vickers *et al.*, “Enhancing Charge Carrier Delocalization in Perovskite Quantum Dot Solids with Energetically Aligned Conjugated Capping Ligands,” *ACS Energy Lett.*, vol. 5, no. 3, pp. 817–825, Mar. 2020, doi: 10.1021/acsenergylett.0c00093.

[18] E. Enlow and S. A. Carter, “Tunable emission color of methylammonium lead bromide perovskite quantum dots by varying ligand quantity,” in *Light-Emitting Devices, Materials, and Applications XXVI*, SPIE, 2022, pp. 145–153.

[19] J. L. Banal, B. Zhang, D. J. Jones, K. P. Ghiggino, and W. W. H. Wong, “Emissive Molecular Aggregates and Energy Migration in Luminescent Solar Concentrators,” *Acc. Chem. Res.*, vol. 50, no. 1, pp. 49–57, Jan. 2017, doi: 10.1021/acs.accounts.6b00432.

[20] B. Balaban, S. Doshay, M. Osborn, Y. Rodriguez, and S. A. Carter, “The role of FRET in solar concentrator efficiency and color tunability,” *J. Lumin.*, vol. 146, pp. 256–262, Feb. 2014, doi: 10.1016/j.jlumin.2013.09.049.

[21] G. D. Gutierrez, I. Coropceanu, M. G. Bawendi, and T. M. Swager, “A Low Reabsorbing Luminescent Solar Concentrator Employing π-Conjugated Polymers,” *Adv. Mater.*, vol. 28, no. 3, pp. 497–501, 2016, doi: 10.1002/adma.201504358.

[22] A. Kaniyoor, B. McKenna, S. Comby, and R. C. Evans, “Design and Response of High-Efficiency, Planar, Doped Luminescent Solar Concentrators Using Organic–Inorganic Di-Ureasil Waveguides,” *Adv. Opt. Mater.*, vol. 4, no. 3, pp. 444–456, 2016, doi: 10.1002/adom.201500412.

[23] C. Corrado, S. W. Leow, M. Osborn, E. Chan, B. Balaban, and S. A. Carter, “Optimization of gain and energy conversion efficiency using front-facing photovoltaic cell luminescent solar concentratordesign,” *Sol. Energy Mater. Sol. Cells*, vol. 111, pp. 74–81, Apr. 2013, doi: 10.1016/j.solmat.2012.12.030.

[24] B. A. Swartz, T. Cole, and A. H. Zewail, “Photon trapping and energy transfer in multiple-dye plastic matrices: an efficient solar-energy concentrator,” *Opt. Lett.*, vol. 1, no. 2, p. 73, Aug. 1977, doi: 10.1364/OL.1.000073.

[25] S. T. Bailey *et al.*, “Optimized excitation energy transfer in a three-dye luminescent solar concentrator,” *Sol. Energy Mater. Sol. Cells*, vol. 91, no. 1, pp. 67–75, Jan. 2007, doi: 10.1016/j.solmat.2006.07.011.

[26] I. Z. Steinberg, “Long-Range Nonradiative Transfer of Electronic Excitation Energy in Proteins and Polypeptides,” *Annu. Rev. Biochem.*, vol. 40, no. 1, pp. 83–114, Jun. 1971, doi: 10.1146/annurev.bi.40.070171.000503.

[27] C. Botta, P. Betti, and M. Pasini, “Organic nanostructured host–guest materials for luminescent solar concentrators,” *J. Mater. Chem. A*, vol. 1, no. 3, pp. 510–514, 2013, doi: 10.1039/C2TA00632D.

[28] H. P. Erickson, “Size and shape of protein molecules at the nanometer level determined by sedimentation, gel filtration, and electron microscopy,” *Biol. Proced. Online*, vol. 11, pp. 32–51, May 2009, doi: 10.1007/s12575-009-9008-x.

[29] C. Tummeltshammer *et al.*, “On the ability of Förster resonance energy transfer to enhance luminescent solar concentrator efficiency,” *Nano Energy*, vol. 32, pp. 263–270, Feb. 2017, doi: 10.1016/j.nanoen.2016.11.058.

[30] L. R. Wilson and B. S. Richards, “Measurement method for photoluminescent quantum yields of fluorescent organic dyes in polymethyl methacrylate for luminescent solar concentrators,” *Appl. Opt.*, vol. 48, no. 2, p. 212, Jan. 2009, doi: 10.1364/AO.48.000212.

[31] C. Corrado *et al.*, “Power generation study of luminescent solar concentrator greenhouse,” *J. Renew. Sustain. Energy*, vol. 8, no. 4, p. 043502, Jul. 2016, doi: 10.1063/1.4958735.

[32] B. A. Swartz, T. Cole, and A. H. Zewail, “Photon trapping and energy transfer in multiple-dye plastic matrices: an efficient solar-energy concentrator,” *Opt. Lett.*, vol. 1, no. 2, p. 73, Aug. 1977, doi: 10.1364/OL.1.000073.

[33] E. Deplazes, D. Jayatilaka, and B. Corry, “ExiFRET: flexible tool for understanding FRET in complex geometries,” *J. Biomed. Opt.*, vol. 17, no. 1, p. 011005, 2012, doi: 10.1117/1.JBO.17.1.011005.

[34] J. E. Huheey, E. A. Keiter, R. L. Keiter, and O. K. Medhi, *Inorganic Chemistry: Principles of Structure and Reactivity*. Pearson Education, 2006. [Online]. Available: https://books.google.com/books?id=Ix1fTQ5gY5cC

[35] “Hydrogen and Fuel Cell Technologies Office,” *Energy.gov*. https://www.energy.gov/eere/fuelcells/hydrogen-and-fuel-cell-technologies-office (accessed Aug. 27, 2023).

[36] “Hydrogen direct reduction (H-DR) in steel industry—An overview of challenges and opportunities - ScienceDirect.” https://www.sciencedirect.com/science/article/abs/pii/S095965262103972X (accessed Aug. 27, 2023).

[37] D. R. Barcellos, M. D. Sanders, J. Tong, A. H. McDaniel, and R. P. O’Hayre, “BaCe0.25Mn0.75O3−δ—a promising perovskite-type oxide for solar thermochemical hydrogen production,” *Energy Environ. Sci.*, vol. 11, no. 11, pp. 3256–3265, Nov. 2018, doi: 10.1039/C8EE01989D.

[38] W. C. Chueh *et al.*, “High-flux solar-driven thermochemical dissociation of CO2 and H2O using nonstoichiometric ceria,” *Science*, vol. 330, no. 6012, pp. 1797–1801, Dec. 2010, doi: 10.1126/science.1197834.

[39] “Lattice parameters and orthorhombic distortion of CaMnO3 | Powder Diffraction | Cambridge Core.” https://www.cambridge.org/core/journals/powder-diffraction/article/abs/lattice-parameters-and-orthorhombic-distortion-of-camno3/113D60BE35C65E028A6A4261AB25C4F5 (accessed Aug. 27, 2023).

[40] R. Ali and M. Yashima, “Space group and crystal structure of the Perovskite CaTiO3 from 296 to 1720K,” *J. Solid State Chem.*, vol. 178, no. 9, pp. 2867–2872, Sep. 2005, doi: 10.1016/j.jssc.2005.06.027.

[41] H. Yoshida, S. Nonoyama, Y. Yazawa, and T. Hattori, “Quantitative determination of platinum oxidation state by XANES analysis,” *Phys. Scr.*, vol. 2005, no. T115, p. 813, Jan. 2005, doi: 10.1238/Physica.Topical.115a00813.

[42] Z. Li, M. Yang, J.-S. Park, S.-H. Wei, J. J. Berry, and K. Zhu, “Stabilizing Perovskite Structures by Tuning Tolerance Factor: Formation of Formamidinium and Cesium Lead Iodide Solid-State Alloys,” *Chem. Mater.*, vol. 28, no. 1, pp. 284–292, Jan. 2016, doi: 10.1021/acs.chemmater.5b04107.